



HAL
open science

Investigation of the band structure of quantum wells based on gapless and narrow-band semiconductors HgTe and InAs

Leonid Bovkun

► **To cite this version:**

Leonid Bovkun. Investigation of the band structure of quantum wells based on gapless and narrow-band semiconductors HgTe and InAs. Materials Science [cond-mat.mtrl-sci]. Université Grenoble Alpes; Académie des sciences de Russie (1992-..), 2018. English. NNT : 2018GREAY060 . tel-02057445

HAL Id: tel-02057445

<https://theses.hal.science/tel-02057445>

Submitted on 5 Mar 2019

HAL is a multi-disciplinary open access archive for the deposit and dissemination of scientific research documents, whether they are published or not. The documents may come from teaching and research institutions in France or abroad, or from public or private research centers.

L'archive ouverte pluridisciplinaire **HAL**, est destinée au dépôt et à la diffusion de documents scientifiques de niveau recherche, publiés ou non, émanant des établissements d'enseignement et de recherche français ou étrangers, des laboratoires publics ou privés.

THÈSE

Pour obtenir le grade de

DOCTEUR DE LA COMMUNAUTE UNIVERSITE GRENOBLE ALPES

préparée dans le cadre d'une cotutelle entre la
Communauté Université Grenoble Alpes et
Institute for Physics of Microstructure RAS

Spécialité : **physique des matériaux**

Arrêté ministériel : le 6 janvier 2005 – 25 mai 2016

Présentée par

Leonid BOVKUN

Thèse dirigée par **Dr. Marek POTEMSKI**
et **Prof. Vladimir GAVRILENKO**
codirigée par **Dr. Milan ORLITA**

préparée au sein des **Laboratoire National des Champs
Magnétiques Intenses, CNRS, Grenoble, France**

Étude de la structure de bande de puits quantiques à base de semi-conducteurs de faible bande interdite HgTe et InAs

Thèse soutenue publiquement le **26/11/2018**,
devant le jury composé de :

Dr. Joël CIBERT

Institut NEEL CNRS, Grenoble, France, Président

Prof. Yves GULDNER

Ecole Normale Supérieure de Paris, France, Rapporteur

Prof. Roman STEPNIEWSKI

University of Warsaw, Pologne, Rapporteur

Dr. Ilya SHEIKIN

LNCMI, CNRS, Grenoble, France, Membre

Prof. Dmitriy KHOKHLOV

Faculty of Physics, Moscow State University, Russie, Membre



Acknowledgements

It would not have been possible to write this Ph.D. thesis without the help and support of the kind people around me, to only some of whom it is possible to give particular mention here. I would like to deeply acknowledge to the thesis supervisor Vladimir Gavrilenko for accepting me as a student, for fruitful discussion and corrections of manuscripts. I appreciate his patience, guidance into how to become an independent researcher, share of ideas and personal attitude that extends beyond the field of physics. I am also very grateful to Anton Ikonnikov, who devoted to me a great deal of time for valuable discussions not only scientific results but also thicknesses and colors of Landau levels in the plots. I would like to thank my supervisor Marek Potemski for his kind and valuable advices at every stages of my scholarship (e.g. possibility to use the biggest screen in the group). I would like to emphasize the help and guidance of my co-supervisor Milan Orlita in high-field experiments as well as during preparation reply to referees. I start drinking coffee because of Milan as well.

I am thankful to the fellowship of the close colleagues for providing a friendly atmosphere and stimulating environment at IPM RAS Russia, especially in in department for physics of semiconductors. My cordial gratitude belongs to head of the lab Sergey. Morozov, to Kirill Spirin for the affinity, to Kirill Maremyanin for patience, to Alexandr Antonov and to Sergey Sergeev for help in engineering. I appreciate the help and cooperation with Vladimir Aleshkin, Sergey Krishtopenko and Maxim Zholudev. I would like to thank Vladimir Rumyantsev, Alexander Kadykov and Pavel Bushuikin.

The experimental work in the LNCMI would be hardly feasible without considerable help of infrared lab team. I thank Michael Hakl not only for introducing me into Fourier infrared spectroscopy but also for his company during trekking in Chartreuse. I thank Iris Crassee for help with Faraday rotation experiments. I thank Gerard Martinez for his personal support and translations into French. I would like to acknowledge Clément Faugeras for the complementary Raman measurements. I thank Benjamin Piot for the help with the transport characterization. I am indebted to Arthur Slobodeniuk for companionship and for theoretical advices on julienne slicing of salad. Many thanks should be expressed to Inna Lobanova, Maciej Molas, Benoit Roberge, Maciej Koperski, Younes Henni. I am thankful to Ivan Breslavetz, Robert Pankow and Eyub Yildiz for the technical support of the experimental instruments. The author also conveys thanks to the staff of Laboratoire National des Champs Magnétiques Intenses for the hospitality and access to the installation and laboratory facilities, specifically to the secretaries Alexandra Gasparini and Amelie Pic for the help with the administration, to Ghenadie Novitchi for the support with chemistry. Surely, one should thank CNRS-Liquefier for providing liquid helium.

It is my pleasure to thank all jury members – Dr. Joël Cibert, Prof. Yves Guldner, Prof. Roman Stepniewski, Dr. Ilya Sheikin and Prof. Dmitriy Khokhlov for the acceptance to review this thesis.

Because the doctoral study does not consist only of the world within the walls of the laboratory, I would like to thank also my parents and my wife Olga. Another important acknowledgement is devoted to all my friends, with whom I had the opportunity to spend this great time both in Grenoble and in Nizhny Novgorod.

This work was supported by the Russian Science Foundation, by CNRS through the LIA TeraMIR project and by ANR through Dirac3D project. I thank the French Embassy in Moscow provided me with Vernadski scholarship for co-tutelle program. Author acknowledges the support of LNCMI-CNRS, a member of the European Magnetic Field Laboratory (EMFL). This work was done under auspices of the Université Grenoble Alpes and was funded from the ERC project MOMB (No. 320590).

Abbreviations

2D	two-dimensional
3D	three-dimensional
B-field	magnetic field
BHZ	Bernevig, Hughes and Zhang
BIA	bulk inversion asymmetry
CB	conduction band
CR	cyclotron resonance
DQW	double quantum well
E1, E2	electron band
FR	Faraday rotation
HH1, HH2	heavy hole band
IIA	interface inversion asymmetry
IR	infrared
LL	Landau level
MBE	molecular beam epitaxy
MCT	mercury cadmium telluride
ML	monolayer
QCL	quantum cascade lasers
QW	quantum well
SdH	Shubnikov-de Haas
SIA	structure inversion asymmetry
SL	superlattice
TI	topological insulator
VB	valence band

Table of Contents

Acknowledgements	i
Abbreviations	ii
Résumé (Fr)	1
Introduction	3
Chapter 1. Two-dimensional topological insulators based on gapless and narrow-band semiconductors (review)	9
1.1 Heterostructures HgTe/CdHgTe	9
1.1.1 Superlattices and single quantum wells	9
1.1.2 Topological properties and other effects of spin-orbit coupling	14
1.1.3 Double quantum wells	17
1.2 Heterostructures InAs/GaSb	19
Chapter 2. Experimental methods	22
2.1 Magnetooptics with monochromatic sources	22
2.2 Fourier-spectroscopy in magnetic fields	23
2.3 Thermally activated conductivity	24
Chapter 3. Observation of symmetry lowering effects in HgTe single quantum wells with a rectangular potential	27
3.1 Experimental details	28
3.2 Hamiltonian and eigenstates for system with reduced symmetry	30
3.3 Matrix elements for optical transitions between Landau levels	31
3.4 Dominant and high energy optical transitions in axial model	34
3.5 Effects of symmetry lowering in low-fields and avoided crossings	40
Chapter 4. Observation of structural inversion asymmetry in single HgTe single quantum wells with selective barrier doping	46
4.1 Experimental details	46
4.2 Oscillating splitting of cyclotron resonance modes	50
4.3 Spin vs magnetic quantization in fields up to 34 T	52
Chapter 5. Activation conductivity in HgTe/CdHgTe quantum wells at integer Landau level filling factors: role of the random potential	55
5.1. Experimental details	55
5.2. Determination of the mobility gap Δ_T	57
5.3. Broadening of the Landau levels	Error! Bookmark not defined.
5.4. Determination of the energy gaps	59
5.5. Comparison with the calculated Landau levels	62

Chapter 6. Exploring magneto-optical properties of double quantum wells HgTe/CdHgTe	65
.....	
6.1. Experimental details.....	65
6.2. «Doubling» of dominant absorption lines in spectra	67
6.3. Splitting of $n = -2$ Landau levels in heterostructures with inverted band ...	75
Chapter 7. Dirac fermions in InAs/GaSb/InAs	81
7.1. Experimental details.....	81
7.2. Determination of band mass in quasi-classical magnetic fields	83
7.3. Cyclotron resonance in quantizing magnetic fields up to 34 T.....	86
Conclusions	92
Author's publications related to this work	94
Bibliography	95

Résumé (Fr)

Le tellurure de mercure et de cadmium (HgCdTe ou MCT) est un matériau reconnu pour la physique de la matière condensée, dont l'histoire, datant aujourd'hui de plus de cinquante ans, constitue un excellent exemple des progrès remarquables réalisés dans la recherche sur les semi-conducteurs et les semi-métaux. Notre travail est principalement motivé par l'intérêt fondamental que suscitent ces systèmes, mais notre recherche peut également avoir un impact pratique (indirect) sur la médecine, la surveillance ou la détection de l'environnement ainsi que sur les systèmes de sécurité. Cela peut aider à améliorer les performances des photodétecteurs dans la limite des grandes longueurs d'onde ou à faciliter la fabrication de dispositifs émettant de la lumière.

La présente thèse de doctorat vise principalement à combler certaines des lacunes de notre compréhension de la structure de bande électronique des hétérostructures 2D et quasi-2D basées sur les matériaux HgTe/HgCdTe et InAs/InSb, qui peuvent être transformés en phase topologiquement isolante à l'aide des paramètres de croissance. Pour explorer leurs propriétés, la technique expérimentale de base, la magnéto-spectroscopie infrarouge et THz fonctionnant dans un large éventail de champs magnétiques, est combinée à des mesures complémentaires de magnéto-transport. Cette combinaison de méthodes expérimentales nous permet d'obtenir de précieuses informations sur les états électroniques non seulement à l'énergie de Fermi, mais également dans son voisinage relativement large. Diverses hétérostructures ont été étudiées avec des caractéristiques globales et/ou spécifiques déterminées principalement par les paramètres de croissance.

Les études présentées et les résultats obtenus incluent :

1. L'étude des hétérostructures non dopées HgTe/CdHgTe avec un seul puits quantiques (PQ) ayant un niveau de Fermi situé dans la bande de valence. Nous spécifions les caractéristiques expérimentales des échantillons de conductivité de type p en les comparant avec les données de la littérature sur des échantillons de type n. Nous faisons une analyse systématique des résultats et identifions les tendances dans une série d'échantillons augmentant la largeur des puits quantiques, avec donc le passage d'une structure de bande normale à une structure à bande inversée (correspondant à la phase d'un isolant topologique). Nous identifions les caractéristiques liées aux effets de l'abaissement de la symétrie dans la bande de valence.
2. L'étude des hétérostructures Hg(Cd)Te/CdHgTe avec un dopage barrière asymétrique, à la fois dans des échantillons avec une structure à bande normale inversée. Identification des caractéristiques de magnéto-transport et magnéto-optiques associées au splitting de Bychkov-Rashba.
3. L'étude des hétérostructures HgTe/CdTe à double PQ. Nous analysons les caractéristiques dues à la transparence tunnel de la barrière.
4. L'étude des hétérostructures "à trois couches" InAs/GaSb dans les champs magnétiques classiques et dans la limite quantique. Nous identifions les caractéristiques associées à la présence de sous-bandes paraboliques et "coniques" dans la bande de conduction.

La réponse magnéto-optique observée, due aux excitations intra-bande (résonance cyclotron) et interbandes (entre les niveaux de Landau) peut être interprétée dans le contexte d'études antérieures sur des échantillons 3D, des puits quantiques et des super-réseaux, mais également en rapport aux attentes théoriques. Ici, nous visons à obtenir une explication quantitative des données expérimentales recueillies, mais également à développer un modèle théorique fiable. Ce dernier comprend le réglage précis des paramètres de structure de bande présents dans le modèle établi de Kane, mais surtout, l'identification de termes supplémentaires pertinents (d'ordre élevé) nécessaires pour parvenir à un accord quantitatif avec nos expériences. On peut s'attendre à ce que les corrections dues à ces termes supplémentaires affectent davantage les sous-bandes de valence, généralement caractérisées par des masses effectives relativement

importantes et, par conséquent, par une grande densité d'états ou, lorsque le champ magnétique est appliqué, par un espacement assez étroit (et mélange important) des niveaux de Landau. Les conclusions générales du manuscrit sont les suivantes :

1. Dans les spectres de magnétoabsorption de puits quantiques simples HgTe / CdHgTe, les lignes associées aux transitions entre les niveaux de Landau interdites dans le cadre du modèle de loi de dispersion axiale largement utilisé sont observées, ce qui est dû à l'anisotropie des liaisons chimiques au niveau des hétérointerfaces et l'absence de centre d'inversion dans le réseau cristallin.
2. Dans les puits quantiques asymétriques de type n Hg(Cd)Te/CdHgTe à dopage sélectif unilatéral des barrières, le splitting "géant" de Rashba est observé non seulement dans des échantillons à structure inversée mais également normale, ce qui est dû, dans les deux cas, à un mélange significatif de la fonction d'onde du trou, avec celle des électrons dans la bande de conduction.
3. Dans les puits quantiques de HgTe / CdHgTe, les effets d'échange pour le splitting de spin des niveaux de Landau sont négligeables et les valeurs des gaps de spin déterminés par magnéto-transport sont en bon accord avec les résultats des calculs à un électron.
4. Dans les hétérostructures à double puits quantique HgTe / CdHgTe, séparées par une barrière mince ($t \sim 3$ nm), les lignes d'absorption principales sont doublées (par rapport à un puits unique), ce qui indique sa transparence tunnel pour les états électroniques. L'analyse des spectres de magnéto-absorption confirme la prédiction théorique de la formation de l'état sans gap dans un DQW avec une largeur critique de puits unique. Dans ce cas, la structure de la bande est analogue à celle d'un graphène bicouche (les sous-bandes paraboliques d'électrons et de trous se touchent au point $k = 0$).
5. Dans les champs magnétiques classiques, on observe l'élargissement et le décalage de la raie CR avec une densité décroissante d'électrons dans des puits quantiques InAs / GaSb / InAs à trois couches symétriques, encapsulés entre des barrières AlSb avec des épaisseurs de couche conçues pour une structure en bande sans gap avec un cône de Dirac au centre de la zone de Brillouin. Un tel comportement indique la présence de sous-bandes "coniques" et paraboliques dans la bande de conduction. Lors de la quantification de champs magnétiques (jusqu'à 34 T), la présence de sous-bandes "coniques" se manifeste par l'apparition d'une nouvelle raie d'absorption due à une transition issue du niveau de Landau le plus bas dans la bande de conduction.

Introduction

Relevance of the research topic & state-of-the-art

Mercury cadmium telluride (HgCdTe or MCT) is a time-honored material for condensed matter physics, whose history – nowadays more than fifty years long – may serve as an excellent example of remarkable progress made in research on semiconductors and semimetals. The ternary compound HgCdTe implies two important aspects, which largely contributed to its undoubted success in solid-states physics.

Primarily, it is the relatively simple and highly tunable (via external or internal parameters) electronic band structure. This may be understood in terms of the Kane model, well established in the field of zinc-blende semiconductors, and tuned by means of the compound composition, temperature, strain/stress, but also, using the quantum confinement. This way, HgCdTe may be tune to a bulk semimetal, semiconductor with a narrow or sizeable band gap (see reviews in [[1-3](#)]), 2D or 3D topological insulator [[4-6](#)], 2D Dirac semimetal [[7](#)], but possibly also 3D Dirac/Weyl semimetal [[8](#)].

Secondly, it is the tremendous progress in technology. This allows us to prepare high-quality bulk crystals, via traditional Bridgman or Czochralski techniques, which have been used for this purpose already back in sixties [[9-11](#)]. The fast advancing novel techniques of growth of low-dimensional structures (for instance, molecular-beam and liquid-phase epitaxy) enable routine fabrication of quantum dots, wires and wells [[12-14](#)], but also more complex 2D heterostructures, such as coupled quantum wells or superlattices [[15](#)]. The current technology also allows us to produce HgCdTe with a relatively high quality (expressed, *e.g.*, in terms of electronic mobility), to control its doping with a high precision and to process it into devices.

Thanks to this, HgCdTe nowadays plays a crucial role in both fundamental and applied physics. For instance, this material is routinely and successfully used as an efficient detector of light, operating efficiently in a broad range of photon energies, from the THz till near-visible spectral range [[16](#)]. Such infrared detectors nowadays belong to the standard equipment of optical laboratories, but may operate in much less expected situations, for instance, as photodetectors checking the temperature of wheels on the famous TGV high-speed trains. Relatively large atomic masses also predetermine the use of HgCdTe (more often in the binary form CdTe) as efficient x-ray detectors [[17](#)].

At the same time, HgCdTe heterostructures nowadays play a prominent role in the emerging field of topological matter. As a matter of fact, it was the wide HgTe quantum well, which was theoretically predicted [[18](#)] and subsequently experimentally proved to be the very first topological insulator. This was manifested by the observation of the Quantum Spin Hall Effect [[6](#)], and thus paved the way to other materials with non-trivial topological properties. Just to illustrate the impact of HgTe in the field of topological insulators, let us mention that the Google Scholar search engine now returns 5470 results for "HgTe" and 17.800 results "topological insulator" newer than from 2014.

This remarkable success of an “old” compound in the applied, and especially, in fundamental physics in turn calls for further investigations. Among other, there exists a quest for better quantitative understanding of observed phenomena. In this respect, the standard Kane model, which is often applied to describe the electron and hole subbands in HgTe quantum wells, or when the magnetic field is applied, to deduce the corresponding Landau level spectrum, provides us in many cases only with a qualitatively valid output. Therefore, we search for an expanded version of this model, which takes account of various symmetry-lowering effects. These include effect due to bulk, structure as well as interface inversion asymmetries.

State of the art of the research topic

The present PhD thesis primarily aims at filling some of existing gaps in our understanding of the electronic band structure in 2D and quasi-2D heterostructures based on HgTe/HgCdTe and InAs/InSb materials, which both may be tuned into topologically insulating phase using particular structural parameter. To explore their properties, the primal experimental technique, infrared and THz magneto-spectroscopy operating in a broad of magnetic fields, is combined with complementary magneto-transport measurements. This combination of experimental methods allows us to get valuable insights into electronic states not only at the Fermi energy, but also in relatively broad vicinity.

The observed magneto-optical response – due to intraband (cyclotron resonance) and interband inter-Landau level excitations – may be interpreted in the context of previous studies performed on bulk samples [19-22], quantum wells [23-33] and superlattices [34-41], but also compared with theoretical expectations. Here we aim at achieving the quantitative explanation of the collected experimental data, but also further developing a reliable theoretical model. The latter includes the fine-tuning of the band structure parameters present in the established Kane model, but even more importantly, identifying additional relevant (high-order) terms and finding their particular strengths, needed to achieve quantitative agreement with our experiments. One may expect that corrections due to these additional terms will more affect the valence subbands, which are in general characterized by relatively large effective masses. Consequently, valence subbands have larger density of states compared to conduction band or, when the magnetic field is applied, rather narrow spacing (and possibly large mixing) of Landau levels.

Our work is primarily driven by the fundamental interest in these systems, but at the same time, our investigations may have some (indirect) practical impact in medicine, environmental monitoring/sensing, and security systems. It may help to advance the performance of photodetectors in the long-wavelength limit or to facilitate the fabrication of light-emitting devices. One may mentioned, for instance, the recent progress in obtaining of the long-wavelength stimulated emission (up to 20 μm) from structures based on HgTe quantum well [42, 43]. Our work may also contribute to the overall understanding of 2D topologically insulating phase in InAs multilayers, the bulk energy of which is predicted to reach 60 meV [44], providing thus a considerable stability of such a topological insulator against thermal fluctuations.

Goals and objectives

The main goal of the thesis was to obtain new scientific insights into the electronic band structure of heterostructures with QWs based on narrow bandgap and gapless $\text{Hg}_{1-x}\text{Cd}_x\text{Te}$ solid solutions and InAs/GaSb heterostructures. Each of the systems was studied by a combination of transport and optical methods in magnetic fields up to 35 T. Various heterostructures were studied with overall characteristics, and specific features determined mainly through the growth parameters.

The presented studies and the obtained results include:

1. Study of undoped heterostructures HgTe/CdHgTe with single QW with a Fermi level located in the valence band. We specify the characteristic experimental features for samples of the p -type conductivity in comparison with the literature data on n -type samples. A systematic analysis of the results and the identification of trends within a sample series increasing quantum well width, therefore with a transition from a normal to inverted band structure (corresponding to the phase of a topological insulator). Identification of features related to the effects of the symmetry lowering in the valence band.

2. Investigation of heterostructures Hg(Cd)Te/CdHgTe with asymmetric barrier doping both in samples with both inverted normal band structure. Identification of magnetotransport and magneto-optical features associated with the Bychkov – Rashba splitting.
3. Investigation of heterostructures HgTe/CdTe with double QW. Analysis of the features due to the tunneling transparency of the barrier.
4. Investigation of "three-layer" heterostructures InAs/GaSb in classical and quantizing magnetic fields. Identification of features associated with the presence of parabolic and "conical" subbands in the conduction band.

Scientific novelty

1. Interband and intraband resonant absorption lines between Landau levels have been traced in a broad range magnetoabsorption spectra ($\hbar\omega = 5\text{--}250$ meV), both in valence and conduction bands, in quantizing magnetic fields of p -type quantum wells HgTe/CdHgTe with both normal and inverted band structure.
2. In quantum wells with a normal band structure, the absorption lines are found for transitions that are forbidden by the selection rules within the framework of the axial model. It is shown that the violation of the selection rules is related to the mixing of states in the valence band due to the anisotropy of the chemical bonds at the heterointerfaces and the absence of an inversion center in the crystal lattice. In a sample with an inverted band structure, the avoided crossing was first observed for the case of partial filling of the "zero" Landau levels, which indicates a single-particle character of the phenomenon.
3. The absorption spectra were studied in both classical and quantizing magnetic fields in asymmetric heterostructures with HgCdTe / CdHgTe quantum wells with a selective one-sided doping of barriers with a large electron density ($n_s \geq 10^{12}$ cm⁻²). At low fields, a strong splitting of the cyclotron resonance line ($\sim 10\%$) is observed, which is related to the Rashba effect in samples with both inverted and, for the first time, normal band structure. The splitting of the cyclotron resonance line is oscillating with magnetic field, which are associated with magnetic quantization in the upper subband with a smaller number of filled Landau levels. The evolution of the absorption lines with a magnetic field is traced up to 34 T, when the magnetic quantization already prevails over the Rashba splitting. In magnetic fields of 15 – 20 T in the absorption spectra, a manifestation of the anticrossing of the Landau levels from the first and second subbands of size quantization was observed.
4. The magnetoabsorption spectra in double quantum wells HgTe / CdHgTe of different widths were studied and doubling (compared to a single QW) of the number of main magnetoabsorption lines associated with tunneling transparency of the barrier for electronic states was demonstrated. In a sample with a well width close to the critical value ($d_c = 6.3$ nm), a shift in the magnetoabsorption lines was observed with a change in the carrier concentration due to the persistent photoconductivity effect associated with a change in the potential profile upon recharge of traps.
5. The cyclotron resonance spectra have been experimentally studied in "three-layer" symmetric InAs/GaSb/InAs QWs encapsulated between AlSb barriers with the calculated layer thicknesses corresponding to the gapless band structure at different electron concentration values. In "classical" magnetic fields, the broadening and shift of the absorption line to the region of smaller cyclotron masses are revealed, which confirm the existence of two subbands with parabolic and "conical" dispersion laws in the conduction band. In the cyclotron resonance spectra in quantizing magnetic fields up to 34 T, the appearance of a new higher-frequency absorption line associated with transitions from the lower Landau level of electrons in the subband with a "conical" dispersion law was found

in accordance with the results of calculations performed using the 4-band Kane Hamiltonian.

Theoretical and practical significance of the work

The scientific significance of the work is to obtain a new scientific knowledge about the optical properties and structure of the band structure in heterostructures with HgTe/CdHgTe and GaAs/InSb heterostructures in the terahertz, far infrared and middle infrared spectral ranges.

The criteria for determining the conductivity type and the character of the band structure (normal, inverted), based on the characteristic features of the magnetoabsorption spectra, have been developed in the work. It is shown that magneto-optical studies are a source of reliable information not only about the value of the energy gap, but also about the relative location of the nearest subbands of size quantization. The latter is relevant for the construction of laser structures based on HgTe/CdHgTe QWs.

Methodology and experimental techniques

Author employ approved methods developed and applied in the Institute for Physics of Microstructures of the Russian Academy of Sciences, (Nizhny Novgorod, Russia) and the Laboratoire National des Champs Magnétiques Intenses (LNCMI, Grenoble, France). The work was carried out as part of a joint Russian – French postgraduate study.

- Absorption spectroscopy with a magnetic field sweep up to 5.5 T at 4.2 K using monochromatic sources of radiation — quantum cascade lasers in the THz range.
- Transport measurements with optional temperature control down to 1.6 K and in a magnetic field up to 12 T.
- Fourier spectroscopy in the far and middle IR range in magnetic fields of up to 11 T at 4.2 K combined with the simultaneous transport experiments.
- Faraday rotation experiment in the far and middle IR range in a magnetic field of 11 T at 4.2 K using fixed and turning linear polarizers.
- Fourier spectroscopy in the far and middle IR range in magnetic fields of up to 34 T at 1.6 K in a resistive magnet.

General findings of the thesis

1. In the magnetoabsorption spectra of single quantum wells HgTe/CdHgTe, the lines associated with transitions between Landau levels that are forbidden within the framework of the widely used axial dispersion law model are observed, which is due to anisotropy of chemical bonds at heterointerfaces and the absence of an inversion center in the crystal lattice.
2. In *n*-type asymmetric quantum wells Hg (Cd)Te/CdHgTe with one-sided selective doping of barriers, the "giant" Rashba splitting is observed not only in samples with inverted but also with normal band structure, which is caused, in both cases, by a significant share of the hole-like states in a multicomponent wave function in the conduction band.
3. In the quantum wells of HgTe/CdHgTe, the exchange enhancement effects of the spin splitting of the Landau levels are negligibly small, and the values of the spin gaps determined from magnetotransport are in good agreement with the results of single-electron calculations.
4. In heterostructures with double quantum wells HgTe/CdHgTe, separated by a thin ($t \sim 3$ nm) barrier, the main absorption lines are doubled (in comparison with a single well),

which indicates its tunnel transparency for electron-like states. The analysis of the magnetoabsorption spectra confirms the theoretical prediction of the formation of the gapless state in DQW with critical single well width. In such case, the band structure is analogous to the structure of a bilayer graphene (the parabolic subbands of electrons and holes touch at the point $k = 0$).

5. In classical magnetic fields the broadening and shift of the CR line is observed with decreasing density of electrons in three-layer symmetric InAs/GaSb/InAs quantum wells, encapsulated with AlSb barriers with layer thicknesses designed for a gapless band structure with a Dirac cone in the center of the Brillouin zone. Such behaviour indicates the presence of "conical" and parabolic subbands in the conduction band. In quantizing (up to 34 T) magnetic fields, the presence of "conical" subbands is manifested in the appearance of a new absorption line due to a transition from the lowest Landau level in conduction band.

The degree of reliability and approbation of the results of the study

The reliability of the results of the research presented in the thesis is provided by the use of methods approved at the LNCMI-CNRS, IPM RAS and in other research centers. The results of experimental studies are presented in comparison with theoretical calculations, as well as with other data presented in the literature. The main results of the thesis were reported at the XIX-XXII International Symposia "Nanophysics and Nanoelectronics" (Nizhny Novgorod, 2015-2018); 12th Russian Conference on Semiconductor Physics (Ershovo, 2015); conferences-schools "New Frontiers in 2D materials: Approaches & Applications" (Villard-de-Lans, France, 2017), "New Developments in Solid State Physics" (Mauterndorf, Austria, 2018), "Science in high magnetic fields" (Arles, France, 2018), as well as at the seminars of the IPM RAS.

In total 31 printed works were published on the subject of the thesis, including 12 articles in refereed journals and 19 publications in collections of abstracts of papers and proceedings of conferences and symposiums. All of the above in aggregate testifies to the reliability of the results obtained and the conclusions drawn on their basis.

Contributions: author and collaborators

HgCdTe-based heterostructures were grown in the Rzhanov Institute of Semiconductor Physics, Siberian Branch, Russian Academy of Sciences (ISP SB RAS, Novosibirsk, Russia) by the group of N.N. Mikhailov, S.A. Dvoretzskii et al. Heterostructures with quantum wells InAs/GaSb were grown in the Institut d'Electronique et des Systemes (IES, Montpellier, France) by E. Tournié, F. Gonzalez-Posada, and G. Boissier et al. as well as in the ISP SB RAS by B.R. Semyagin, M.A. Putyato, E.A. Emelyanov, and V.V. Preobrazhenskii.

Major part of experimental result presented in the manuscript are obtained by the author itself, including (i) simultaneous optical and transport experiment in superconducting magnet up to 11 T at LNCMI, (ii) optical experiments in resistive magnet up to 34 T at LNCMI, (iii) temperature-dependent magnetotransport measurements in superconducting coil up to 12 T at IPM RAS, (iv) transmission experiments with monochromatic sources at IPM RAS. Additional experiments at IPM RAS were performed by A.V. Ikonnikov and K.V. Maremyanin, while experiments at Laboratoire Charles Coulomb (L2C, Montpellier, France) were performed by A.M. Kadykov, M. Marcinkiewicz, S. Ruffenach, C. Consejo, F. Teppe, and W. Knap et al.

Theoretical calculations presented in the manuscript are performed in the Kane model developed by S.S. Krishtopenko for double quantum wells of HgTe and single quantum wells of InAs/GaSb. Another model employed by the author in the thesis has been developed by V.Ya. Aleshkin. In included additional terms of interface inversion asymmetry and bulk

inversion asymmetry. Author analyzed the experimental data in the framework of above-mentioned theoretical approaches.

Author acknowledge V.I. Gavrilenko, M. Orlita, M. Potemski, A.V. Ikonnikov, S.S. Krishtopenko, and V.Ya. Aleshkin et al. for fruitful discussions, allowing explanation different effects mentioned in the presented below results.

Chapter 1. Two-dimensional topological insulators based on gapless and narrow-gap semiconductors (review)

1.1 Heterostructures HgTe/CdHgTe

1.1.1 Superlattices and single quantum wells

Ternary solutions of HgCdTe (i.e. mercury cadmium telluride or MCT) are widely used to create photodetectors for the MIR range [16]. While CdTe is a semiconductor with a normal band structure (i.e. trivial) and a band gap of about 1.6 eV (at low temperature), HgTe, on the contrary, has an inverted band structure with a "negative" band gap $E_g \approx -0.3$ eV (see, for example, [1-3]). HgTe has a crystal lattice of zinc blende (similar to CdTe) but in the center of the Brillouin zone, the point Γ_8 lies higher in energy than the point Γ_6 due to the strong spin-orbit interaction. Consequently, HgTe is a gapless semiconductor with particular band ordering (at the point $k = 0$): the lower subband in the conduction band and the upper valence subband are formed by hole-like states with the angular momentum $J = 3/2$ e.g. p orbital for $k = 0$ (at the point Γ_8) whilst an electron-like subband (states with a moment $J = 1/2$ e.g. s orbital) shifted in the valence band by an energy of 0.3 eV. Complete solubility of HgTe in CdTe provide to solid solutions of $\text{Hg}_{1-x}\text{Cd}_x\text{Te}$ the whole range of x continuous physical properties with forbidden band varying from 1.6 eV at $x = 1$ to zero at $x \sim 0.17$ (at low temperature) [16].

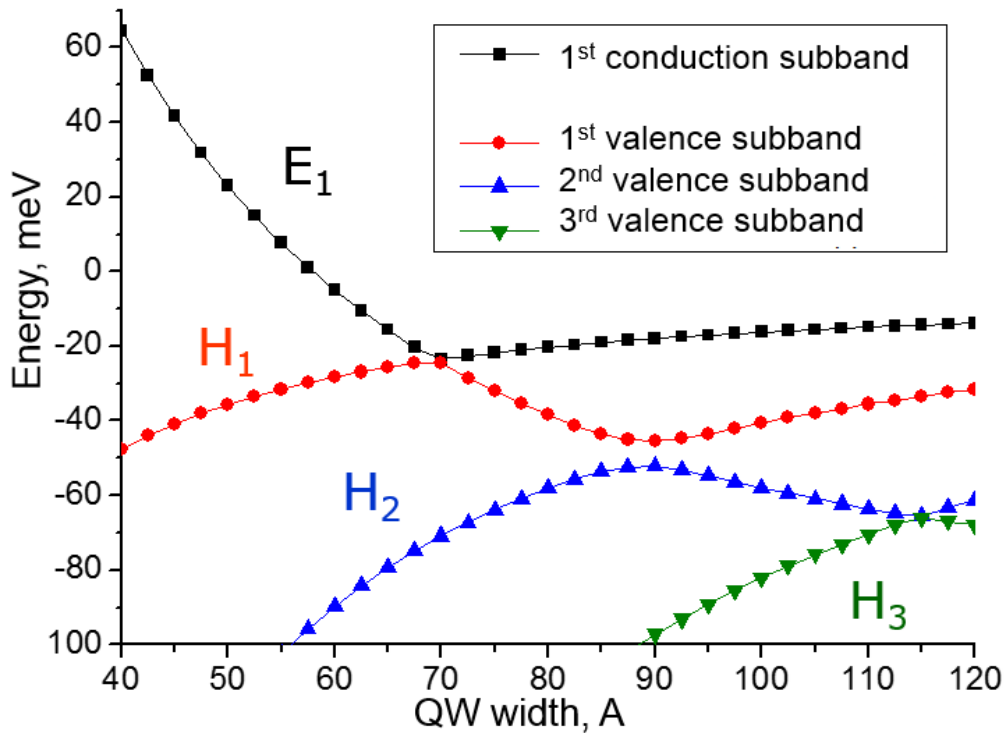


Fig. 1. Calculated energy spectra for conduction and valence subbands for $k_{\perp} = 0$ versus width of quantum well $\text{HgTe}/\text{Cd}_{0.7}\text{Hg}_{0.3}\text{Te}$ (013) at $T = 0$ K. From [45].

Single quantum wells (QWs) HgTe/CdHgTe attract great interest in recent years due to their nontrivial topological properties; moreover, the type of the band ordering is determined by the as-grown width d_{QW} of the quantum well HgTe. Narrow QWs “inherit” the normal band structure of CdHgTe barrier layers (the typical Cd rate is $x \approx 0.7$) due to the quantum penetration of CdHgTe wave functions into HgTe QWs. If one increases QW width then the value of the bandgap decreases to zero at some critical $d_{QW} = d_c \sim 6-7$ nm (depending on the barrier composition, see, for example, [45] on page 52). With further increase of d_{QW} occurs an

inversion of the bands: the electron-like subband E_1 , which is mainly formed by s orbital states, turns out to be lower in energy than the hole-like subband H_1 , which is predominantly formed by orbital p -states, and the gap opens again in the energy spectrum — see Fig. 1. Thus, HgTe/CdHgTe quantum wells are two-dimensional topological insulators: helicoidal states protected against scattering appear on the edges of the structure, thus wise, non-dissipative transport can occur even in the absence of a magnetic field [6].

Historically, the first heterostructures based on MCT, which attracted wide interest, were not single QWs, but superlattices HgTe-CdTe [34], designed to improve the properties of photodetectors because of the relatively sharp edge of fundamental absorption in the quasi-2D structure compared to the bulk material. The energy gap in superlattices was controlled by changing the number of HgTe monolayers in the structure. Parameters of such structures were investigated primarily by magneto-optical methods [36-40]: resonance intraband and interband absorption was observed both in n -type systems [36] and in p -type samples [37]. One of the key parameters required for modelling of the band structure was the valence band offset at the HgTe/CdTe heterojunction, the value of which varied in the calculations from 40 to 550 meV (cf. [35, 36, 41, 46-49]), which did not allow convincing interpretation of the experimental results. Subsequently, the authors of [41] turned to the study of simpler systems: triple and single quantum wells, based on overall experience in the study of superlattices.

At present, quantum confinement for charge carriers is created by means of molecular beam epitaxy: sandwiching an HgTe material with an inverted band structure between the CdHgTe barriers with a normal band structure, i.e. creating quantum well. In contrast, a triangular potential well was created at the heterointerfaces of a semiconductor with a dielectric due to the application of a gate voltage (see Fig. 2) in the early experiments on thick HgTe films (up to 1.5 μm). Oscillations in tunnel magnetotransport were reported in [50, 51], that confirms the appearance of a two-dimensional gas in such structures [52]. Authors performed Fourier analysis of the results and justified simultaneous population of several subbands.

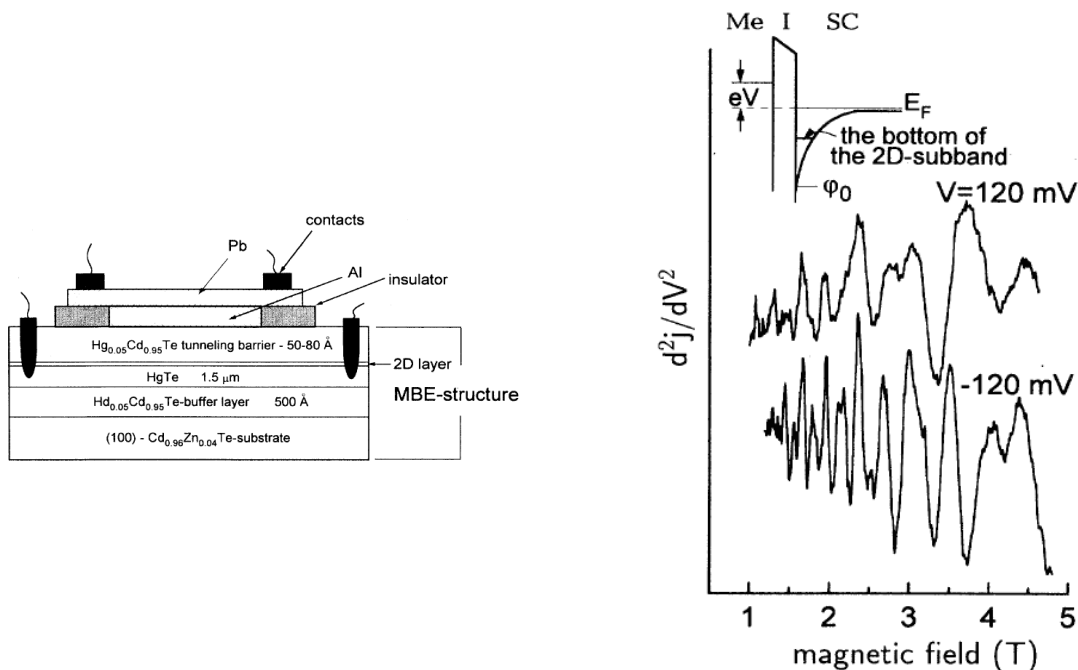


Fig. 2. (left) Schematic representation of the tunnel contact. (right) Typical oscillations of the derivative of the tunneling conductivity dj/dV for different values of the applied bias voltage. The inset shows the potential energy diagram for $V > 0$. From [50].

In [24], magneto-optical and magnetotransport studies were carried out on a sample with a QW width of $d_{QW} = 11.5$ nm with a semi-transparent gate at an electron concentration reaching $n_s \approx 10 \times 10^{12} \text{ cm}^{-2}$ in magnetic fields up to $B = 8$ T. Both beatings in Shubnikov - de Haas oscillations and the splitting of cyclotron resonance line observed, which is associated with the removal of the spin degeneracy of the lower conduction subband (*i.e.* Bychkov - Rashba splitting). The cyclotron resonance in stronger magnetic fields up to $B = 14$ T was investigated in [53]. The object of the study was an *n*-type heterostructure (without intentional doping) consisting of three quantum wells HgTe each 9.5 nm wide, separated by 25 nm $\text{Cd}_{0.7}\text{Hg}_{0.3}\text{Te}$ barriers, thick enough to eliminate tunnelling effects. Three different absorption lines were observed in the spectra (see Fig. 3), which was associated with both a different concentration of electrons in the wells and with magnetic-quantization effects in the quantum well with the lowest concentration. However, the interpretation of the results of the experiment was carried out in the approach of effective masses within the simplified two-band Kane model.

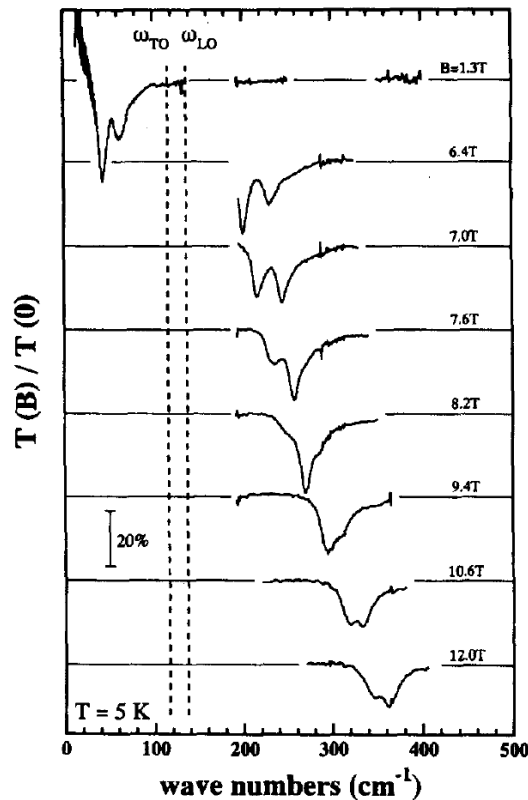


Fig. 3. Normalized transmission spectra for the heterostructure under study for different magnetic field values. Vertical dashed lines show the phonon energy in bulk HgTe. From [53].

Magneto-optical studies of a single HgTe QWs in quantizing magnetic fields have been continued in [26, 54], where results for samples with inverted band structure are presented. In these studies, both intraband (CR in the conduction band) and interband optical transitions were observed for the first time. Interpretation of the results was based on Landau level calculations within the framework of the three-band Kane model. It should be noted that in Ref. [54] the critical magnetic field (at which the "zero" Landau levels intersect, see below) for the HgTe/CdHgTe QW amounted to $B_c \approx 14$ T (while according to our estimates, $B_c \approx 5-7$ T), which is related either to the use of the three-band Kane model (which does not take into account the effect of the spin-split hole subband) or with inaccurate selection of material parameters. The calculations of V.Ya. Aleshkin showed that omitting the spin-split subband leads to a noticeable increase in the value of the energy gap by approximately 20% and, consequently, to a significant

increase in B_c . Thus, despite the significant "isolation" of the spin-split subband $\Delta_{SO} \sim 1$ eV, its effect on the details of the band structure for "narrow-band" QWs is significant. Magnetotransport experiments, in turn, are represented by a more extensive number of publications [55-60]. In these studies, spin effects in the conduction band were studied [55, 57, 59] and estimates for the effective g factor [53, 60] and effective mass were obtained [55], last but not least, the violation of axial symmetry in the valence band was observed associated with the presence of four lateral maxima [56, 58]. Thanks to the above-mentioned experimental works, a theoretical models advance significantly as well using the four-band Kane Hamiltonian, which consequent development is presented below.

There are different approaches towards calculations dispersion law $E(k)$ and the energy of the Landau levels $E_n(B)$ in the HgTe/CdHgTe heterostructures with QWs. One of the first papers [53] used a simple two-band model with an effective band gap parameter E_g^* for the interpretation of observed absorption lines. Later, it was proposed to use the 8×8 Kane Hamiltonian (four-band with double spin degeneracy) [61], it was widely adopted to describe energy spectra both in the conduction band and in valence bands with a normal or inverted band structure [23, 27-29, 43, 57, 59-66]. A simplified two-band model was also proposed for describing gapless and "narrow-gap" quantum wells of HgTe [18]. Its simplicity, in particular, is convenient for describing edge states in quantum wells of HgTe with an inverted band structure [18, 67]. On the other hand, in order to describe more "subtle" effects, additional corrections to the four-band Hamiltonian were suggested, taking into account the effects of symmetry lowering. The first is the so-called Dresselhaus correction (e.g. Bulk Inversion Asymmetry), accounting for the lack of inversion symmetry in the zinc blende crystal lattice [64, 68, 69]; the second correction arises from the anisotropy of the chemical bonds at the interfaces HgTe / CdHgTe (Interface Inversion Asymmetry) [70, 71]. The above effects lead to the fact that initially the orthogonal wave functions belonging to the conduction band (Γ_6) and the valence band (Γ_8) turn out to be "mutually mixed", which was experimentally discovered in papers devoted to the anti-crossing of Landau levels [23, 63, 68].

As mentioned earlier, the width of the quantum well HgTe determines the type of the band spectrum, and for $d_{QW} > 6.3$ nm there is an inverted band ordering. Corresponding samples possess properties of a two-dimensional topological insulator, which attract a lot of attention of researchers. In the early papers [24, 54], the authors studied also inverted structures with $d_{QW} = 8.5$ and 12.2 nm, and for the first time observed resonance absorption in the far infrared region, caused by transitions both within the conduction band (CR-modes) and between the bands (interband transitions). In these papers, the authors discuss in detail the intersection of the "zero" (an established term in the description of the graphene band structure) of the Landau levels in the conduction band and the valence band ($n = 0_{\uparrow}$ and $n = -2_{\downarrow}$ in Fig. 4) with increasing magnetic field, i.e., the transition from the inverted to normal band structure. However, measurements are not detailed enough to detect subtle effects of crossing avoiding of these Landau levels.

In [63] electrons populate both the "zero" Landau levels near the critical magnetic field B_c , which allowed observing the mixing and effect of the avoided crossing of levels via α transition (see Fig. 4), and in work [68] simultaneously for the transitions α and β . The authors of the first work assigned the observed effect to BIA, but speculated about many-particle effects as well. In the second work, attempts were made to theoretically describe the BIA effect for two overlapping levels, but for correct description (fitting) one of the model parameters for HgTe (unknown experimentally) was taken three times as large as for CdTe.

Lesser amount of studies are devoted to the valence band, which is most likely due to its more complex structure and, accordingly, the difficulty in interpreting the results of experiments. The axial approximation is poorly suited for the valence band due to the existence of "lateral" maxima (see, for example, Fig. 5), which, in particular, leads to the appearance of a semimetallic state in wide QWs, when the lateral maxima overlap in energy with a minimum

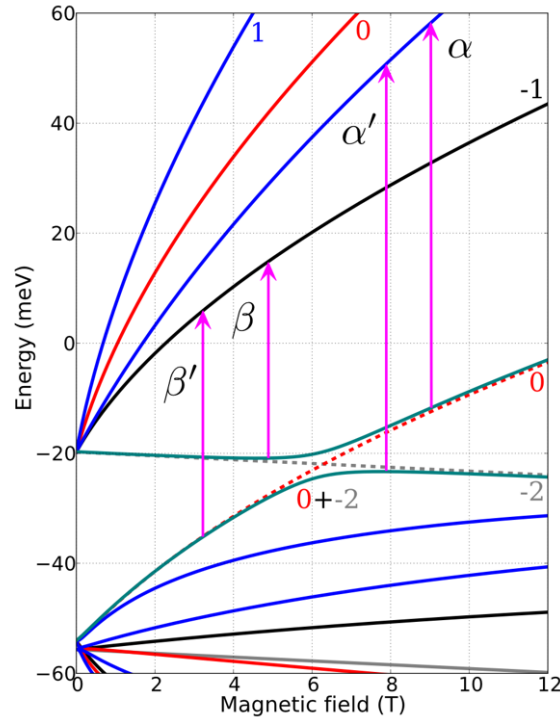


Fig. 4. Calculated Landau levels for the quantum well $\text{HgTe}/\text{Cd}_{0.64}\text{Hg}_{0.36}\text{Te}$ with a width $d_{\text{QW}} = 8$ nm. The arrows indicate the observed transitions. The numbers correspond to the numbers n of the corresponding Landau levels. From [68].

at the Γ -point of the conduction band and the corresponding position of the Fermi level: the coexistence of electrons and holes in the equilibrium conditions of HgTe in a quantum well [72]. The situation is further complicated by the high density of states in the valence band, which leads to mixing of the Landau levels due to the effects of lowering the symmetry.

Investigations of quantum transport [56, 66] have shown a strong difference between samples with electronic and hole types of conductivity. In the first case [66], the heterostructure with $\text{HgTe}/\text{Cd}_{0.7}\text{Hg}_{0.3}\text{Te}$ quantum wells was selectively doped with iodine (in the barriers) and demonstrated the n-type conductivity with pronounced Shubnikov-de Haas oscillations and the quantum Hall effect. In the subsequent work [56] magnetotransport in quantum p -type wells 12-20 nm in thickness was investigated, where one of the barriers was doped with nitrogen. Not only the oscillations of R_{xx} SdH were aperiodic, but also the pronounced QHE plateaus were not observed. The authors performed the simulation of $R_{xx}(B)$ on the 4-band Kane model with a self-consistent Hartree potential. It was verified that a complex picture of the SdH oscillations is related to the determination of the Fermi level in the side valleys of the valence band and the interaction of the Landau levels of the holes. The study of the valence band was continued in [58], where it was shown in transport experiments the presence of an additional peak associated with finding carriers in the four later valleys of the valence band — see Fig. 5. With an increasing Fermi energy, this peak disappeared, and the system becomes axially symmetric.

In later works on wide QWs ($d_{\text{QW}} \sim 20$ nm), overlapping of zones were experimentally observed as an alternating Hall effect, thus demonstrating the existence of charge carriers of both plus and minus signs in the structures [73]. In subsequent studies, the transition from a metallic to a semimetallic state was observed by shifting the position of the Fermi level in experiments with microwave cyclotron resonance, detected by a relative changes in the sample resistance [74, 75]. Finally, a significant discrepancy of the theoretical valence band structure and experimental results in magnetotransport was demonstrated in structures with semimetallic conductivity [76]. The splitting of the valence band was observed in samples with a normal

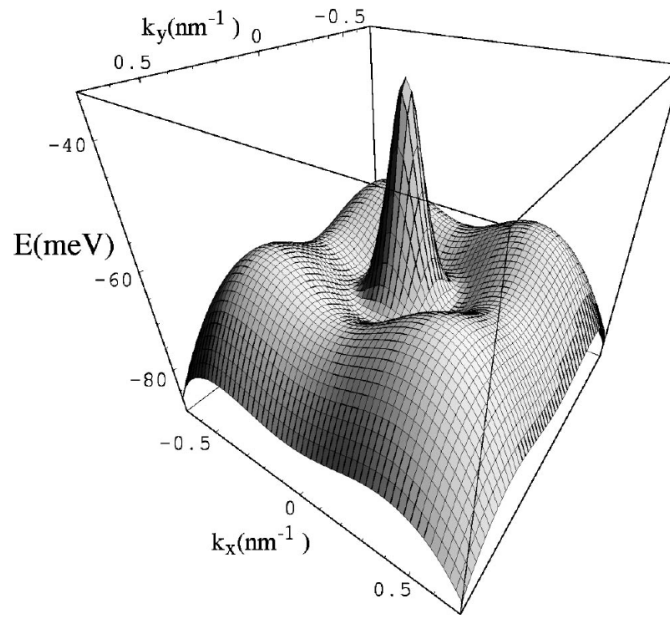


Fig. 5. A three-dimensional representation of the self-consistent calculation for the H1 subband for a sample with $d_{QW} = 5.8$ nm and hole concentration $p_s = 3.0 \times 10^{11}$ cm $^{-2}$. Four lateral peaks and the central Γ -valley are clearly visible. From [58].

band structure. In early works [56, 58] this effect was associated with the appearance of a lateral local maxima in the dispersion law associated with the anisotropy of the crystal. In [77] this explanation was criticized and the splitting was theoretically modeled with adjustment for the built-in electric field. Finally, in [78] the authors give a subject second thought, analyzing large number of samples with close parameters and explained the splitting by the mixing effect of states on heterointerfaces [70], and in the subsequent work [71] a model takes into account the different mixing value at QW heterojunctions explained well the results of magnetotransport. Magneto-optical transitions from states in the valence band were investigated in two samples in [23] and [65], but their interpretation was not unambiguous.

1.1.2 Topological properties and other effects of spin-orbit coupling

The topological insulator (TI) is the newly discovered quantum state of material [4, 6, 18, 79, 80]. This state is described with two contradictory properties: "bulk" material has energy gap in the electronic spectrum (no conductivity as in a conventional band insulator), while conductive edge (surface) states with a linear dispersion law appear on its edge, due to a strong spin-orbit interaction. Moreover, edge states are topologically protected by the time-reversal symmetry from backscattering to local distortions and weak disorder of the crystal lattice [4, 79, 80]. The QW HgTe/CdHgTe with an inverted band spectrum is the first 2D system experimentally demonstrated [6] edge states as signature of the TI. As already noted, in discussed heterostructures the transition from the normal band structure to the inverted one occurs when the width of the quantum well is increased. In QWs with a critical thickness $d_c \approx 6.3$ nm (for the Cd content in the barrier $x = 0.7$), the dispersion laws for electrons and holes near the point of intersection of the bands are analogous to the dispersion law for massless fermions in graphene. However, in contrast to graphene, in which the Dirac cone is present in two valleys, the HgTe cone is located in the center of the Brillouin zone. If the width of the QW HgTe d_{QW} is less than the critical d_c , then the energy spectrum is similar to the charge carrier spectrum in 2D systems based on narrow band A_3B_5 semiconductors: the electron subbands at

$k = 0$ are made from the band states of electrons (the Γ_6 symmetry group) and the light-holes, and the main valence subband H1 from the states of heavy-holes Γ_8 . If one consider HgTe/CdHgTe quantum well with the width $d_{QW} > d_c$ then, the lower electron-like subband E1 lies below the upper hole-like subband H1. This inverted ordering of the subbands results in the appearance of a 2D TI state (see Fig. 6). With a further increase in the width of the HgTe/CdHgTe quantum well, the minimum of the conduction band located in the center of the Brillouin zone and the lateral maxima ($k \neq 0$) of the valence band approach each other, finally at $d_{QW} > d_{SM} \sim 12$ nm the state of the 2D semimetal is realized in the quantum well [72].

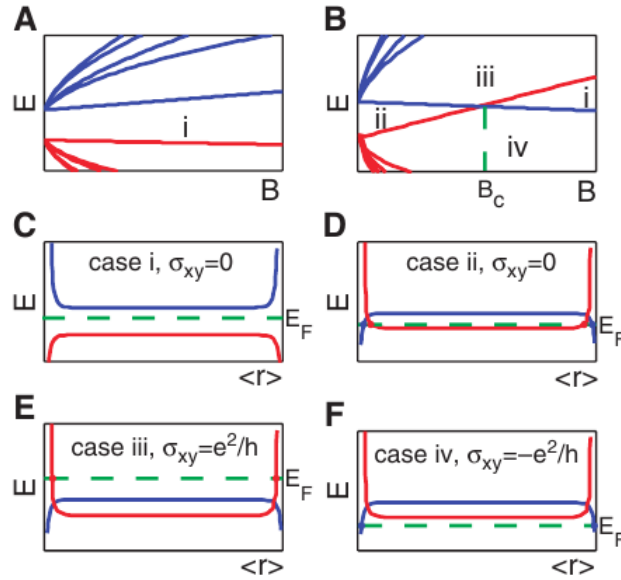


Fig. 6. Bulk and edge state spectrum of the two-band Dirac model in the presence of an external orbital magnetic field. (A) The bulk Landau levels in the normal regime. (B) The bulk Landau levels in the inverted regime, where zero-mode Landau levels cross at a finite magnetic field B_c . The crossing divides the phase diagram of gate voltage and magnetic field into four regimes, labeled (i) to (iv). (C) The low-lying bulk and edge state energies as a function of the centers of the Landau orbitals in the normal regime. (D) The low-lying bulk and edge state energies as a function of the centers of the Landau orbitals for the inverted regime, where the Fermi energy lies in-between the two bulk inverted Landau levels. The Fermi energy crosses the Landau levels, giving rise to the pair of counter propagating edge states. When the magnetic field is increased, the two lowest-lying bulk Landau levels approach each other, and they cross the Fermi energy in a different order, depending on the value of the gate voltage. The crossing of the Fermi energy by one of the Landau levels gives rise to either the n - or the p -type QHE for the cases shown in (E) and (F). From [58].

One should extend the topic to a three-dimensional topological insulator, where massless Dirac fermions are realized not in edge states, but in surface states. The thick (80-100 nm) HgTe film grown on a substrate with a larger lattice constant (the so-called "strained HgTe" in Ref. [81]) is a three-dimensional topological insulator because the deformation opens a band gap in the bulk material between bands of light and heavy holes, and for particular position of Fermi level conductivity occurs over surface states [82-85].

One of the consequences of the strong spin-orbit interaction in HgTe/CdTe systems with a structural asymmetry (due to asymmetric doping of barriers or application of the gate voltage) is the appearance of the giant spin splitting in a zero magnetic field [24, 57, 59] (also known as the Bychkov-Rashba splitting [86]). Up to now, the magneto-optics in asymmetric QWs with inverted band structures has been studied only in [24, 25], where along with the beating patterns in the Shubnikov-de Haas oscillations (compare [25, 57, 59, 87]), the splitting of the cyclotron

resonance line was observed. The sample with a HgTe/CdTe quantum well with a width of $d_{QW} = 11.5$ nm were studied in work [24], where the semitransparent gate allowed authors to increase the electron concentration up to $n_s \approx 10^{12}$ cm $^{-2}$ in magnetic fields up to $B = 8$ T. Doubled-peaked CR line was observed and associated with the splitting of the lower subband of the conduction band at $B = 0$, but the interpretation of the results was based on the incorrect assumption, that Rashba splitting is linear in k in this system.

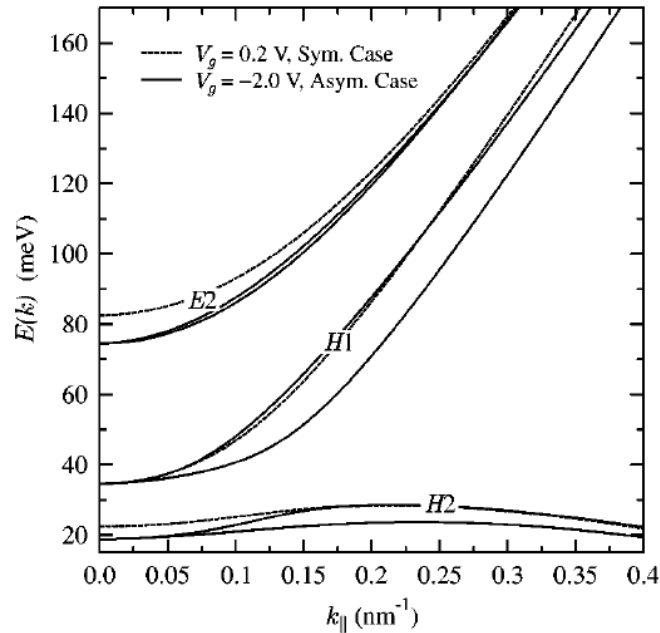


Fig. 7. Self-consistent calculations of the dispersion law $E(k)$ for a symmetric (dashed) and asymmetric (solid) potential controlled by the gate voltage in a sample with $d_{QW} = 21$ nm. From [57].

In subsequent works, magnetotransport studies of symmetric and asymmetrically doped structures with QWs were performed, where the splitting between the bands was estimated from the positions of the beating nodes of the SdH oscillations. Thus, in [57] the gate voltage is used not only to control appearance of the oscillations but the depopulation of the subband E2 (see Fig. 7). In [59], a splitting of up to 30 meV was obtained, and in [87] the hysteresis effect caused by charging the semiconductor and insulator heterojunction was investigated, thus undermining previous works on gated samples, usually ignoring effect. A heterostructure with a QW of width $d_{QW} = 15$ nm with one-sided selective barrier doping in magnetic fields up to $B = 5$ T was investigated in Ref. [25]. A strong (up to 12%) splitting of the CR line was found, and based on analytical estimates, a conclusion was made about the giant (up to 30 meV) spin splitting of Rashba (compared with [59]).

The minimum of the band gap in CdHgTe is located at the Γ point of the Brillouin zone, which excludes valley degeneracy in this system. In a magnetic field, the classical two-dimensional system has a discrete (and equidistant in the case of parabolic dispersion) spectrum of Landau levels, where each spin pair is separated by the value of Zeeman energy $E = g\mu_B B$. One of the key features of CdHgTe is the fact that the magnitude of spin splitting can be comparable to the value of cyclotron splitting $\hbar\omega_c$, which aroused interest of researchers trying to determine the value of the system's g -factor. In the above-mentioned paper [53], a simple two-band model was used to fit the g -factor value of 20. An unusually large value for this quantity was reported in [60], mentioning non-monotonous g -factor dependence on the filling factor in structures with asymmetric potential. Additionally, the spin splitting was investigated

via the coincidence method in Refs. [60, 88, 89], while the values of the g -factor were determined within two ranges 15-35 and 50-60 in various works.

1.1.3 Double quantum wells

As already discussed, the band structure of the HgTe/CdHgTe quantum well is rearranged from the normal (CdTe-like) to the inverted when the HgTe width is increased. At the critical width of the QW $d_c \sim 6.3$ nm, the conduction band and the valence band are engaged, the dispersion law of charge carriers becomes linear (massless Dirac fermions) similar to a single-layer graphene [18]. Accordingly, it can be expected that the band structure of the double HgTe QWs (two HgTe QWs separated by a tunnel-transparent CdHgTe barrier) under certain conditions will be similar to the band structure of bilayer graphene [90, 91]. However, the presence of a tunnel-transparent barrier in the double QW HgTe opens additional possibilities for the engineering of the energy spectrum in comparison with double-layer graphene since barrier thickness controlled during growth. The band structure of double HgTe QWs was studied for the first time in the works of the group P. Michetti [92-94] on the generalized "two-zone" Bernevig-Hughes-Zhang model (BHZ) [18]. The authors demonstrated that applying a sufficiently strong vertical electric field makes an inversion of the bands possible: a hole-like subband H1 "related" to one QW is higher in energy than an electron-like E1 related to another QW, even if the individual quantum wells have a normal band structure ($d_{QW} < d_c$), *i.e.* there is a topological transition to the inverted band structure. It should be noted that the BHZ model even in a single HgTe QW is applicable in a very limited energy region [95], and the region of applicability of the "generalized Michetti model" to double QWs has not been investigated so far. The first theoretical study of the band structure of DQWs based on the four-band Kane model was carried out in [67], where a phase diagram of symmetric double HgTe/CdHgTe QWs was constructed as a function of the thicknesses of the HgTe well layers and the CdHgTe tunneling-transparent barrier. In particular, it was found that when the band are inverted, the system passes into a specific gapless phase that exists in a wide range of layer thickness values, which exhibits many properties inherent to a two-layer graphene.

The band structure of DQWs was calculated using the four-band $\mathbf{k}\cdot\mathbf{p}$ Hamiltonian as a kinetic energy operator [67]. In the used Hamiltonian, the interaction of the conduction band Γ_6 with the valence bands Γ_8 and Γ_7 is included exactly, and the interaction with the other bands is taken into account by perturbation theory. Such an approach allows one to calculate correctly the nonparabolicity of the size-quantized subbands, the spin-orbit interaction, and the value of the built-in elastic deformations. Latter appears due to the difference in the lattice constants of the material in the QW plane for structures grown on the CdTe buffer. The calculation of the wave functions was carried out by the method described in [27]. The essence of the calculation method consists in considering a superlattice with a sufficiently long period instead of one double QW [45]. Due to large thickness of the barriers between adjacent double QWs in the superlattice, the tunneling of the charge carriers can be neglected, thus the wave function periodicity condition with period $d_{SL} > d_{QW}$ is used as boundary conditions. The electronic wave function in this model has eight components. Each component was expanded in terms of spatial harmonics:

$$\begin{aligned} \psi_j(x, y, z) &= e^{-ik_x x + ik_y y} \sum_{n=-N_{max}}^{N_{max}} C_n(k_x, k_y) e^{-i\frac{2\pi Z}{d}n} = \\ &= e^{-ik_x x + ik_y y} \varphi_j(x, y, z), \end{aligned} \quad \text{Eq. 1}$$

where k_x, k_y are the components of the electron wave vector in the quantum well, and z is the coordinate perpendicular to the QW plane, $(2N_{max} + 1)$ is the number of spatial harmonics in

the expansion, the index j denotes the component of the wave function, and $C_n(k_x, k_y)$ are the coefficients of the expansion. It was further assumed that the QW was grown on the (013) and $x \parallel [100]$, $y \parallel [03-1]$, $z \parallel [013]$ planes. The calculation of the energy spectrum and wave functions with this approach comes to finding the eigenvalues and eigenvectors of a matrix of dimension $8(2N_{max} + 1) \times 8(2N_{max} + 1)$. In the calculations, the material parameters from [61] were used.

In Fig. 8, the results of the band structure calculations are presented for symmetric DQWs with a rectangular potential profile. The energy dependences at $\mathbf{k} = 0$ of electron (E) and (H) hole-like subbands versus the thickness of the separation barrier t are given in the panels Fig. 8 (A, B). There are two particular scenarios: when the thickness d of each two QWs is $d_c/2 < d_{QW} < d_c$ (A) and $d_{QW} > d_c$ (B), where d_c is the critical thickness for a single QW. At an infinite thickness of the separation barrier, the states in the double quantum well do not differ from the states in two isolated QWs, and for a finite thickness (for tunnel transparency) of the barrier t , splitting of each pair of subbands into even and odd states occurs. If t close to zero, then the energies of the subzones tend to the corresponding values in a single quantum well of thickness $2d$. It can be seen that the splitting of electron-like states (E) is much greater than the splitting of hole-like states (H), which is associated with a significant difference in effective masses in electron- and hole-like subbands at $\mathbf{k} = 0$, the values of which determine the tunneling transparency of the barrier for a given t .

There are two types of band ordering in the symmetric DQWs, depending on the thickness d_{QW} of each QW. The first case is shown in Fig. 8 (A), when parameter varies as $d_c/2 < d_{QW} < d_c$. In this case, the subband E2 is always located above the subzone H2; there is an inversion of the subbands E1 and H1 (with a change in t). For large values of t , the subband E1 lies higher in energy than the subband H1, and the system has a normal band structure (see the inset in Fig. 36). As the thickness of the separation barrier t decreases, the E1 subband energy decreases, while H1 practically does not change, thus at some value of t the gap in the state spectrum collapses. With a further decrease in t of the subband, E1 goes down to the valence band, and a gapless state is formed that resembles a bilayer graphene, when two parabolic subbands H1 (the lower subband of the conduction band) and H2 (the upper subband in the valence zone) touches at the point $\mathbf{k} = 0$, see the inset in Fig. 40. If the thickness of the separation barrier becomes very small, then, finally, the splitting of the subbands H1 and H2 occurs, i.e. the system goes into the 2D state of a topological insulator, as is the case for a single HgTe QW.

The second type of band ordering, shown in Fig. 8 (B), is realized for $d_{QW} > d_c$. In this case, the subband E1 always lies below H1. At a small thickness of the separation barrier of the subband, E2 lies above H2, and with an increase they intersect, which also leads to the formation of a Dirac cone at the Γ point (as in the intersection of E1 and H1).

The phase diagram of the system on the d - t axis is shown in Fig. 8 (C). Thick black lines correspond to the appearance of Dirac cones at the Γ point. The left line corresponds to the intersection of the sub-zones E1 and H1, the right — E2 and H2. If the thickness of the separation barrier is sufficiently small, then the subbands H1 and H2 are separated, and the inversion of the subbands E1 and H1 leads to a topological phase transition between the states of the trivial (band, BI) and topological (TI) insulator (corresponds to the orange area on Fig. 8 (C)). For relatively wide QWs, a semi-metallic state corresponding to the shaded region in Fig. 8 (C). It is characterized, as in the case of a single QW for $d_{QW} > d_{SM}$, by the disappearance of the "indirect" forbidden band, when the energy of the "lateral" maximum in the valence band exceeds the energy of the bottom of the conduction band. The above-mentioned metal phase (gapless state) of the "two-layer graphene" (bilayer graphene, BG) corresponds to the blue region on the colored one in Fig. 8 (C). Its lower blurred boundary is determined, in fact, by the splitting conditions of the subbands H1 and H2, when the separation barrier becomes tunnel-transparent for hole-like states.

Another unique property of the double QW HgTe is the existence of massless Dirac fermions in the range of parameters corresponding to the inverted band structure. The occurrence of this Dirac branch caused by the intersection of the second electronic level E2 and the hole-like H2 level. Note that the region BI to the right of BG in Fig. 8 (C), where the inversion of the levels E2 and H2 occurs, corresponds to a trivial, rather than a topological insulator. Two pairs of helicoidal edge states arise in this region, and the gap opens in their spectrum as a result of their interaction [67].

1.2 Heterostructures InAs/GaSb

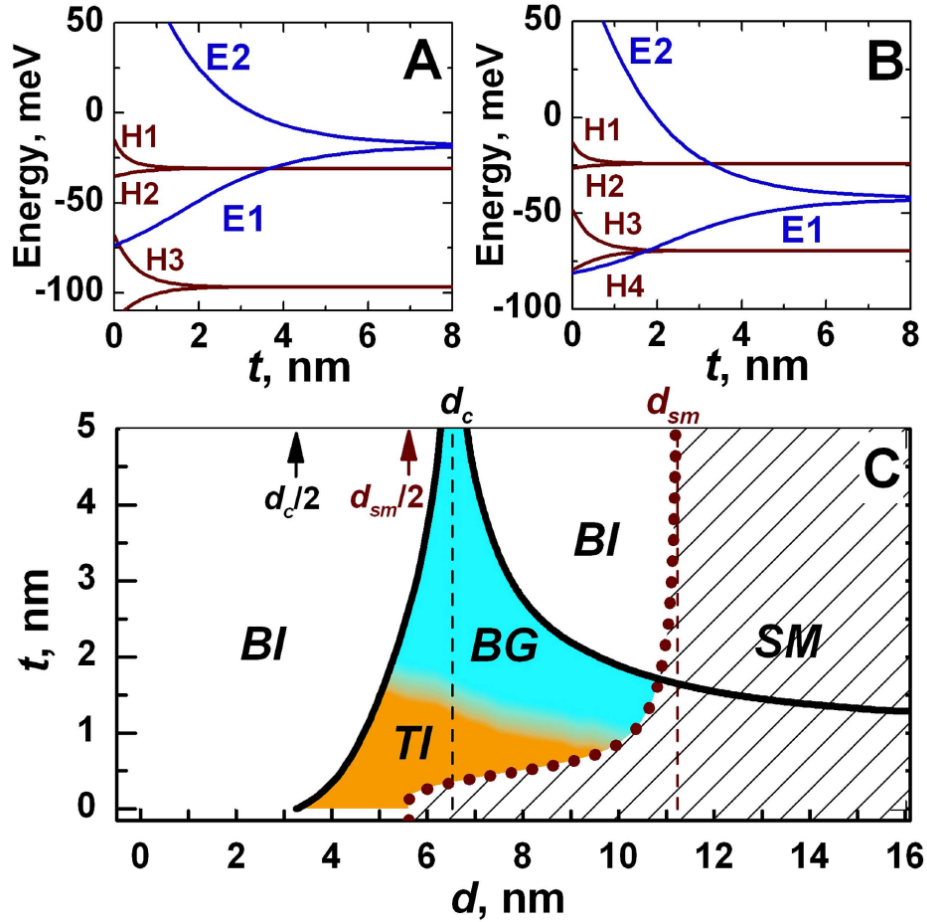


Fig. 8. (A,B) Energy of E1, E2 (both in blue) and H1, H2 (both in red) bands at $k = 0$ versus barrier thickness t at different quantum well thickness d : (A) $d_c/2 < d_{QW} < d_c$ and (B) $d_{QW} > d_c$. (C) Phase diagram of double HgTe QW. The values d_c and d_{SM} correspond to thickness of the single QW, at which Dirac cone and semimetal phase arise respectively. The white-open regions are the band insulator phase, while the white-striped region corresponds to the semimetal phase, when the side maxima of valence subband exceed the bottom of conduction subband. The orange and blue regions conform to topological insulator and BG phase, respectively. The bold black curves correspond to the arising of the Dirac cone at the Γ point. We note that the scales of d_{QW} and t in the phase diagram can be efficiently increased by changing x and y in the alloys of $\text{Hg}_y\text{Cd}_{1-y}\text{Te} / \text{Cd}_x\text{Hg}_{1-x}\text{Te}$ DQWs. From [67].

The two-layer InAs / GaSb QWs are the second semiconductor system in which the state of a two-dimensional topological insulator was predicted theoretically [96] and then discovered experimentally [97]. The GaSb valence band edge is by 0.15 eV higher than the bottom of the conduction band in InAs, which makes it possible to control the band structure of the two-layer InAs / GaSb QW by selecting the layer widths. Moreover, QW itself bounded by AlSb barriers

(specific material with a large bandgap) to provide overall confinement. In the case of thin layers, the size quantization pushes the lower electron-like band E_1 above the upper hole-like level of H_1 , and the QW has a normal band structure. With thicker layers, the inversion of the bands occurs, when the subband E_1 turns out to be lower in energy than the subband H_1 — the system transforms to the 2D TI state. The lack of the inversion symmetry in the growth direction in the "double-layer" InAs / GaSb quantum wells leads to the "crossing" of the E_1 and H_1 subbands at $k \neq 0$ and, consequently, to the gap opening in the spectrum due to the hybridization of the subbands (see Fig. 9(b)). Thus, in the "double-layer" InAs / GaSb quantum wells, unlike the HgTe / CdHgTe [98], it is impossible to obtain a gapless state with a linear dispersion of massless Dirac fermions at any thickness. It was found in [99, 100] that this 2D system always has nonzero persistent conductivity even if the Fermi level is inside this forbidden zone. In earlier works [101], the origin of the persistent conductivity was associated with the broadening of the levels due to scattering of charge carriers by a random potential. It is interesting that even in the "pure limit" in these papers the conductivity of the 2D system at a position of the Fermi level inside the forbidden band remained finite and did not depend on the scattering parameters. The values of the persistent conductivity were experimentally measured in Ref. [102], which were in better agreement with the theoretical values predicted in [101] and several times higher than the possible contribution of the edge states to the conductivity. However, it has been demonstrated that the persistent conductivity decreases if the system has a direct band structure. Later, more accurate studies of the conductivity at the position of the Fermi levels inside the forbidden band, performed on samples of various sizes, confirmed the existence of edge states with an inverted band structure in the InAs / GaSb quantum well [97, 103, 104].

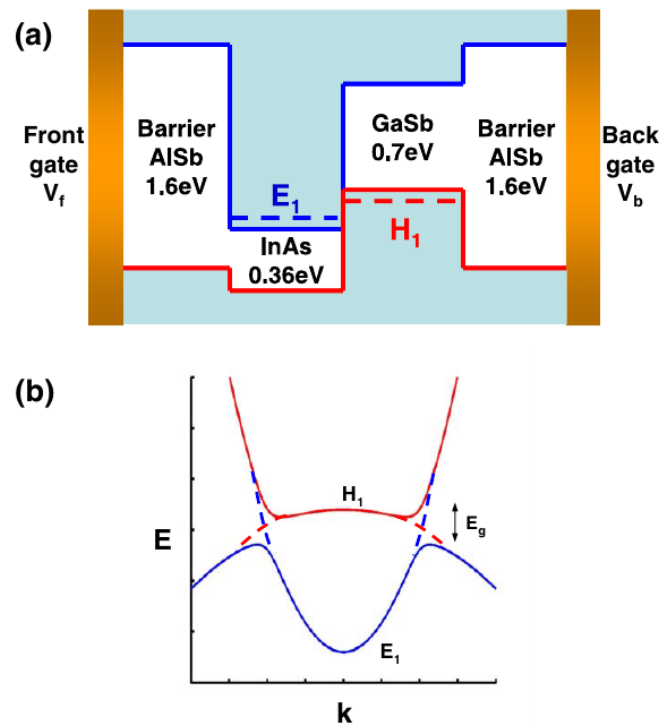


Fig. 9. (a) The band gap and band offset diagram for asymmetric AlSb / InAs / GaSb quantum wells. The left AlSb barrier layer is connected to a front gate while the right barrier is connected to a back gate. The E_1 subband is localized in the InAs layer and H_1 is localized in the GaSb layer. Outer AlSb barriers provide an overall confining potential for electron and hole states. (b) Schematic band structure diagram. The dashed line shows the crossing of E_1 and H_1 in the inverted regime. Hybridization between E_1 and H_1 , opens the gap E_g . From [96].

Magneto-optical studies in double-layer InAs / GaSb QWs were carried out at liquid-helium temperatures long before the boom associated with their nontrivial topological properties took place [105-109]. The observation of the cyclotron mass oscillating behavior was one of the most interesting results, when the amplitude and width of the cyclotron resonance line from the magnetic field in semimetallic samples [105-108]. Subsequently, it was shown that this behavior is a consequence of the hybridization of electronic and hole states. At the same time, in spite of the large number of works devoted to the investigation of CR in InAs / GaSb structures, complete magneto-optical studies in InAs / GaSb quantum wells restricted by AlSb barriers and "intended" to the formation of 2D TI state have not been carried out. The author is aware of a single rather old work in which a bandgap of the inverted spectrum was determined by THz spectroscopy [110] in a two-layer InAs / GaSb structure with AlSb barriers. Studies of the magneto-optical properties of three-layer (see below) quantum wells have not been carried out even at low temperatures.

As was noted in [111] (see also [44]), the addition of one more layer of InAs to the "two-layer" QW InAs / GaSb eliminates the asymmetry in the growth direction and makes the properties of such "three-layer" InAs / GaSb / InAs QWs similar on the properties of QW HgTe / CdHgTe. In particular, for a certain thicknesses of InAs and GaSb layers, a gapless state with a conical dispersion law at the Γ point of the Brillouin zone is realized in the system in a manner similar to the HgTe/CdHgTe of critical width. The first experimental studies of such gapless structures were performed in our work [111], where the spectra of the cyclotron resonance of electrons in classical magnetic fields and their transformation with a decrease in the carrier concentration were studied. The results obtained indicated the presence of two kinds of charge carriers in the conduction band (with parabolic and conical dispersion laws). However, the large number of electron concentration in the studied samples, did not allow shifting the position of the Fermi level closer to the Dirac point.

Chapter 2. Experimental methods

Despite the general title of the section, we try to focus only on particular methods of investigating the band structure that are directly related to the results presented in the thesis. Since the HgTe QW structures are sufficiently transparent in the far-infrared region, the study of transmission spectra and polarization experiments has become very popular [46, 112]. In spite of the fact that transport measurements require additional model analysis, the results of magnetotransport studies have also made it possible to expand knowledge of the band structure of narrow-gap materials with HgTe and InAs / GaSb QWs.

2.1 Magnetooptics with monochromatic sources

In order to study absorption in the IR range a semiconductor sample (usually is a plane-parallel plate or wedged 1-2 degree to eliminate interference effects) is placed in a quasi-optical path perpendicular to the wave vector of radiation propagating along. If the magnetic field is parallel to the wave vector of the radiation, then the optical configuration of the Faraday occurs, if perpendicular — then Voigt. In both cases the detected signal is determined by the real part as well as imaginary part of the conductivity of the free carriers, i.e. the transmitted signal is determined by both absorption and reflection. It's worth to mention, than for Voigt configuration it's possible to study both E||B and E⊥B where different selection rules are applied [113].

To obtain an alternating signal (for the purpose of subsequent amplification and synchronous detection), cyclotron resonance studies use different types of modulation. In the first cyclotron resonance experiments, the amplitude of the microwave radiation was modulated. However, for a small value of the change in the transmission of a sample due to resonant absorption (useful signal associated with absorption at the CR when the magnetic field is swept) appears as a small change in the large signal from the radiation source. In the second case, one could control optical excitation of charge carriers in the sample with additional source located nearby, e.g. LED. In this case, amplitude of the microwave radiation is constant and the recorded signal is entirely governed by absorption of free carriers, amount of which is modulated externally. Additionally, the modulation of the intensity of the external magnetic field is possible, then the signal (proportional to the derivative dT/dH) is recorded, and it is necessary to perform numerical or analog integration of the signal to obtain the absorption spectrum in the usual form.

Researchers often use backward wave tubes (BWOs) as a source of a tunable monochromatic radiation in the millimeter and sub-millimeter ranges. In these ranges, the use of a wedged sample does not allow avoiding interference, but if proper wavelength is chosen it is possible to achieve a situation where the signal is determined only by the real part of the conductivity (as in a Fabry-Pérot resonator where an integer number of half-waves correspond to thickness of the sample). As applied to the HgTe / CdHgTe quantum well, one of the first such studies was made in Ref. [25]. Radiation with frequency $f \sim 600$ GHz sent into the cryostat along a quasi-optical path and measured with sensitive element located behind the sample. The detector is an epitaxial *n*-GaAs film with perceptible photoconductivity and at frequencies below the 1s-2p transition frequency of shallow donors. In work [114], studies were carried out using linearly polarized radiation from backward-wave tubes in the range 0.1-0.9 THz, using a Golay cell or a helium-cooled bolometer as the detector.

At higher frequencies, it is possible to use compact radiation sources such as quantum cascade lasers (QCL), which are conveniently located in the same cryostat with investigated sample. QCL produced by "Trion Technology" (Tempe, Arizona, USA), operating at frequencies of $f = 2.61$ and 4.35 THz, were used in [115]. Another laser with $f = 3.0$ THz was used in Ref. [25]. In measurements with QCL, an impurity photodetector Ge:Ga was used as a sensitive element. In high-frequency pulsed magnetic fields, it is necessary to use lasers of higher frequency: in [27, 116] QCL with a wavelength of $\lambda = 14.8 \mu\text{m}$ and $\lambda = 11.4 \mu\text{m}$ was

used. In the experimental gap between the QCL of THz range and the MIR range, it is also suitable to use semiconductor injection lasers based on PbSnSe with a wavelength of up to $\lambda = 50 \mu\text{m}$ [117], however, have significantly less powerful, e.g. less than $1 \mu\text{W}$.

Bulk samples of CdHgTe was studied using above-mentioned back-wave tubes as well as electrically pumped HCN and H₂O molecular lasers [46, 112, 118]. It is also possible to use gas THz lasers, for example, at $\lambda = 118.8 \mu\text{m}$ ($\hbar\omega = 10.4 \text{ meV}$), where ethanol pumped with CO₂ laser is used as an active substance [73], [119]. Finally, in work [116], the use of a CO₂ laser itself was demonstrated, when studying HgTe / CdHgTe QWs in pulsed magnetic fields.

2.2 Fourier-spectroscopy in magnetic fields

The Michelson interferometer is the main element of the Fourier spectrometer, where the position of one mirror is fixed while the position of the second is controlled by the spectrometer optical bench (it is precisely controlled). In general, the detector obtains a complex space-domain signal (interferogram) as a function of mirror displacement, which is a superposition of harmonic signals. The period of each signal is determined by the frequency and the amplitude is determined by the intensity of the incoherent source. The first part of the term FT-IR coming from the fact that specific mathematical process (Fourier transform) is required to convert the raw data into the actual spectrum, while the second specifies the energy range. Nowadays such spectrometers widely used for “quantitative analysis of complex mixtures, the investigation of dynamic systems, biological and biomedical spectroscopy, microspectroscopy and hyperspectral imaging, and the study of many types of interfacial phenomena” [120].

In our particular case benefits of magnetic field is employed. For a fixed value of B -field "raw" spectrum contains superimposed features of the emission spectra of a broadband source (mercury lamp or globar), reflections of the beamsplitter, the sensitivity of the photodetector, and finally, the transmission of the sample under study. Luckily, features of the optical configuration depends weakly on the value of magnetic fields, thus in the first step the normalization by the zero-field spectrum allow distinguishing sample specific response. In addition, one can use the spectrum of the empty optical path to exclude field-dependence of setup (e.g. bolometer) as second step. Before we proceed, we refer to PhD thesis of M. Hakl for alternative description of setup [121], since here we focus on related techniques in the following.

In the LNCMI (Grenoble, France), where the author has performed most of the spectral investigations in this work, the sample and the bolometer both placed in standalone-sealed insert aka “probe” with optical filter on top, then pumped and filled with an exchange helium gas. Then the prepared probe is introduced in a helium cryostat with a superconducting solenoid (Fig. 10). There are various spectrometer configurations (i.e. source/beam splitter), probe top filter and extra filter just before vacuum-sealed composite silicon bolometer, depending on the purpose of the experiment. For example, for low energy studies, a mercury lamp can be used as a source, a Multilayer Mylar T222 or Mylar $50 \mu\text{m}$ as a beam splitter, white or black (to avoid exposure of the sample to shortwave radiation) polyethylene as an probe top filter and a bolometer with a silicon or white polyethylene filter. In the MIR region, the globar gives a sufficient signal in combination with a KBr-based beamsplitter, ZnSe can be used as probe filter, but such a configuration inevitably leads to exposure of the sample to short-wave radiation.

In this setup, not only the transmission, but also the photoconductivity in a wide range of energies can be investigated, which, in particular, makes it possible to estimate the width of the forbidden band [115]. According to experimental results in [122] it is possible to distinguish the normal and inverted band structure from the shift of the red boundary of the interband PT as the temperature changes.

Polarization-sensitive experiments are greatly informative magneto-optical studies. In the case of a classical CR, the sign of the charge carriers can be determined from the type of circular polarization of the transmitted/adsorbed radiation (see, for example, Refs. [73-75, 123]) or the

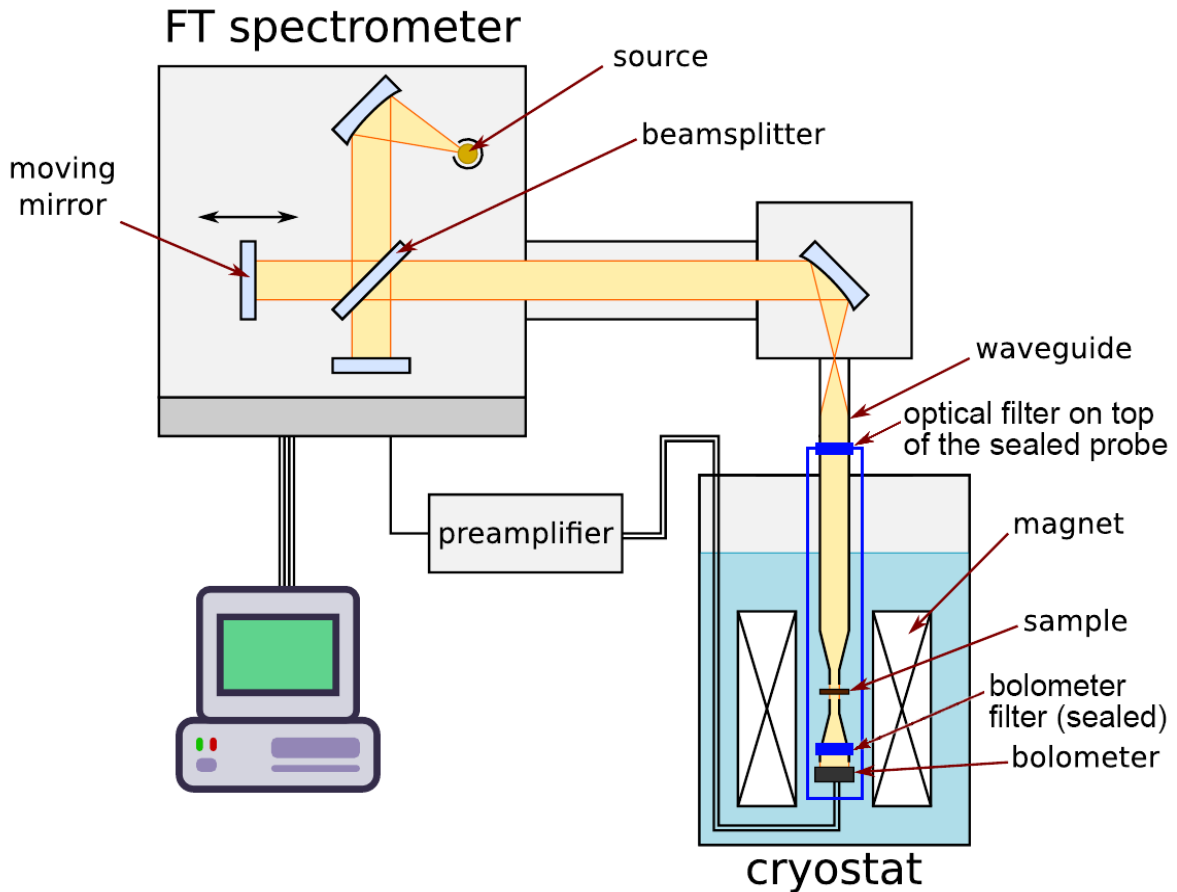


Fig. 10. Scheme of setup for measuring transmission spectra in a magnetic field. From [45].

sign of the Faraday effect for linearly polarized radiation, as was demonstrated in Ref. [124] for a stressed layer of HgCdTe and in [125] for graphene. In experiments with monochromatic radiation, $\lambda/4$ -plates or their analogs can be used to produce circularly polarized light (see, for example, [126, 127]). The difficulty lies in the fact that for a broad range of energies it is necessary to use many plates, moreover, the main material of the plates is quartz, which is opaque in most of the middle and far IR ranges $\hbar\omega > 300$ meV ($\lambda > 4$ μm). An alternative can be the use of photoelastic modulators based on piezo-birefringent crystals [128], but the range is again limited to wavelengths of $0.3 > \lambda > 2.5$ μm . The most complex experiment is ellipsometry in a magnetic field [129], where the complexity of the analysis is related to the inevitability of mixing the z component of the conductivity tensor, which forces us to use Mueller matrices. In the Fourier spectroscopy method, the best alternative is to study the Faraday rotation. A simple technique for such measurements was proposed in [130] and it was demonstrated that the advantage of polarization experiments can be used not only for classical CR, but also for studying transitions between Landau levels in quantizing magnetic fields.

2.3 Thermally activated conductivity

Magneto-optical measurements of the resonant absorption in quantizing magnetic fields do not provide a direct experimental method to estimate the spin splittings of the Landau levels, since electric-dipole transitions between such states are forbidden by selection rules. At the same time, if one could control the position of the Fermi level and ensure its sequential movement through the Landau levels (for example, via gate voltage), then the position of the Landau levels in a magnetic field can be established using magnetotransport measurements [131, 132]. In HgTe/CdHgTe heterostructures, the spin splitting was studied also with the

coincidence method [60, 88, 89], g -factors in the range of 15–35 or in the range of 50–60 have been reported depending on the structure used in the experiment.

To determine the energy distances between neighboring Landau levels in the HgTe/CdHgTe quantum well, one can make use of activation magnetoconductivity in perpendicular magnetic fields [133–135]. If the Fermi level lies in the region of localized states between Landau levels, then the thermal excitation of electrons into delocalized states in the upper Landau level should lead to an activation behavior of the conductivity with increasing temperature. Thus, by analyzing the temperature dependence of the amplitude of the SdH oscillations for a chosen filling factor, it is possible to determine the magnitude of the mobility gap Δ_T . A similar technique made it possible to detect a constant nonzero density of states in GaAs/Al_xGa_{1-x}As structures [134], between narrow Landau levels of width $\Gamma_G = 0.25\sqrt{(B/T)}$ meV [136].

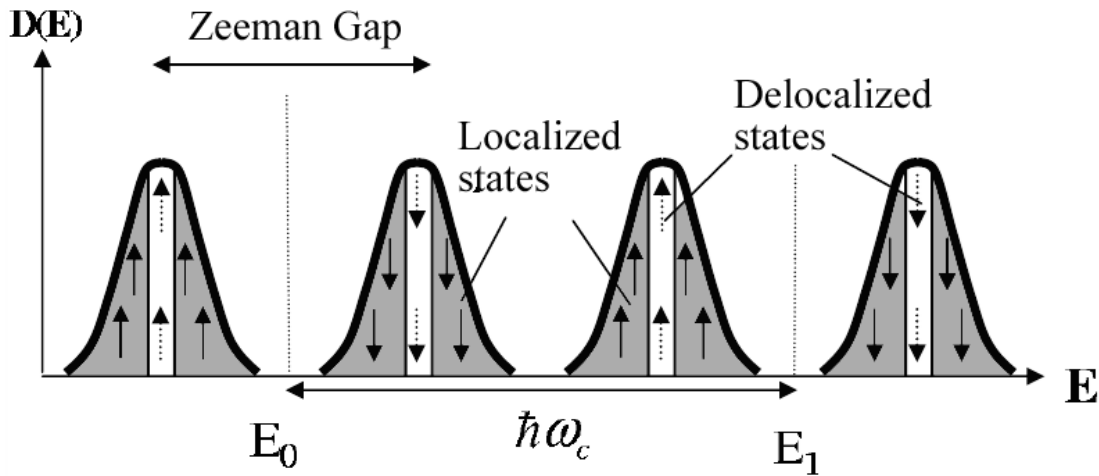


Fig. 11. The scheme of the density of states at the Landau levels in the presence of a random potential. From [137].

The presence of scattering centers in two-dimensional systems leads to a broadening of the Landau levels, a description of which is devoted to a large number of studies, which are reviewed in Ref. [133]. In the very first work by Ando [138], a self-consistent Born approximation was used, giving rise to a semielliptical form of the peak of the density of states. In the one-electron approximation, the Landau level broadening depends on the level index, as it is determined by the ratio of the characteristic length between random scatters and the extension of the electron wave function on a given LL. In the limit of a smooth potential, the approach proposed by Gerhardt [139] is more appropriate. The average over all types of scattering is taken and the level broadening is expressed in terms of the quantum lifetime $\Gamma_L = \hbar/2\tau_q$. The inclusion of many-body interaction effects greatly complicates the description and can lead to a significant difference from the "one-particle" results.

The Lorentzian [158, 160, 161], Gaussian [156, 162], or semi-elliptical [163] shape of broadened LLs can be considered. In studies [56, 141] devoted to HgTe/CdHgTe QWs, the Gaussian model of the density of states with the parameter $\Gamma_G \sim (B)^{1/2}$ was used. We note that such a square root dependence of the width of the density of states corresponds to the short-range (δ -correlated) random potential [163, 164]. In the later work [59], focused on asymmetrically doped HgTe/Hg_{0.3}Cd_{0.7}Te heterostructures, the broadening Γ of LLs was assumed to be independent of magnetic field. In the Lifshitz–Kosevich model [165, 166], there is an approach that allows one to directly determine the type of scattering centers in a system and calculate the broadening value. This was made for different high-mobility 2D systems (see, for example, [142]). However, for the case of HgTe/CdHgTe QWs, this approach was fully applied only in our previous study [167]. In [55], this approach was only used to determine the effective mass in the HgTe QW with the standard band structure.

The most common methods of studying the density of states in two-dimensional systems are based on measurements of the oscillations of thermodynamic quantities in a transverse magnetic field [133], such as, for example, magnetization, electronic heat capacity, and conductivity. Of interest for such studies are systems with a large mobility of charge carriers, including the HgTe QWs. For the first time, the electronic properties of two-dimensional systems were considered in inversion layers of silicon [138], where the enhancement of the effective g -factor due to the exchange interaction was observed [140]. A large contribution to the study of magnetotransport phenomena in heterostructures based on mercury cadmium telluride with substrate orientation (1 0 0) was made by a group of scientists from Würzburg. To calculate the changes in the density of states in a magnetic field, they used a simplified theory [139] with the arbitrary broadening parameter of the Landau levels. In [56], the structure of the valence band in the HgTe/Hg_{0.3}Cd_{0.7}Te quantum well with a width d_{QW} from 12 to 20 nm was studied via magnetotransport methods. Irregular patterns in the SdH oscillations (see Fig. 2 in [56]) are typical for samples with a p -type conductivity. Gaussian broadening model with the parameter Γ_G , which depends on the magnetic field as $\Gamma_G \sim \Gamma_0 \sqrt{(B/T)}$ where $\Gamma_0 = 0.2$ meV was applied.

Samples of n -type with $d_{QW} = 20$ nm with symmetric and asymmetric doping were investigated in work [141]. The authors point out the absence of intersubband scattering, relying on the excellent agreement between the results of the experiment and the theoretical calculation of the density of states. In this case, the parameter $\Gamma_0 = 1.5$ meV became larger. In a later paper [59], a model with a parameter Γ independent of the magnetic field was used to calculate the density of states in asymmetrically doped heterostructures HgTe/Hg_{0.3}Cd_{0.7}Te with $d_{QW} = 12.5$ nm. The best agreement between theory and experiment was obtained with $\Gamma = 2.5$ and $\Gamma = 2.8$ meV for two different samples cut from the same heterostructure. The broadening of the Landau levels must be taken into account in the quantitative description of the magnetoabsorption spectra as well. Authors in [26] simulate absorption spectra for structures with $d_{QW} = 12.2$ nm. In this case, a constant magnitude of the broadening equal to 5 meV was used.

The literature review presented in this section shows that the broadening parameter in all of the works on the HgTe QW was used only as an adjustable parameter, either to calculate the density profile of states and to quantify the Shubnikov–de Haas oscillations, or to explain the magnetoabsorption spectra. It is unclear whether the parameter Γ depend on the magnetic field or on the temperature. Does it have the form of Gaussian or Lorentzian function? On the other hand, within the framework of the Lifshitz-Kosevich theory, there is an approach that allows one to directly determine the nature of the scattering in the system and calculate the magnitude of the broadening, which has been done for other high-mobility systems [142]. However, there is no much analogous studies for MCT and no clear approach on Landau level broadening. In [143], the effective mass and the g -factor was determined neglecting the broadening completely.

Chapter 3. Observation of symmetry lowering effects in HgTe single quantum wells with a rectangular potential

The Landau level spectroscopy technique has been used to explore the electronic structure of the valence band in a series of p-type HgTe/HgCdTe quantum wells with both normal and inverted ordering of bands. We find that the standard axial-symmetric 4-band Kane model, which is nowadays widely applied in physics of HgTe-based topological materials, does not fully account for the complex magneto-optical response observed in our experiments — notably, for the unexpected avoided crossings of excitations and for the appearance of transitions that are electric-dipole forbidden within this model. Nevertheless, reasonable agreement with experiments is achieved when the standard model is expanded to include effects of bulk and interface inversion asymmetries. These remove the axial symmetry, and among other, profoundly modify the shape of valence bands.

- Bovkun, L.S., et al., Landau level spectroscopy of valence bands in HgTe quantum wells: Effects of symmetry lowering. <https://arxiv.org/abs/1711.08783>, 2018 (with referees).
- Ikonnikov, A.V., et al., On the Band Spectrum in p-type HgTe/CdHgTe heterostructures and its transformation under temperature variation. *Semiconductors*, 2017. 51(12): p. 1531-1536.
- Bovkun, L.S., et al., Polarization-sensitive Fourier spectroscopy of HgTe quantum wells. *JETP Letters*, 2018. 108(5): p. 352 (in print).

In recent years, there has been a considerable interest in HgTe/CdHgTe quantum wells (QWs) with narrow-gap or even gapless electronic band structures. Most notably, QWs with an inverted band structure (HgTe QW with a width larger than $d_c \sim 6.3$ nm) are the very first experimentally identified topological insulators and thus opened a completely new field for condensed matter physics [6, 131]. Among other recent achievements on HgTe/CdHgTe heterostructures, one may mention the realization of stimulated emission (due to interband electron-hole recombination) demonstrated at wavelengths up to 20 μm [43, 62]. This is possible thanks to a relatively low electron-hole asymmetry of the band structure in narrow-gap HgTe QWs, which seems to efficiently suppress the non-radiative Auger recombination (see, *e.g.*, Ref. 4 and references therein).

To describe electronic bands in HgTe/CdHgTe QWs, the 4-band Kane model with an axial symmetry (along the growth axis) is traditionally employed. This model proved itself to describe fairly well results of magnetotransport [57, 59-61] and magneto-optical [23-33] experiments in *n*-type samples, where effects of strong spin-orbit interaction (for instance, giant Rashba-type spin splitting [59]) were demonstrated. However, experiments performed on *p*-type HgTe/CdHgTe QWs [71, 77, 78] have revealed effects that cannot be explained within the axial approximation. In Refs. [78] and [71], these effects of large spin-splitting of electronic states in the valence band were attributed to the symmetry lowering, which emerges due to the anisotropy of the chemical bonds at HgTe/CdHgTe heterointerfaces and which gives rise to a strong mixing of electronic states [70].

In general, there are at least three reasons why the axial model can be in certain cases insufficient for the realistic description of electronic states in HgTe/CdHgTe QWs. The first reason is due to neglected “cubic” terms, which become important when side maxima (at non-zero momenta) are considered in the valence band (see, *e.g.* [71]). Two other reasons are related to the bulk inversion asymmetry (BIA) and interface inversion asymmetry (IIA), which also reduce the symmetry of the Hamiltonian and result in a significant spin splitting (as large as 10 meV) of the energy spectra (see, for instance, Refs. [23], [63, 64, 68] and references therein).

All these effects lead to the interaction of the states which are orthogonal in the axial approximation, in the valence band, in particular, thus giving rise, *e.g.*, to the mixing of Landau levels (LLs) with different indices. Let us also note that the role of BIA and "cubic" terms has been in the past extensively explored in the context of bulk germanium [144, 145] and many other zinc-blende semiconductors [146, 147]. However, their impact on electronic states in 2D systems remains much less explored, in particular, when the valence bands in HgTe QWs are concerned. Besides that, there are other effects beyond the axial approximation – described, for instance, by Rashba terms. These are, however, neglected in this our work, which is justified by quantitative estimates presented in the Supplementary Material of work [148].

So far, the clearest experimental evidence of the state mixing is the avoided crossing of “zero-mode” Landau levels (LLs) in HgTe/CdHgTe QWs with an inverted ordering of bands, which was reported in Ref. [63] for HgTe/CdHgTe (001) QWs and reproduced later on in Refs. [23] and [68] for QWs grown on the (013) plane. In the axial model, the wave functions of zero-mode LLs $n = -2$ and $n = 0$ are orthogonal, and for an inverted band structure, these LLs cross at the critical magnetic field B_c , which corresponds to the phase transition from the 2D topological insulator to the normal Quantum Hall effect state [26]. In earlier studies, see, *e.g.*, Fig. 2(b) in Ref. [61], it was shown that the cubic terms in the Hamiltonian do not result in a pronounced interaction (and avoided crossing) of zero-mode LLs in HgTe/CdHgTe(001) QW. In Refs. [63, 64, 68], BIA was proposed to be responsible for this effect, however, recent atomistic calculations [70] indicate that the asymmetry due to chemical bonds at the heterointerfaces (IIA) [149] may prevail over BIA.

In this work, we present a detailed magneto-transmission study of *p*-type HgTe/CdHgTe QWs, providing us with solid experimental evidence for the lack of the axial symmetry in the band structure of these systems. The missing axial symmetry affects the valence band in particular, which is significantly flatter than the conduction band, and therefore, characterized by the considerably larger density of states and smaller spacing of Landau level. Our experimental data are confronted with results of the band structure calculations performed in both, axial 4-band Kane model and its advanced version, which takes account of cubic, IIA, and BIA effects.

3.1 Experimental details

The samples under study were grown by molecular beam epitaxy on semi-insulating GaAs (013) substrates with an ellipsometric control of the layer thickness and composition [14, 150]. A thin ZnTe buffer, thick relaxed CdTe buffer, 40-nm lower $\text{Cd}_x\text{Hg}_{1-x}\text{Te}$ barrier, HgTe QW, and 40-nm $\text{Cd}_x\text{Hg}_{1-x}\text{Te}$ top barrier were grown one by one without any intentional doping. The heterostructure was covered by a 40-nm-thick CdTe capping layer to insure stability of active layer. Native defects (dominantly mercury vacancies) imply the *p*-type conductivity of as-grown samples, with the hole concentration below 10^{11} cm^{-2} . A set of samples with different QW width was prepared, in order to achieve normal, gapless as well as inverted regimes of the band structure. The relevant parameters of the explored samples are presented in Table I.

Table I. Growth parameters and electrical properties (at $T = 4.2$ K) of the studied samples.

Sample	QW width, d (nm)	Barrier Cd composition, x	Bandgap, E_g (meV)	Band structure	Hole concentration	
					without illumination, p_{\max} (10^{10} cm $^{-2}$)	under maximal illumination, p_{\min} (10^{10} cm $^{-2}$)
A (110622)	4.6	75	60	normal	9.0	7.4
B (160126)	5.0	70	40	normal	7.4	insulating
C (110623)	5.5	62	15	normal	6.6	4.7
D (110624)	6.0	62	5	near gapless	3.2	3.0
E (151214)	8.0	86	-20	inverted	11.0	11.0

The magneto-optical experiments were performed in the Faraday configuration in magnetic fields up to 11 T delivered by a superconducting coil [23, 28, 63]. Samples were kept in the low-pressure helium exchange gas at the temperature of 4.2 K. Globar or mercury lamp was used as broadband sources of infrared radiation. The radiation, analyzed by a Fourier transform spectrometer, was guided through black polyethylene (PE) or ZnSe entrance window of the sealed probe, delivered via light-pipe optics to the sample and detected by a composite silicon bolometer placed below the sample. The collected spectra are presented in this paper in the form of relative magneto-transmission, T_B/T_0 , corrected for the field-induced changes in the response of the bolometer, which is a smooth function of the photon energy, which monotonously increases with B in the explored range of magnetic fields.

The transport data were collected using the standard van der Pauw method simultaneously with the magneto-optical measurements. All the explored samples showed pronounced Shubnikov-de Haas oscillations and the quantum Hall effect in the “dark” state, *e.g.*, without illumination. To change the position of the Fermi energy, the hole concentration in the QW was decreased by means of illumination (taking advantage of the persistent photoconductivity (PPC) effect, see, *e.g.*, Ref. [27]) by a blue light emitting diode (LED) located near the sample. Magneto-optical measurements in the energy range above 80 meV were performed with the ZnSe entrance window on the probe, thus allowing us to illuminate the samples with the middle infrared spectrum of globar (blocked when the black PE entrance window was used). In the latter case, some of the samples showed nearly insulating behavior with the Fermi level lying within the band gap.

To illustrate this, the evolution of the longitudinal resistance of sample B after illumination by a blue LED in three subsequent steps is shown in Fig. 12. In periods without any LED illumination, no changes in the longitudinal resistance were observed. This allowed us to perform magneto-optical and magneto-transport measurements at several fixed hole concentrations. The stages LED₁ and LED₂ were achieved after one and two successive doses of illumination, 6 and 12 minutes, respectively. The stage LED₃ with a rather high value of R_{xx} , and therefore with the Fermi level in the midgap position, has been obtained under permanent illumination.

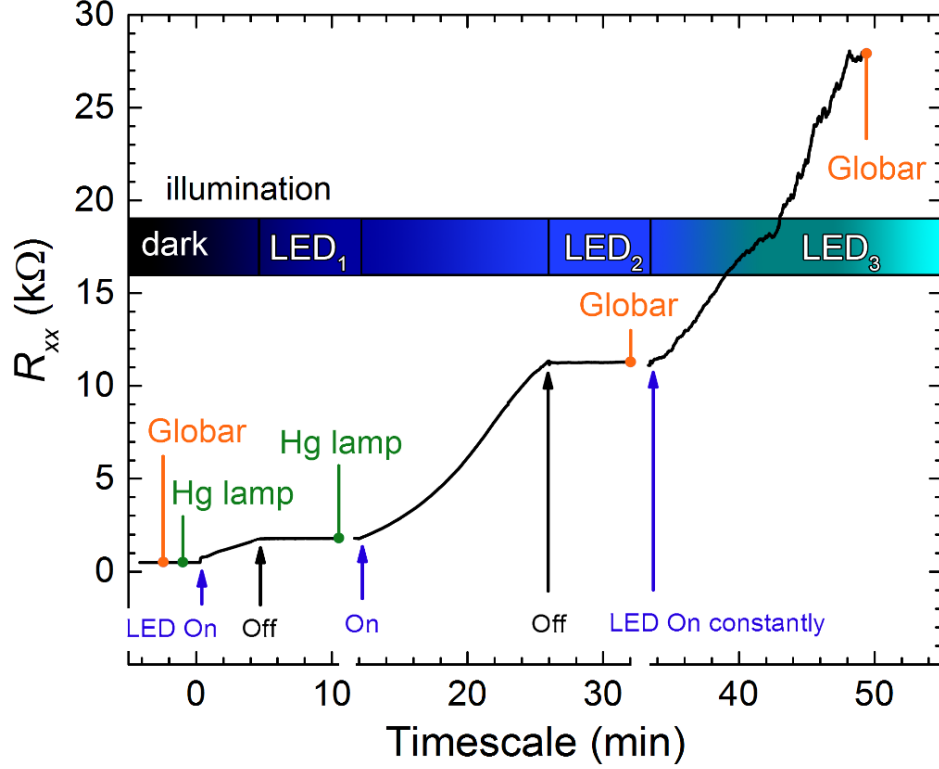


Fig. 12. A characteristic dependence of zero-field longitudinal resistance R_{xx} (sample B) during three illumination steps by a blue LED. The vertical arrows indicate times when the LED diode was switch on or off. The vertical lines show times when the magneto-optical measurements with an indicated source were carried out. The middle infrared part of the radiation was blocked using the black PE entrance window.

3.2 Hamiltonian and eigenstates for system with reduced symmetry

The Landau level spectrum was calculated by the diagonalization of the 8×8 $\mathbf{k} \cdot \mathbf{p}$ Hamiltonian for (013)-oriented heterostructures, thus considering states with the symmetries Γ_6 , Γ_8 and Γ_7 bands [23, 27, 28]. A tensile strain in individual layers arising due to the mismatch of lattice constants in the CdTe buffer, HgTe QW, and $\text{Cd}_x\text{Hg}_{1-x}\text{Te}$ barriers were also included, with material parameters taken from Ref. [61]. This model allows us to describe the non-parabolic profiles of bands as well as effects of the spin-orbit interaction. The electron and hole states were calculated in two subsequent stages. To this end, the Hamiltonian was represented as a sum of the axial and anisotropic parts:

$$H = H_s + H_a, \quad (\text{Eq. 2})$$

where H_s is invariant with respect to rotations along the growth axis. In the first stage, the eigenstates of H_s were found [23, 27, 28]. These eigenstates then served in the second stage as a basis for the expansion of eigenstates of the full Hamiltonian H :

$$\psi = \sum_{n,m} c_{n,m} \psi_{n,m} \quad (\text{Eq. 3})$$

The corresponding coefficients $c_{n,m}$ were then found using a numerical diagonalization of H . Here the LL index is denoted by n and the integer m labels individual subbands. In our calculations, two conduction and eleven valence subbands were taken into account. For each subband, we considered 14 Landau levels ($n = -2, -1, 0, 1 \dots 11$). We performed additional calculations with additional subbands and extra LLs considered. Obtained results did not provide us with any significant corrections to the eigenenergies for $B > 2$ T. At lower fields, the

number of LLs taken into account should be increased to achieve a quantitatively correct description of valence states. In particular, this becomes important for HgTe QWs with an inverted band structure (*i.e.*, for widths $d > d_c$) with the maxima of valence subbands typically located at $k \neq 0$.

The anisotropic part of the total Hamiltonian H_a includes terms describing the cubic symmetry, the lack of the inversion symmetry in the bulk crystal and the symmetry lowering at the heterointerfaces (BIA and IIA). The explicit form of the Hamiltonian in the absence of the magnetic field for the case $z \parallel [013]$ is given in Ref. [23]. The magnetic field has been introduced using the standard Peierls substitution. The BIA term was derived from 14×14 Kane Hamiltonian proposed in Ref. [69], from which also the corresponding parameters were taken (same for CdTe and HgTe). The IIA terms for the (013)-oriented QWs are expressed in Ref. [71] (see Eqs. 5 and 6 therein). The parameter g_4 (solely determining the power of the effect) was taken as $1.4 \text{ eV} \times \text{\AA}$ in our advanced Kane model. The chosen value reproduces exactly the spin splitting the Dirac cone in the (001)-oriented HgTe QW with the critical thickness $d_c = 6.3 \text{ nm}$ at zero momentum, calculated using the tight-binding approximation in Ref. [70]. Notably, for this symmetric crystallographic orientation, the BIA term practically does not contribute to this splitting, which is thus primarily driven by IIA (see, *e.g.*, [64]). The structural inversion asymmetry (SIA) is negligible for our samples, since it requires an electric field in the direction perpendicular to plane of QW, which usually induced by asymmetric doping in barriers or by means of the gate voltage, not applied in our case.

3.3 Matrix elements for optical transitions between Landau levels

The matrix elements for optical transitions between Landau levels were calculated for non-polarized radiation used in our magneto-optical experiments. The probability of such a transition is proportional to the square of the dipole moment matrix element (product of the electron charge and the matrix element of the coordinate operator). The matrix element $r_{f,i}$ of the coordinate operator between the initial $|i\rangle$ and final $|f\rangle$ states satisfies the equation:

$$\mathbf{v}_{f,i} = \frac{i}{\hbar} [H, \mathbf{r}]_{f,i} = \frac{i}{\hbar} (\varepsilon_f - \varepsilon_i) \mathbf{r}_{f,i}, \quad (\text{Eq. 4})$$

where \mathbf{v} is the velocity operator. First, one has to find the velocity operator using Eq. 1, and then, to calculate the matrix elements. The BIA term has thus been omitted in these expressions since it represents only a second-order correction. As for IIA, the corresponding term commutes with the coordination operator, thus giving zero correction to the mean value of the velocity operator.

In the axial model, the selection rules for electric-dipole excitations are $\Delta n = \pm 1$ and no spin-flip excitations are allowed. The applicability of these ‘‘axial’’ selection rules for HgTe/CdHgTe QWs was demonstrated in a number of works [23, 26-29, 63]. It is worth mentioning that the interpretation of (cyclotron resonance-like) excitations within the conduction band is simpler due to a rather large spacing of LLs. In contrast, the identification of particular CR excitations in *p*-type samples is more challenging. The relatively flat valence bands imply a relatively high density of states, and when the magnetic field is applied, a corresponding densely spaced set of Landau levels, some of which contribute a complex set of excitations to the observed spectrum. To facilitate the identification of individual lines, we calculated the corresponding matrix elements for electric-dipole transitions between different pairs of LLs in order to compare the relative strength of excitations.

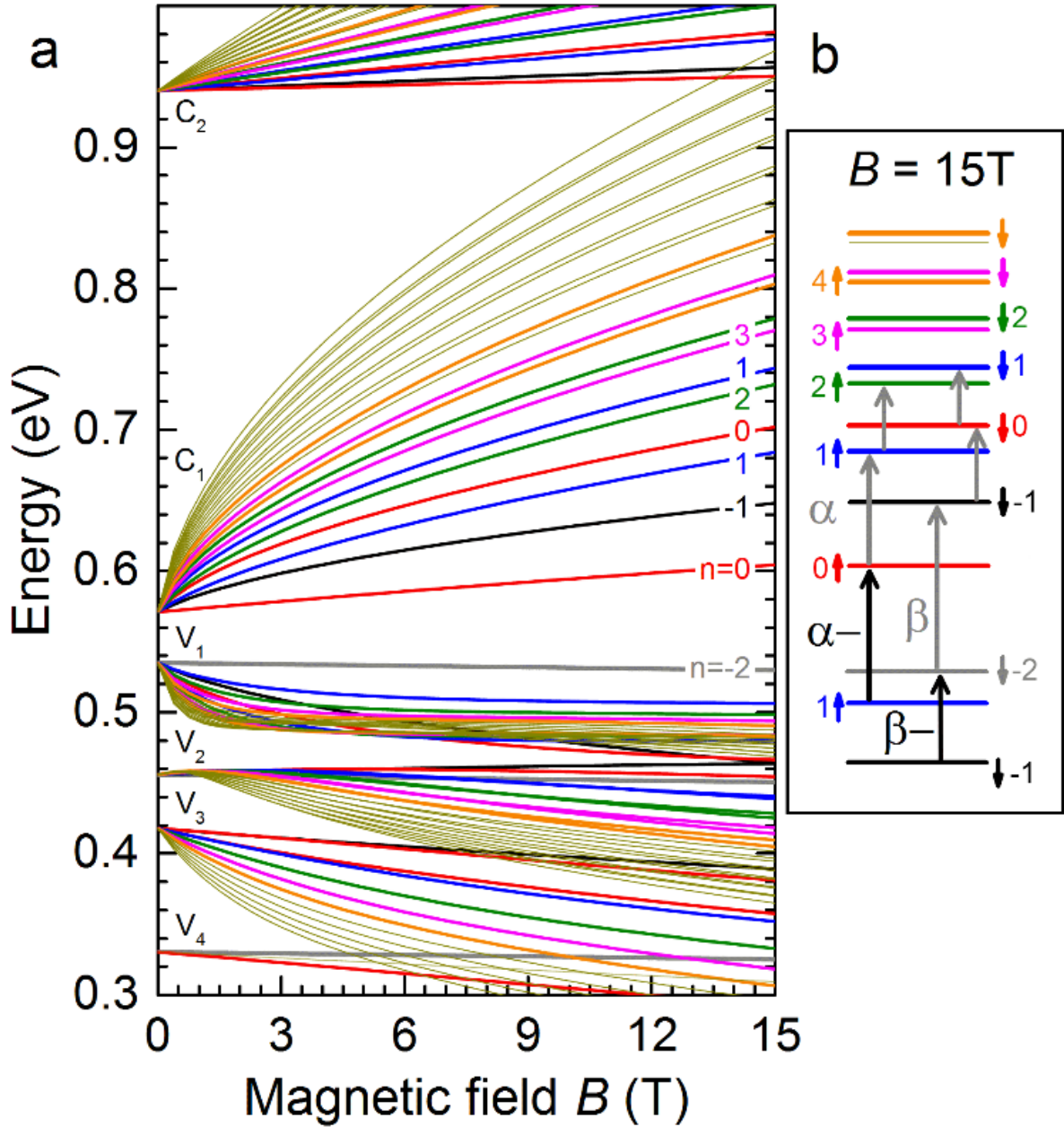


Fig. 13. (a) Landau levels in sample B calculated in the axial approximation taking account of two conduction (C_1 , C_2) and four valence ($V_1 - V_4$) subbands. (b) Landau level energies at $B = 15$ T. The short arrows near the LL indices mark the dominant spin projection. The long vertical arrows indicate the allowed electric-dipole-active excitations between different pairs of LLs. The detailed description is available in Table II. The transition α ($0_{\uparrow} \rightarrow 1_{\uparrow}$) are typical for the n -type samples, while α^- ($1_{\uparrow} \rightarrow 0_{\uparrow}$), β ($-2_{\downarrow} \rightarrow -1_{\downarrow}$) and β^- ($-1_{\downarrow} \rightarrow -2_{\downarrow}$) are characteristic for the p -type specimens.

We have considered optical transitions among thirty different Landau levels: four low-energy LLs in C_1 subband, eleven top LLs both in V_1 and V_2 subbands ($n = -2, -1, 0, \dots, 4$) and four LLs in V_3 subband ($n = -1, 0$), see Fig. 13. The excitations from/to LLs in other, more distant subbands were not included since they do not fit into the spectral window explored in our experiments. The transitions originally “forbidden” in the axial model may become active due to mixing neighboring Landau levels induced by BIA or IIA effects. Since these symmetry-lowering effects profoundly modify the profiles of valence subbands, one may expect that they primarily influence excitations involving LLs originating from those valence subbands.

Table II. The square of matrix elements of transitions between Landau levels optically active in the axial approximation. The results are given for the lowest conduction subband (C_1) and for the highest valence (V_1) subband at 6 T for the normal (sample B) and inverted (sample E) band structure.

Landau level		Transition label	Δn	$ r_{fi} ^2$ (\AA^2)		
initial	final			Sample B	Sample E	
C_1	0_\downarrow	1_\downarrow	ε	1	10385	11082
	1_\uparrow	2_\uparrow	δ	1	8287	7720
	-1_\downarrow	0_\downarrow	γ	1	5724	6665
	0_\uparrow	1_\uparrow	α	1	3766	3184
V_1	-1_\downarrow	-2_\downarrow	β^-	-1	2945	1653
	0_\downarrow	-1_\downarrow	γ^-	-1	5722	5670
	2_\uparrow	1_\uparrow	δ^-	-1	5388	1319
	3_\uparrow	2_\uparrow		-1	8476	8337
V_1	-2_\downarrow	-1_\downarrow	β	1	1366	2576
	1_\uparrow	0_\uparrow	α^-	-1	1109	2566
	2_\uparrow	1_\uparrow		-1	247	200
	0_\downarrow	-1_\downarrow		-1	219	530
	-1_\downarrow	0_\downarrow		1	186	42

Before we start a thorough analysis of our experimental data, let us summarize the main trends/findings from the theoretical consideration and calculations. In Table II, we show the squares of matrix elements of the coordinate operator calculated at $B = 6$ T for QWs with normal and inverted band ordering. Obtained values allow us to estimate the relative intensities of individual absorption lines. In addition, we also provide the square of the coordinate matrix elements for β , β^- and α^- lines for the selected values of B (see Table III). This latter Table shows that theoretically, no significant changes in relative intensities are expected with the magnetic field apart from those related to the occupation of LLs. Let us also note that the squared coordinate matrix element has to be multiplied by the LL degeneracy (linear in B), the difference between the initial and final filling factors and the transition energy to get the integral intensity of any absorption line (see equations 48-51 in [144]).

Table III. The calculated squares of matrix elements $|r_{fi}|^2$ for dominant optical transitions in sample B for the selected values of the magnetic field (in units of \AA^2).

B (T)	1	2	3	4	5	6	7	8	9	10
β^-	21981	10127	6418	4644	3614	2945	2478	2133	1869	1660
β	4276	2964	2284	1863	1576	1366	1207	1081	979	894
α^-	3818	2534	1907	1533	1286	1109	977	875	793	727

One may immediately see in Table II that the strength of intraband (cyclotron resonance-like) transitions ($C_1 \rightarrow C_1$ and $V_1 \rightarrow V_1$) exceeds that of interband transitions ($V_1 \rightarrow C_1$). Besides, the energies of the intraband transitions are less sensitive, as compared to the interband excitations, to the QW width and to fluctuations of E_g resulting from the lateral inhomogeneity of heterostructures. This implies that the dominant contribution to the magneto-optical response should stem from intraband excitations, which should also give rise to narrower spectral lines.

Let us also note that electric-dipole transitions within the given electron or hole subband (within $C_{1,2}$ or within $V_{1,2}$) always follow the selection rules $\Delta n = 1$ and -1 , respectively. Such transitions represent pure cyclotron resonance modes and these selection rules reflect the opposite sense of the cyclotron motion of electrons and holes, and consequently, also the

opposite circular polarization of absorbed radiation. In the inter(sub)band response, excitations may be active in both circular polarizations: $\Delta n = \pm 1$. For example, transitions to LL $n = -1_i$ in the C_1 subband are allowed from both the top LL $n = -2_i$ in the V_1 subband and from deeper LL $n = 0_i$ (see Table II). In the latter case, the squared matrix element $|r_{f,i}|^2$ is significantly weaker due to bigger energy difference ($\varepsilon_f - \varepsilon_i$) for the given transition (see Eq. 3).

3.4 Dominant and high energy optical transitions in axial model

We will now proceed with the interpretation of our experimental data in two subsequent steps. In the first one, we analyze the data using the axial model, thus identifying the limits of such an approach. In the second step, we compare experiments with a more sophisticated model, which includes both above-mentioned mechanisms of symmetry lowering.

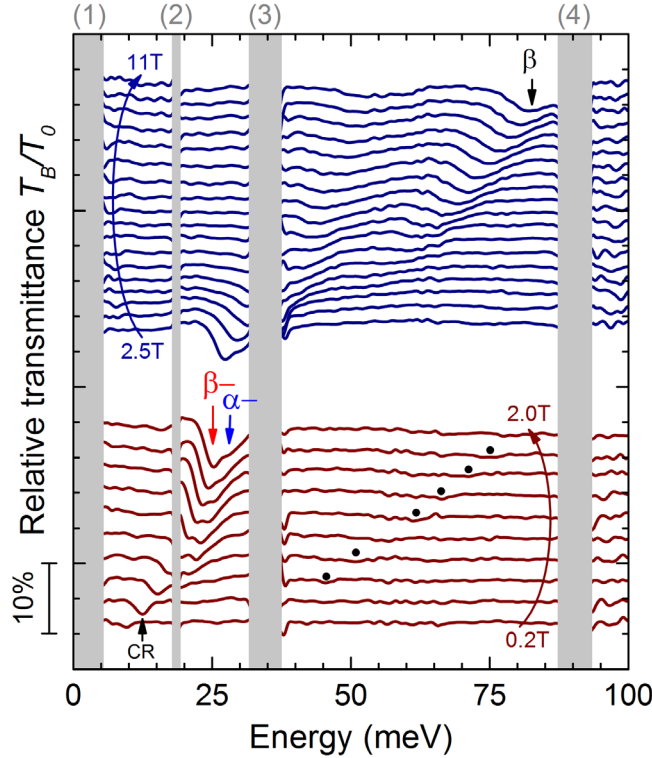


Fig. 14. The low-temperature magneto-transmission spectra collected on sample D. The Hg lamp was used as the source of the radiation for the spectra measured at the fields below 2 T (with the step of 0.2 T). At higher fields, the globar was employed and the step was increased to 0.5 T. Dominant optical transitions are denoted by vertical arrows and labeled according to Table II. The relatively broad spectral feature marked by black dots correspond to a series of excitations analogous to η lines observed and analyzed in detail for sample B (cf. Fig. 20 and Table IV). The grey areas correspond to the spectral regions fully opaque due to the reststrahlen band of HgCdTe and GaAs (2 and 3, respectively) and absorption in the multilayer beamsplitter (4). At low energies (1), it is the low intensity of the radiation source and the low efficiency of the used beamsplitter, which did not allow us to collect the data with a sufficiently high signal-to-noise ratio.

The magneto-transmission spectra recorded on sample D are plotted in Fig. 14. The “dark” hole concentration in this sample was $3.2 \times 10^{10} \text{ cm}^{-2}$, so the filling factor $\nu \approx 1$ is reached at $B = 1.3 \text{ T}$. LLs calculated in the axial approximation are plotted in Fig. 15, where the dotted line indicates the expected position of the Fermi energy as a function of B . The transition, which gradually emerges in the high-field spectra, may be identified as the β line, see Fig. 15. It corresponds to the excitation of electrons from the topmost (partially populated) valence LL

$n = -2_{\downarrow}$, to $n = -1_{\downarrow}$ level in the C_1 conduction subband. This transition is characteristic of all p -doped HgTe/CdHgTe QWs and has already been identified in the early work dedicated to the magneto-optical properties of these systems [26]. The response at low energies and low magnetic fields is dominated by $\alpha-$ and $\beta-$ transitions. The former line is, in this case, the lowest-in-energy interband excitation, from $n = 1_{\uparrow}$ LL to the zero-mode $n = 0_{\uparrow}$ level. This line is analogous to the α line in the conduction band of QWs with an inverted band structure [23, 27-29, 63, 65, 68]. The $\beta-$ line represents a purely CR mode, $-1_{\downarrow} \rightarrow -2_{\downarrow}$, and may thus be expected in all p -doped samples (for a particular hole concentration).

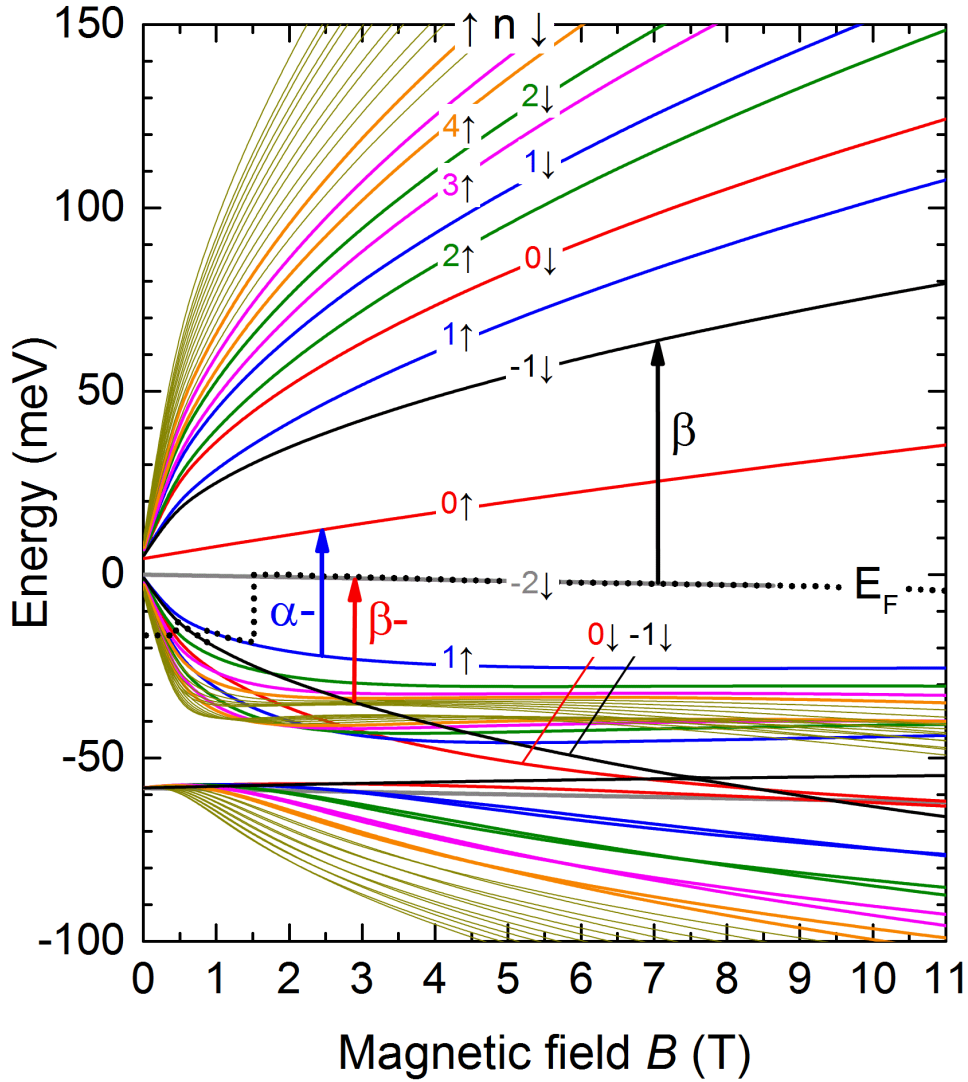


Fig. 15. LLs calculated for sample D within the axial model. Dominant electric-dipole transitions are denoted by vertical arrows.

The β , $\alpha-$ and $\beta-$ lines dominate the magneto-optical response of all investigated samples (Fig. 17). In the case of a normal band structure, transitions $\alpha-$ and β have an interband character and may be always observed in magnetic fields high enough, when the quantum limit of our (weakly p -doped) samples is approached. The zero-field extrapolation of their positions provides us with a good estimate of the bandgap. In agreement with theoretical expectations, the band gap E_g indeed decreases with the thickness of QWs with the normal band ordering as shown in Fig. 17 (a-d). In contrast to these interband excitations, the $\beta-$ line has a purely

intraband (CR-like) character, with the strength proportional to the total carrier (hole) density in the explored QWs.

Moreover, the activity of interband transitions in circularly polarized radiation has been crosschecked by Faraday rotation measurements (see. Fig. 16), where for α^- transition we observe negative slope, corresponding to $\Delta n = -1$, while for β with $\Delta n = +1$ we have opposite slope.

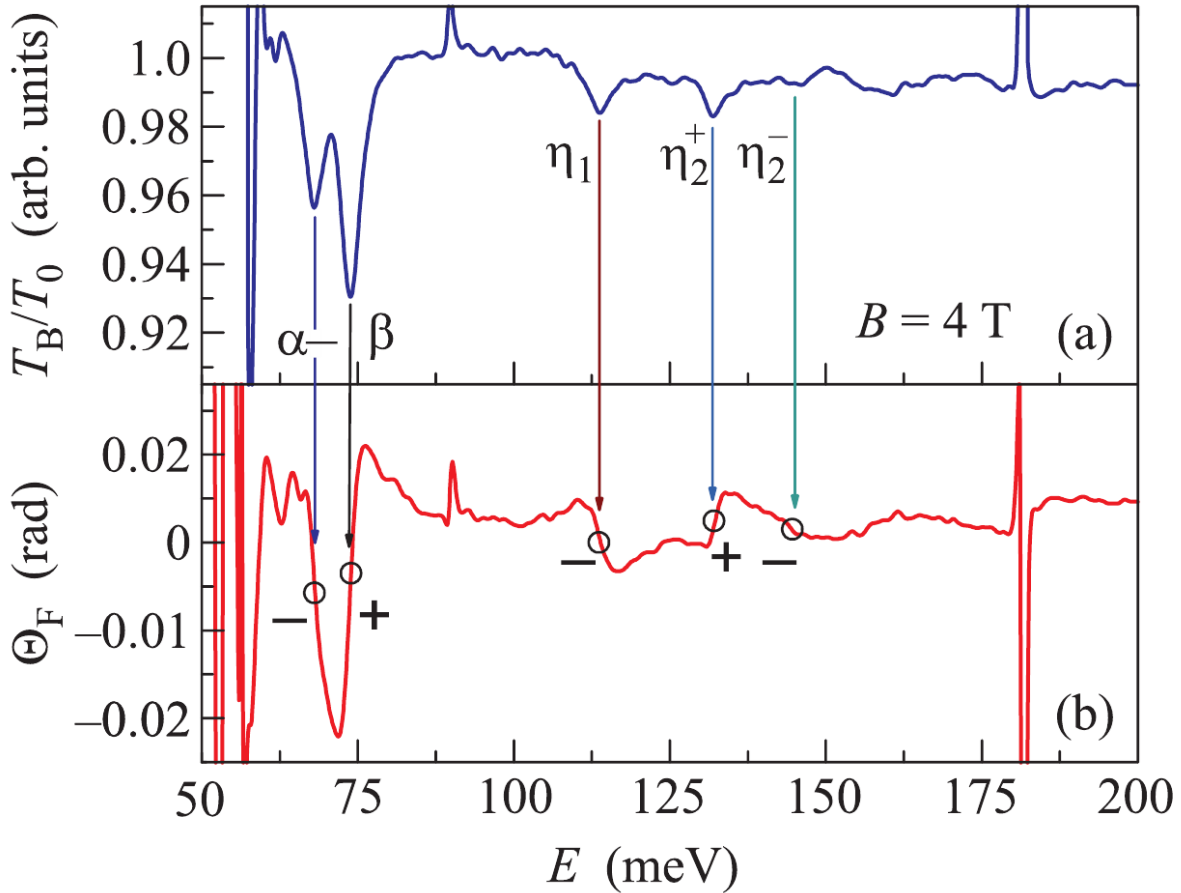


Fig. 16. Transmittance (a) and Faraday rotation (b) spectra in sample B for a fixed $B = 4 \text{ T}$. For each feature in spectrum (a) there is a characteristic sign of the slope in spectrum (b) corresponding to transition type: electron-like ($-$) or hole-like ($+$).

The correct assignment of the dominant absorption lines may be independently checked in the spectra recorded under illumination using the blue diode (due to PPC effect), which gradually lowers the total hole density. The relative magneto-transmission spectra plotted in Fig. 18 show the evolution of the response after several illumination steps. One may immediately notice that the β^- line gradually disappears from the spectrum under illumination, following thus the decreasing hole density. The interband excitations α^- and β show distinctively different behavior. The intensity of α^- transition remains constant with the illumination and the strength of the β transition even increases.

The observed variation of intensities with the illumination may be explained when the specific $n = -2_{\downarrow}$ zero-mode LL is considered, see Fig. 15. This level represents the final and initial states for β^{-} and β excitations, respectively, but at the same time, it is not involved in α^{-} transition. In the quantum limit, when the only $n = -2_{\downarrow}$ level is occupied by holes (*e.g.*, at $B = 8$ T for sample C, see Fig. 18), the illumination by the blue LED decreases this occupation, or equivalently, it increases the number of electrons in this level. This directly implies a gradual increase and decrease of the absorption strengths for the β and β^{-} excitations, respectively. In turn, α^{-} transition, with the initial and final states in the $n = 1_{\uparrow}$ and $n = 0_{\uparrow}$ LLs of the V_1 and C_1 subbands, respectively, remains unaffected.

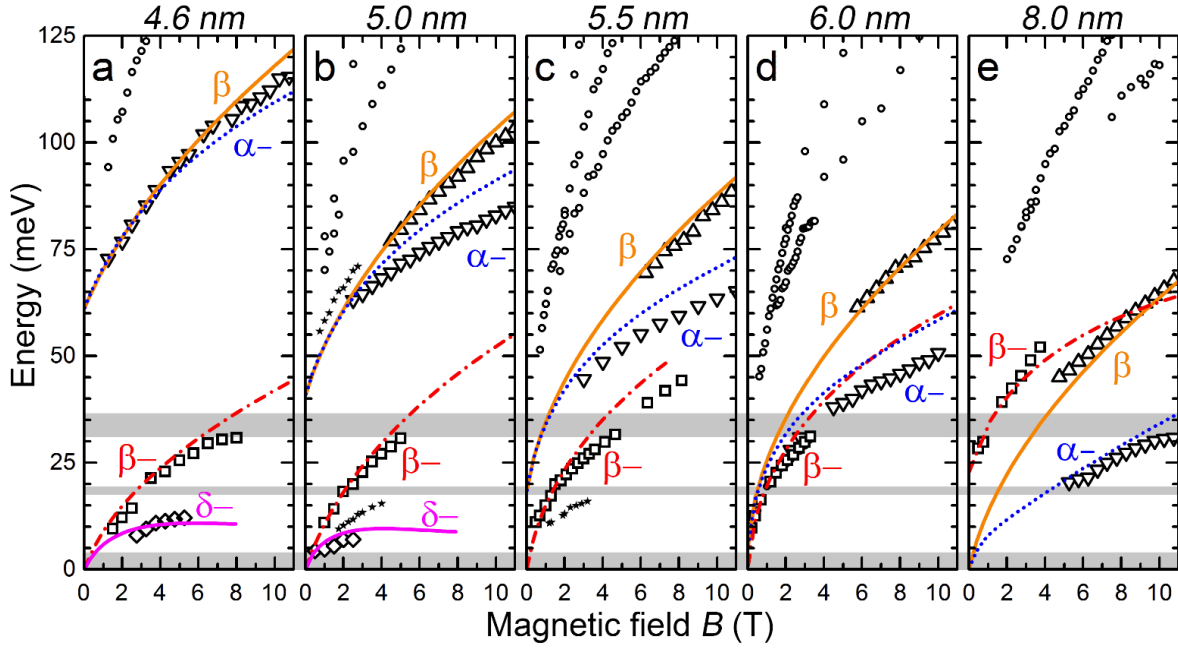


Fig. 17. The energies of α (blue dotted), β (orange solid), β^{-} (red dash-dot) and δ^{-} (magenta solid) transitions as a function of the applied magnetic field in the HgTe/CdHgTe QWs with the normal a) $p_s = 9.0 \times 10^{10} \text{ cm}^{-2}$, b) $p_s = 7.4 \times 10^{10} \text{ cm}^{-2}$, c) $p_s = 6.6 \times 10^{10} \text{ cm}^{-2}$, d) $p_s = 3.2 \times 10^{10} \text{ cm}^{-2}$, and inverted e) $p_s = 1.1 \times 10^{11} \text{ cm}^{-2}$ band structure (d_{qw} is shown on top of each graph). The experimental data are represented by symbols: down triangles, up triangles, squares and diamonds for α^{-} , β , β^{-} , δ^{-} transitions, respectively. The open circles represent the high-energy transitions discussed below. The stars correspond to additional transitions, which emerge due to the reduced symmetry (discussed later on as well).

The above-discussed interplay between intensities of β^{-} and β lines can be traced in a wide range of magnetic fields. At a higher hole concentration, see Fig. 19 (a), the β^{-} line is observed up to 11 T, while the β line only appears at magnetic fields above 6 T, reflecting thus the gradually increasing number of electrons in $n = -2_{\downarrow}$ LL. After illumination, *i.e.*, with the hole density lowered, the β line emerges in the spectrum at magnetic fields as low as $B \approx 3$ T.

To complete our discussion, let us note that the intensity of the β^{-} line decreases significantly above 6 T. As a matter of fact, this line represents – in magnetic fields high enough and in samples with a non-inverted band structure – the cyclotron resonance absorption in the quantum limit (when only the highest hole LL is occupied). In such a case, the intensity of the line is proportional to the hole density (constant with B in the first approach), to the square of the coordinate matrix element (expected to roughly follow the $1/B$ dependence) and to the transition energy (increasing sub-linearly with B). This indeed implies a decrease in the integral strength of the β^{-} line. In numbers, see Table III and Fig. 19 (b): the increase of the transition energy of 30, 43 and 54 meV at $B = 3, 6$ and 9 T does not compensate the decrease in the square of the

coordinate matrix $|r_{\Gamma,i}|^2 \approx 6400, 3000$ and 1900 (\AA^2), respectively. Nevertheless, this decrease is relatively weak and does not explain our experimental observation.

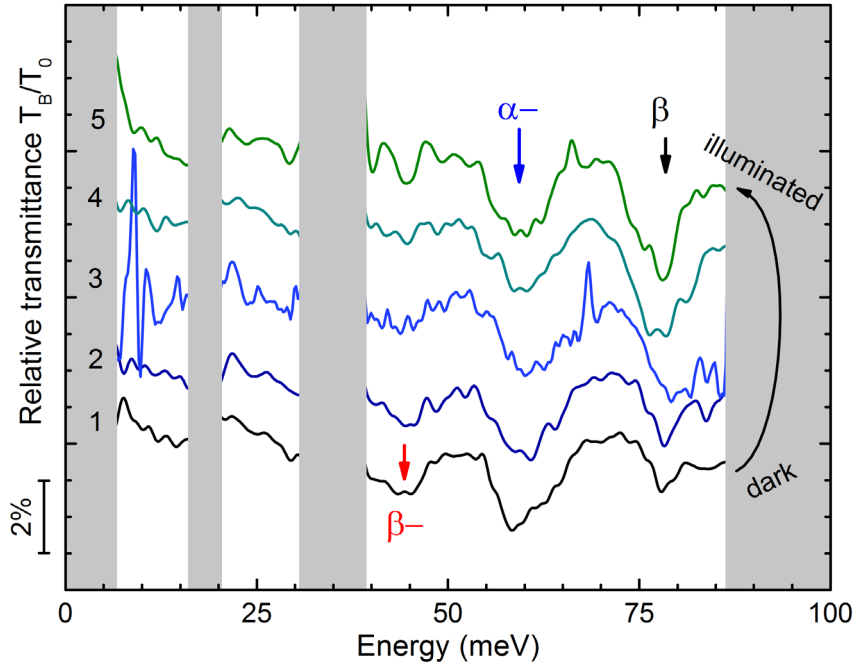


Fig. 18. The relative magneto-transmission spectra taken at $B = 8$ T on sample C, for various hole concentrations from p_{\max} (1) to p_{\min} (5) induced using the PPC effect by illumination. The spectra are shifted vertically by 2% for clarity.

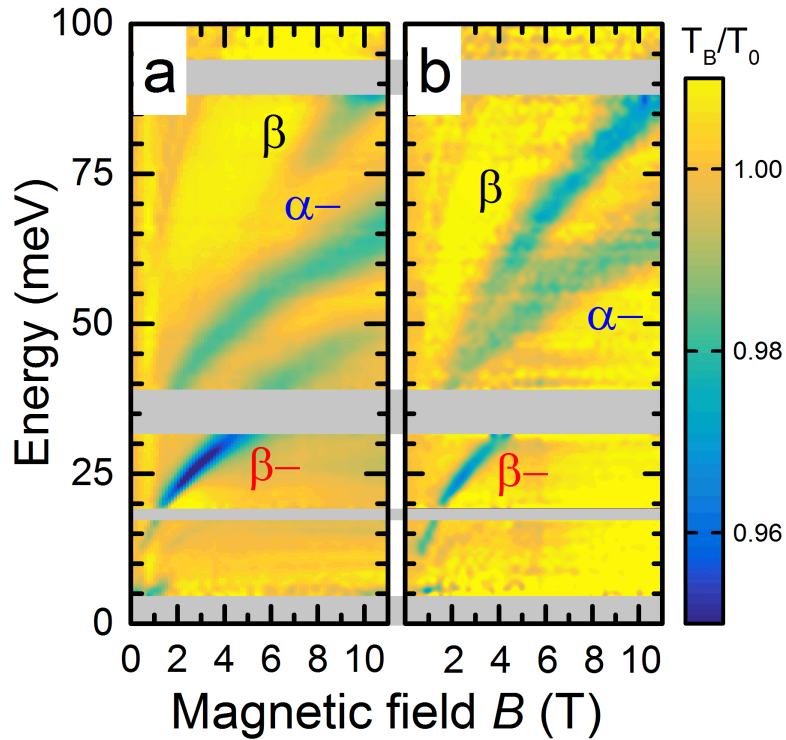


Fig. 19. Magneto-transmission of sample C for two hole concentrations: p_{\max} (a) and p_{\min} (b), plotted as a false color-map. The dominant excitations are labeled by $\beta-$, $\alpha-$ and β .

The disappearance of the β^- line in high magnetic fields may be related to some localization effect which removes holes from the $n = -2_{\downarrow}$ LL. Significant broadening of the β^- line, due to a particular scattering mechanism (*e.g.*, the $B^{1/2}$ dependence of the line width is expected in the standard CR theory for both short and long-range scattering [56, 141, 151]) and/or due to the strong mixing of the initial LL with other levels in the valence band, may also contribute to the effective disappearance of the β^- line from spectra. Anyway, the decrease of the β^- line strength was observed for all QWs [Fig. 17 (a-d)]. In contrast, the intensity of the β line seems to be increasing in its strength at the expense of the β^- line in the investigated samples.

The deeper analysis of the transmission spectra of sample B at higher photon energies ($\hbar\omega > 100$ meV) reveals the presence of more than five additional transitions, which correspond to excitations between LLs in V_1 and C_1 subbands and of two pronounced excitations, which are identified as transitions between pairs of LLs in the V_3 and C_1 subbands (see Fig. 20). The zero-field extrapolation of the line energies yields the separation of subbands of about 40 meV and 160 meV, respectively, which is in good agreement with the calculations performed within the axial model. As for transitions from V_2 to C_1 subbands, they are supposed to be relatively weak due to opposite parity of corresponding wave functions (strictly speaking valid for $k = 0$ parity only). A weak absorption line may be traced in the spectra at magnetic fields high enough (above 5 T) in Fig. 20 (c). This can be associated with the α^+ transition, see Table IV.

Table IV. Squared matrix elements of allowed optical transitions between Landau levels for subbands V_1 , V_3 and C_1 in the axial approximation at a magnetic induction of 6 T for sample B.

Landau level		Transition label	Δn	$ r_{f,i} ^2$ (\AA^2)	$\Sigma r_{f,i} ^2$		
initial	final						
V_1	2_{\uparrow}	C_1	1_{\uparrow}	η_1	-1	493	930
	0_{\downarrow}		-1_{\downarrow}			-1	
V_1	-1_{\downarrow}	C_1	0_{\downarrow}	η_2	-1	372	
	1_{\uparrow}		0_{\uparrow}			341	
	3_{\uparrow}		2_{\uparrow}			263	
	1_{\uparrow}		2_{\uparrow}			265	
V_1	2_{\downarrow}	C_1	1_{\downarrow}	η_3	1	258	
	0_{\downarrow}		1_{\downarrow}			202	
	2_{\uparrow}		3_{\uparrow}			227	
	4_{\uparrow}		3_{\uparrow}			92	
V_1	3_{\downarrow}	C_1	2_{\downarrow}	η_4	-1	213	
	3_{\uparrow}		4_{\uparrow}			75	
	1_{\downarrow}		2_{\downarrow}			129	
V_1	4_{\downarrow}	C_1	3_{\downarrow}	η_5	1	77	
	4_{\uparrow}		5_{\uparrow}			67	
	2_{\downarrow}		3_{\downarrow}			55	
V_2	-1_{\uparrow}	C_1	0_{\uparrow}	α^+	-1	368	-
V_3	-1_{\uparrow}	C_1	0_{\uparrow}	τ_1	1	343	-
V_3	0_{\downarrow}	C_1	-1_{\downarrow}	τ_2	-1	128	-

The relative intensities of high-energy absorption lines do not exceed 2%. The signal-to-noise ratio in our experimental data allowed us to reveal absorption lines with relative intensities down to 0.5%. It is important to note that our calculations predict low intensities for these high-energy transitions, with the squared matrix elements reduced by almost two orders of magnitude as compared to dominant transitions (*cf.* data in Table II & Table IV). Nevertheless, these transitions are still visible in the spectra, since they are rather closely spaced, and in fact,

strongly overlapping in our experiments (taking account of the experimentally observed line widths). For example, the observed line η_1 in see Fig. 20(c) results from two different transitions with nearly identical energies as shown in see Fig. 20(e).

As for the interband transitions from the V_3 subband, we attribute the lower line τ_1 to the transition $-1_\uparrow \rightarrow 0_\uparrow$, and τ_2 to the transition $0_\downarrow \rightarrow -1_\downarrow$. In this case, let us note that the energies of initial-state LLs in the V_3 subband depend on the magnetic field only very weakly, in contrast to the final-state LLs in the conduction band. This way, the field-dependence and separation of LLs in the C_1 conduction band are thus straightforwardly visualized. This gives us a possibility to study conduction-band LLs even in p -type samples, which is an alternative approach to the standard cyclotron resonance technique applied to n -doped QWs [23, 25, 27-29, 53, 65, 68].

Let us conclude this subsection by the observation that the band structure model preserving axial symmetry provides us with an overall acceptable, but as discussed later on not with a complete quantitative description of interband excitations between LLs in different valence and conduction subbands. In the following part, we will specifically focus on limits of the axial model.

3.5 Effects of symmetry lowering in low-fields and avoided crossings

In the previous part, we have shown that the axial model is capable of explaining the dominant features in the magneto-absorption spectra of HgTe/CdHgTe QWs. In what follows, we will concentrate on the findings that cannot be explained within the axial approximation.

Let us start with the magneto-optical response at relatively low energies, which is dominated by cyclotron resonance of hole. According to the calculations performed within the axial 4-band Kane model, such a response should be at low hole densities (for the filling factor $\nu < 2$) dominated by two CR modes, by the β^- and δ^- lines. These transitions are electric-dipole-allowed within the axial model and correspond to inter-LL excitations, $-1_\downarrow \rightarrow -2_\downarrow$ and $2_\uparrow \rightarrow 1_\uparrow$, respectively [see Fig. 20 (d,e)]. Indeed, both these modes are clearly resolved in our experimental data, with the relative intensity depending on the applied magnetic field and particular hole density [Fig. 18(a,b) and Fig. 20 (a,b,c)].

A closer inspection of the data, however, reveals another CR mode denoted β^* in Fig. 20(a, b, c), located in between the β^- and δ^- lines and characterized by roughly half the intensity. This line is observed in the response of several samples with a normal ordering of bands, and it is best manifested for sample B, which shows the highest mobility from the series of explored samples. Importantly, this line cannot be, having in mind the occupation of valence band LLs with relatively low-indices, explained within the axial 4-band Kane model. At the same time, its spectral position fairly well matches the transition $1_\uparrow \rightarrow -2_\downarrow$, see Fig. 20 (d), which is strictly forbidden within the axial model.

The situation changes when symmetry lowering effects are included in the corresponding Hamiltonian. The resulting band structure then loses its axial symmetry. Among other effects, the original selection rules $\Delta n = \pm 1$ is broken for inter-LL excitations and the magneto-optical response may become significantly richer concerning the number of electric-dipole active transitions. Alternatively, the impact of symmetry lowering effects may be also understood in terms of mixing of the original (in the axial model calculated) Landau levels. This mixing becomes in particular important in valence subbands with rather a narrow spacing of Landau levels.

To illustrate this, we have estimated intensities of CR-like excitations, with their final state in the highest valence Landau level ($n = -2_\downarrow$ in the axial model) from several subjacent LLs, denoted as $v_1 \dots v_6$ in Fig. 21. Due to the LL mixing induced by the symmetry lowering effects, the strength of the $-1_\downarrow \rightarrow -2_\downarrow$ excitation, which is the only one allowed within the axial model, is now distributed among a series of excitations from different initial LLs to $n = -2_\downarrow$ level. The relative strength of these excitations strongly varies with B . Importantly, the transition $1_\uparrow \rightarrow -2_\downarrow$, originally forbidden in the electric-dipole approximation [line 1 in Fig. 21], becomes active

in a rather broad range of fields, with the transition probability smaller but still comparable to the strength of the $-1_{\downarrow} \rightarrow -2_{\downarrow}$ excitation (e.g., equal to 1/3 at 2 T). We may also notice that the maximum of the oscillator strength always corresponds to the excitation with the initial state that is closest to the $n = -1_{\downarrow}$ LL. With increasing B , the spacing of LLs increases as well and the overall response approaches the one expected in the axial model, in which the $\beta-$ line dominates the low energies.

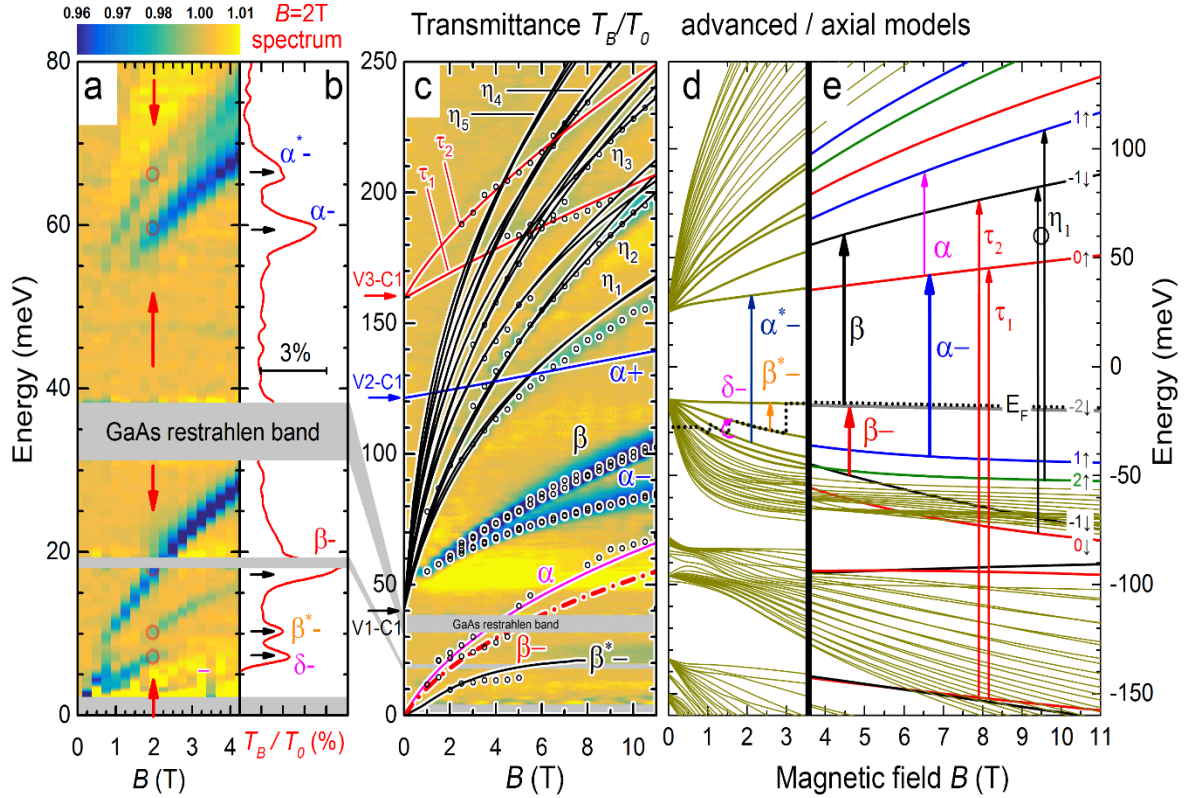


Fig. 20. Magneto-transmission of sample B plotted in the form false-color plots for the maximal (a) and minimal (c) hole concentrations. The red vertical arrows and circles in (a) show the transitions clearly resolved and denoted by Greek letters in the magneto-transmission spectrum taken at $B = 2$ T and plotted in (b). The solid lines in (c) correspond to the theoretically expected energies of the transitions β^* -, β -, α -, $\alpha+$ -, τ_1 , τ_2 and absorption lines η_1 , η_2 , η_3 , η_4 , see the main text. The black open circles stand for the observed transmission minima. (d, e) The LL fan charts calculated in the axial (e) model for $B > 3.5$ T, where all indicated transitions follow the standard selection rules $n \rightarrow n \pm 1$ and the advanced model (d) for $B < 3.5$ T, where LLs are mixed due to symmetry lowering effects, giving rise to additional transitions in the electric-dipole approximation. The dotted line indicates the Fermi level position of the “dark” state (the maximal hole density). The arrows and Greek letters denote LL transitions, observed in the magneto-transmission spectra, the absorption line η_1 contains two close in energy transitions $0_{\downarrow} \rightarrow -1_{\downarrow}$ and $2_{\uparrow} \rightarrow 1_{\uparrow}$, merged in (e) with a black circle.

The appearance of the weak α^* -line in the magneto-absorption spectrum serves as another experimental evidence for symmetry lowering effects [Fig. 20(a, b, d)]. The position of this line matches well the spin-flip transition $-1_{\downarrow} \rightarrow 0_{\uparrow}$, which is strictly electric-dipole forbidden in the axial approximation. Again, its presence may be explained by LL mixing due to symmetry lowering effects. In this case, it is the mixing of $n = 1_{\uparrow}$ and $n = -1_{\downarrow}$ levels, which makes this excitation electric-dipole active. This line may be viewed as a satellite transition of $\alpha-$ line. Notably, α^* -line gradually disappears from the spectra with the increasing magnetic field

(completely above 4 T), when the spacing of $n = 1_{\uparrow}$ and $n = -1_{\downarrow}$ levels increases and the mixing weakens. Let us also note that the α^* -line is also present in the response at low hole concentrations. Nevertheless, it is not directly visible in the false-color plot in Fig. 20(c). This is due to a pronounced high-energy tail of the β line, the intensity of which is greatly enhanced as compared to Fig. 20(a, b) because of the increased population of LL $n = -2_{\downarrow}$ (by electrons).

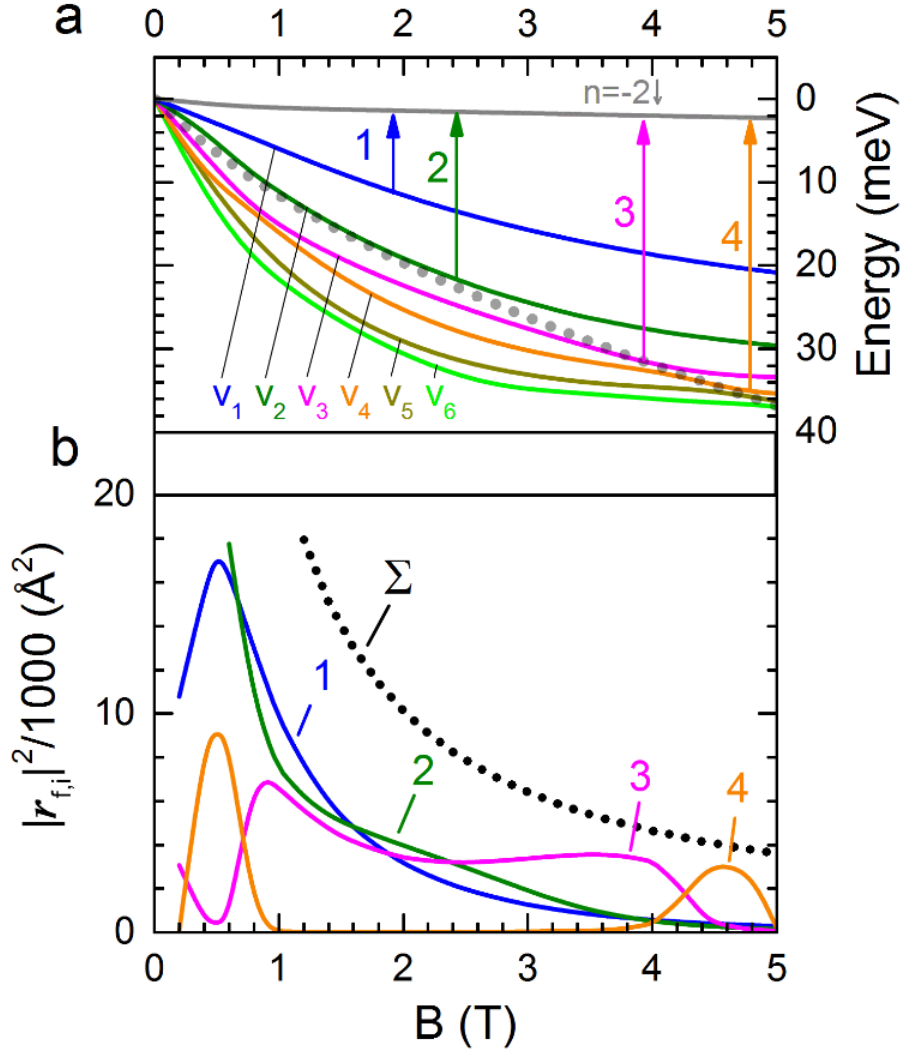


Fig. 21. (a) The Landau level spectrum for sample B calculated in the advanced model taking account of the symmetry lowering effects. The “axial” level -1_{\downarrow} is depicted with the dotted line. The arrows represent transitions discussed in the text. (b) The squared matrix elements plotted as a function of B for transitions with initial states in the “mixed” LLs v_1 - v_6 to the top valence band LL $n = -2_{\downarrow}$, shown in Fig. 21(a). The dotted line Σ stands for the “axial” matrix element $|r_{fi}|^2$ of the β^- transition.

The symmetry lowering effects are also clearly manifested by an avoided crossing of so-called zero-more LLs: $n = -2_{\downarrow}$ and $n = 0_{\uparrow}$. Nevertheless, their impact on the magneto-optical response has been so far studied only in n -type samples. The very first observation of this avoided crossing was reported on HgTe/CdHgTe (001) QWs [[63]]. The splitting was tentatively attributed to BIA; additionally, a possible influence of electron-electron (e - e) interaction was not excluded. Later on, in Ref. [68], an analogous effect has been observed in (013)-oriented samples and also assigned to BIA. Nevertheless, to achieve quantitative agreement with the experimental data, the term describing BIA in the corresponding Hamiltonian had to be taken $3\times$ stronger as compared to the values known for CdTe. The

avoided crossing of zero-mode LLs was clearly visible via α' and β' absorption lines [Fig. 23(c)], for which these zero-mode LLs represent initial states.

Here we report on the avoided crossing of zero-mode LLs in p -doped samples, see Fig. 22 for the magneto-transmission data collected on sample E. Just the observation of the avoided crossing with the magnitude comparable to values reported in Refs. [63] and [68] for samples with the opposite (and higher) doping makes the avoided crossing unlikely to appear due to electron-electron interaction.

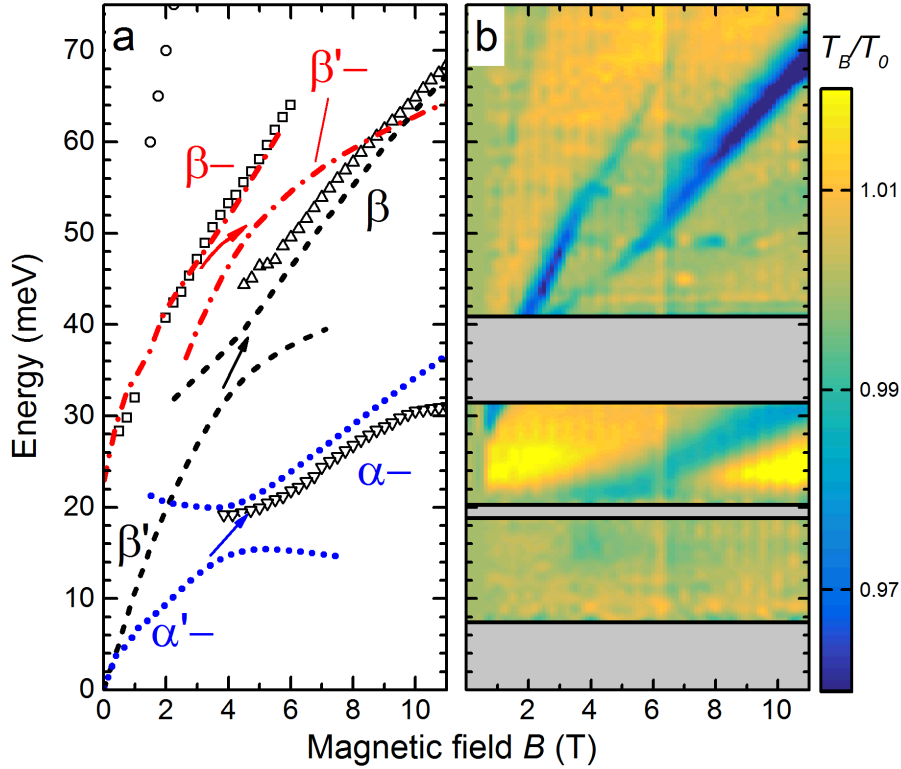


Fig. 22. (a) The energies of $\alpha-$, $\beta-$ and $\beta'-$ transitions, determined experimentally (symbols) and theoretically using the Hamiltonian comprising the symmetry lowering terms. The arrows show the expected transition energies in the axial approximation (without the mixing of LLs). The avoided crossing is experimentally observed in the interval of magnetic fields $B = 2-7$ T. (b) Magneto-transmission of sample E plotted as a false-color plot. The opaque regions of the sample are masked by the horizontal grey areas.

Similar to samples with the normal ordering of bands, the magneto-optical response of sample E with an inverted band gap is dominated by three absorption lines. These are attributed (as justified *a posteriori*) to $\alpha-$, $\beta-$ and $\beta'-$ lines, see Fig. 22. Notably, in contrast to samples with a normal band ordering, the $\beta'-$ transition becomes an interband excitation, while $\alpha-$ and $\beta-$ transitions have an intraband character. The observed response changes rather dramatically its character around 5 T, when the intensity of the $\beta'-$ excitation drops relatively fast and it is replaced by $\alpha-$ and $\beta-$ transitions. This relatively sudden change in the response correlates well with our theoretical expectations based on the Hamiltonian with the symmetry lowering terms. Indeed, the (avoided) crossing of zero-mode LLs is expected at the critical field of $B_c \approx 4.8$ T, as shown in the LL spectrum plotted in Fig. 23(b).

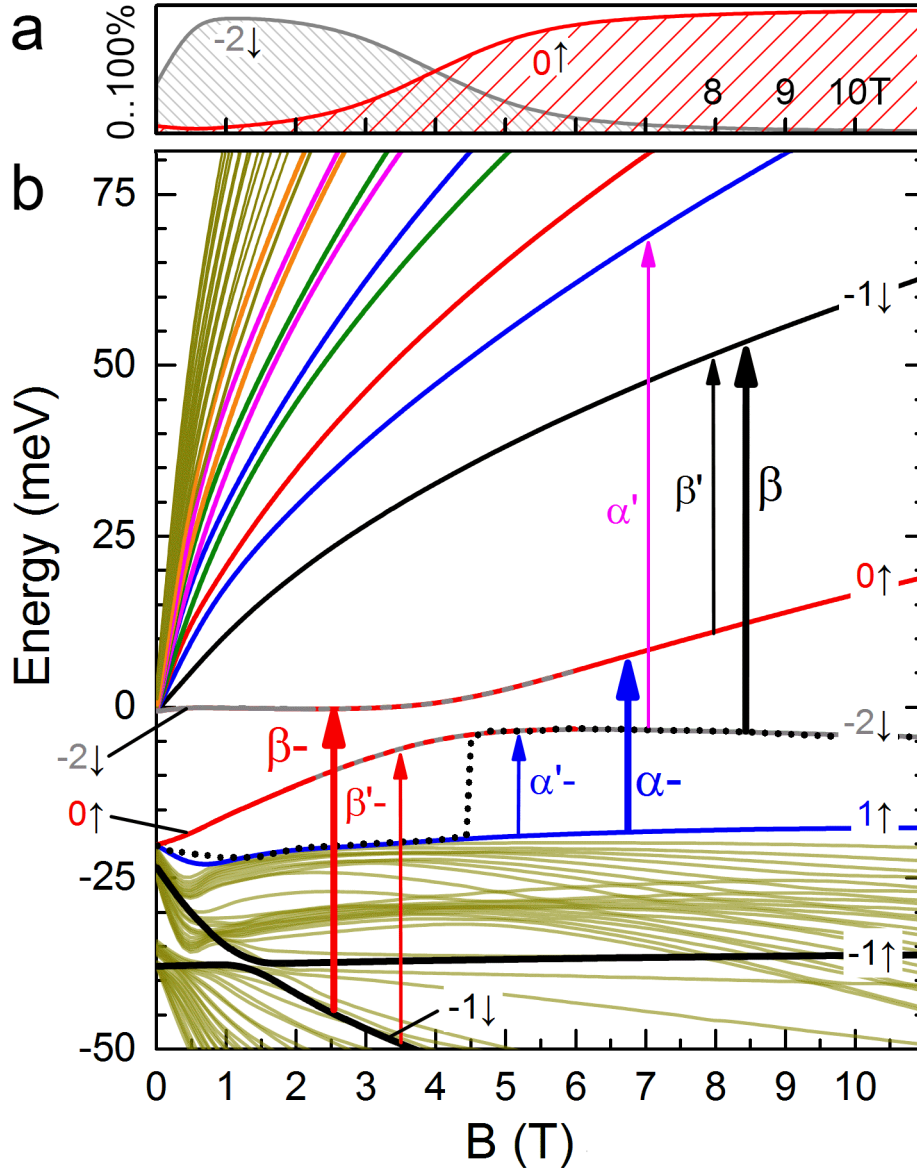


Fig. 23. (a) The admixture of $n = -2_{\downarrow}$ (gray) and $n = 0_{\uparrow}$ (red) states (eigenstates of the axial model) in the lowest LL of the conduction band, which undergoes an avoided crossing with the highest LL of the valence band. (b) The Landau levels calculated within the Hamiltonian comprising all considered symmetry lowering effects. The vertical arrows and Greek letters denote selected electric-dipole excitations: bold arrows are used for lines observed in the magneto-transmission data. The black dotted line shows the Fermi level. The selected Landau levels are identified by the index n and the dominant spin projection.

Let us now focus on interesting details in the magneto-response, which is typical of all p -type samples (as compared to n -type specimens in Refs. [63] and [68]). The magneto-transport data, taken on sample E without any illumination, indicate relatively low hole density, close to $1.1 \times 10^{11} \text{ cm}^{-2}$ ($\nu = 1$ at $B \approx 4.5 \text{ T}$). This implies an approximate field-dependence of the Fermi energy plotted using the dotted line in Fig. 23(b). Similar to samples with a non-inverted band structure, see Fig. 17(a-d), also the response of sample E is dominated at low magnetic fields by the β_{-} excitation, *i.e.*, by the transition denoted as $-1_{\downarrow} \rightarrow -2_{\downarrow}$ in the axial model. In this case, however, the β_{-} excitation is not a CR mode but an interband excitation instead. The position of this line in the spectrum follows the expectations of the axial model at low magnetic fields, see Fig. 22 (a). However, when the critical field B_c is approached, a significant deviation

appears. At the same time, its integral intensity starts to decrease gradually, but the line remains clearly visible well above B_c (up to 8 T). This deviation in energy and the gradual disappearance may only be explained when the symmetry lowering effects – leading to a pronounced avoided crossing of the zero-mode LLs – are taken into account. Without such an avoided crossing, the intensity of the β^- line would drop around B_c rather abruptly due to a simple occupation effect of zero-mode LLs in a nearly undoped sample.

To approach this effect quantitatively, we have plotted in Fig. 23(a) the theoretically calculated admixture of $n = -2_\downarrow$ and $n = 0_\uparrow$ eigenstates of the axial Hamiltonian in the lowest Landau level in the conduction band. One can see that this level is dominantly composed of $n = -2_\downarrow$ (grey) state at low magnetic fields and this state is gradually replaced by the $n = 0_\uparrow$ (red) state with increasing B , but the original state $n = -2_\downarrow$ still remains partly present even at relatively large B , well above B_c . The intensity of the β^- line is proportional to the admixture of the $n = -2_\downarrow$ state in the lowest LL. This results in a gradual – not abrupt as due to a simple occupation effect – disappearance of the β^- line. At the same time, the lower zero-mode LL becomes almost fully occupied around $B = B_c$, which does not allow β^- transition to appear in the spectra.

Above the critical field B_c , two relatively strong resonances emerge in the spectra. Following our calculations, the upper one may be identified as the β transition. It becomes active due to (partial) occupation of $n = -2_\downarrow$ level at $B > B_c$. The line with a lower energy may be associated with α^- transition, see Fig. 22(a). Also for β and α^- transitions, the mixing of zero-mode LLs clearly influences their energies. This is best visible around the critical field B_c when the field dependence flattens significantly. Without the symmetry lowering effects, and consequently, without the avoided crossing of zero-mode LLs, such a flattening could not be explained [cf. Fig. 17 (e)].

Above the critical field of B_c , two strong resonances appear in the response. Following our calculations, the upper one may be identified as β transition. It becomes active due to (partial) occupation of $n = -2_\downarrow$ level at $B > B_c$. The line at lower energies matches well with α^- transition as shown in Fig. 22(a). Also for β and α^- transitions, one may trace a rather clear impact of mixing effects in spectra. These are best visible around the critical field B_c , when the field dependence flattens significantly. Without the symmetry lowering effects, and consequently, without the avoided crossing of zero-mode LLs, such a flattening could not be explained [see Fig. 17(e)].

To conclude, the magneto-optical response of a series of p -type HgTe/CdHgTe quantum wells, with normal as well as inverted band ordering, has been studied in the THz and infrared spectral ranges. We have found that the observed response cannot be fully explained within the standard 4-band model, which is nowadays widely applied and which assumes the full axial symmetry of the system (along the growth axis). We propose that additionally observed spectral features (avoided crossing of transitions and transitions observed, but forbidden in the axial model) have their origin in specific symmetry lowering effects. These mainly include the bulk inversion asymmetry and anisotropy of chemical bonds at the heterointerfaces. Our calculations of the magneto-optical response with both these asymmetries properly included in the corresponding Hamiltonian support this conclusion.

Chapter 4. Observation of the structural inversion asymmetry in quantum well HgTe with selective barrier doping

Cyclotron resonance spectra are studied both in classical and quantizing magnetic fields in asymmetric heterostructures with HgCdTe / CdHgTe quantum wells with selective barrier doping. Self-consistent calculations of the energy spectra (for $B = 0$) and Landau levels in the framework of the 8-band Kane model in the Hartree approximation are performed. The strong splitting of the cyclotron resonance line ($\sim 10\%$) is observed in low fields, which is related to the Rashba effect in samples with both an inverted and a normal band structure. The evolution of the absorption lines with a magnetic field is followed up to 34 T when the magnetic quantization already prevails over the Rashba splitting.

- Bovkun, L.S., et al., Magneto-optics in HgTe/CdTe quantum wells with giant Rashba splitting in magnetic fields up to 34 T. *Semiconductors*, 2019 (in print).

4.1 Experimental details

We investigated two heterostructures with $\text{Hg}_{1-x}\text{Cd}_x\text{Te}/\text{Cd}_{1-y}\text{Hg}_y\text{Te}$ QWs, there is a small content of Cd in QW, while Cd dominate in barriers. Bottom barrier (the one closer to substrate) was selective doped with indium, while the whole structure was grown by molecular beam epitaxy with ellipsometric control of composition and thickness on relaxed CdTe buffer layers on a semi-insulating GaAs (013) substrate [14, 150]. The "active" part of the heterostructure 070704 (sample A, inverted band structure), studied earlier in [25], consisted of the bottom barrier layer of the quantum well $\text{Cd}_{0.6}\text{Hg}_{0.4}\text{Te}$, containing a region doped with a density of $3 \times 10^{18} \text{ cm}^{-3}$ with a thickness of 13.5 nm, then QW itself $\text{Hg}_{0.95}\text{Cd}_{0.05}\text{Te}$ with a width of 15 nm, and an upper barrier layer of $\text{Cd}_{0.53}\text{Hg}_{0.47}\text{Te}$. Sample 070704-1 (hereinafter, sample B) differs mainly in terms of the QW width and composition, which leads to rearrangement of the band spectrum from inverted to normal, analogously to the bulk material [16]). Complete information on the growth parameters of both samples is given in Table V.

Table V. Growth parameters of the investigated heterostructures with QWs

Sample	A (070704)		B (070704-1)	
	Thickness (d), nm	Cd fraction (x)	Thickness (d), nm	Cd fraction (x)
Capping CdTe	40	1	37	1
Upper barrier $\text{Cd}_x\text{Hg}_{(1-x)}\text{Te}$	31,5	0,53	32	0,85
Quantum well $\text{Cd}_x\text{Hg}_{(1-x)}\text{Te}$	15	0,05	13	0,15
Bottom barrier $\text{Cd}_x\text{Hg}_{(1-x)}\text{Te}$	11,5	0,6	9,5	0,89
In-doped barrier $n = 3 \times 10^{18}$	13.5 nm		10 nm	
Bottom barrier $\text{Cd}_x\text{Hg}_{(1-x)}\text{Te}$	5,5	0,6	5	0,89
Relaxing CdTe	5-6 μm			
ZnTe (define growth direction)	30 nm			
Substrate GaAs (0 1 3)	400 μm			

The magneto-optical study using the Fourier spectroscopy technique was carried out at the Laboratoire National des Champs Magnétiques Intenses, Grenoble (France) in the Faraday configuration on samples 5×5 mm in size in magnetic fields of up to $B = 11$ T at $T = 4.2$ K using a superconducting solenoid and in fields of up to 34 T at 1.6 K using a resistive solenoid. The presented spectra were recorded with a resolution of 0.5 meV and normalized to zero magnetic-field measurements with regard to the bolometer-sensitivity variation. The magnetotransport measurements were performed simultaneously with the optical measurements in the van der Pauw geometry in fields of up to 11 T at 4.2 K. The modulated

signal from a synchronous detector at a frequency of $f \sim 17$ Hz was applied to the current contacts. The current value was chosen to exclude the heating of carriers. Measurement was performed in several contact configurations (longitudinal and transverse resistances).

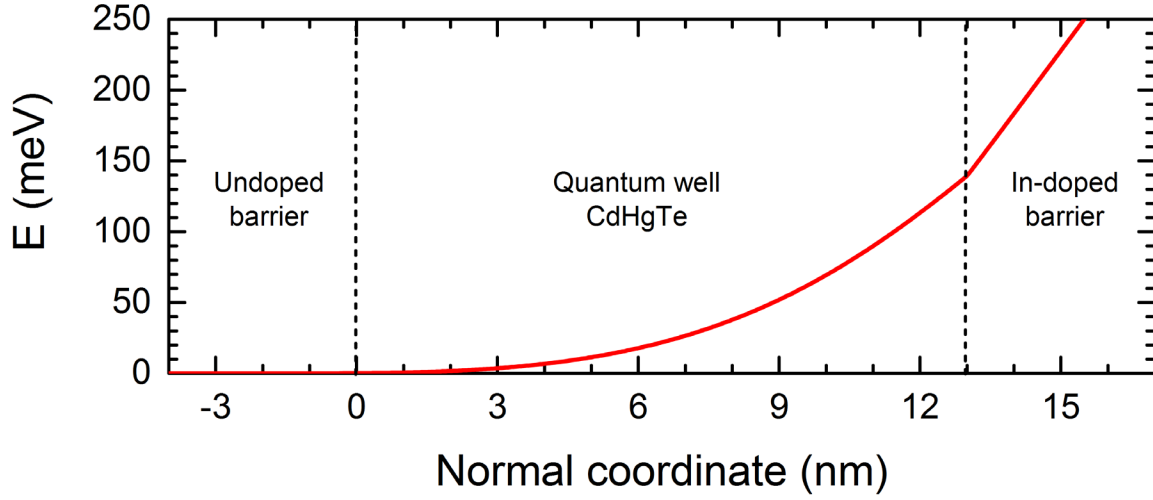


Fig. 24. Potential energy of an electron is self-consistent field theory for sample B.

To interpret the experimental results, we calculated the band structure $E(k_x, k_y)$ in zero magnetic field using the 4-band Kane model with regard to bulk inversion asymmetry (BIA) of the crystal lattice [68, 69] and the anisotropy of chemical bonds at the QW interface (interface inversion asymmetry, IIA) [70, 71]. Structural asymmetry caused by one-sided selective doping (structure inversion asymmetry, SIA) was taken into account in the Hartree approximation [152]. The obtained QW potential profile (see Fig. 24) was then used to calculate the Landau levels in the axial 4-band model (disregarding the BIA and IIA).

Table VI. Total charge-carrier density and distribution over the subbands according to Fourier analysis of the SdH oscillations in the investigated samples.

Sample	Total concentration $n_s, 10^{12} \text{ cm}^{-2}$	$n_2, 10^{11} \text{ cm}^{-2}$	$n_{1+}, 10^{11} \text{ cm}^{-2}$	$n_{1-}, 10^{11} \text{ cm}^{-2}$
A	1.7	3.9	5.6	7.5
B	2.8	4.7	10.7	13.0

The magnetotransport study revealed pronounced beating patterns in the Shubnikov-de Haas oscillations in both samples (see Fig. 25 for sample B and [25] for sample A), which are indicative of the existence of several carrier types in the QW. Fourier analysis of the SdH oscillations revealed three groups of charge carriers corresponding to the E_2 , H_1^+ and H_1^- quantum-confinement subbands for sample A (Fig. 26(a)) and E_2 , E_1^+ and E_1^- for sample B (Fig. 26(b)). The oscillation beating is caused by spin splitting of the $H_1(E_1)$ subband, whereas the E_2 band is characterized by a single peak (compare with [25, 57]). The resulting two-dimensional electron gas densities $n_s = n_2 + n_{1+} + n_{1-}$ were 1.7 and $2.8 \times 10^{12} \text{ cm}^{-2}$ (detailed results of the Fourier analysis of the oscillations are given in Table VI). It is noteworthy that the ratios between the densities in the $H_1^+(E_1^+) / H_1^-(E_1^-)$ bands are 1.34 and 1.25 for samples A and B, respectively, and the charge-carrier fractions in the second subband are 23 and 18%, which evidences the differences in both the spin splitting and Fermi-level positions. The minor differences of the results for sample A from the data of a similar analysis performed in [25] are related to the fact that physically different parts of the same heterostructure were investigated.

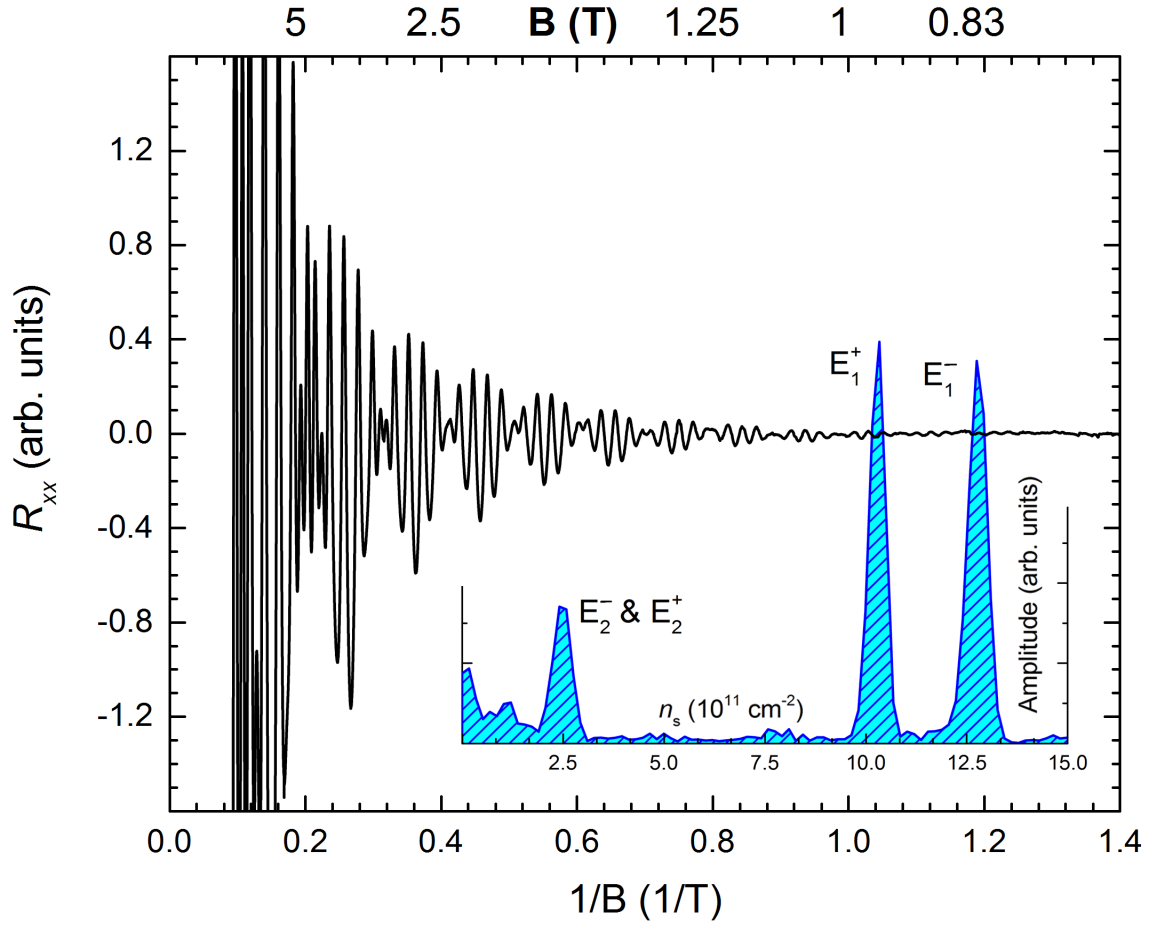


Fig. 25. Shubnikov-de Haas oscillations in sample B vs the inverse magnetic field. Carrier densities found from the Fourier analysis of SdH oscillations in overlay.

The obtained total densities were used in self-consistent calculations of the band structure of the investigated samples in the Hartree approximation (Fig. 26). According to our calculations, the band structure of sample A is inverted and the lower subband H1 in the conduction band is formed mainly by heavy-hole states Γ_8 . In contrast, sample B has a normal band structure, where the lower subband E_1 in the conduction band is formed mainly by electron states Γ_6 (see the inserts in Fig. 26(a, b)).

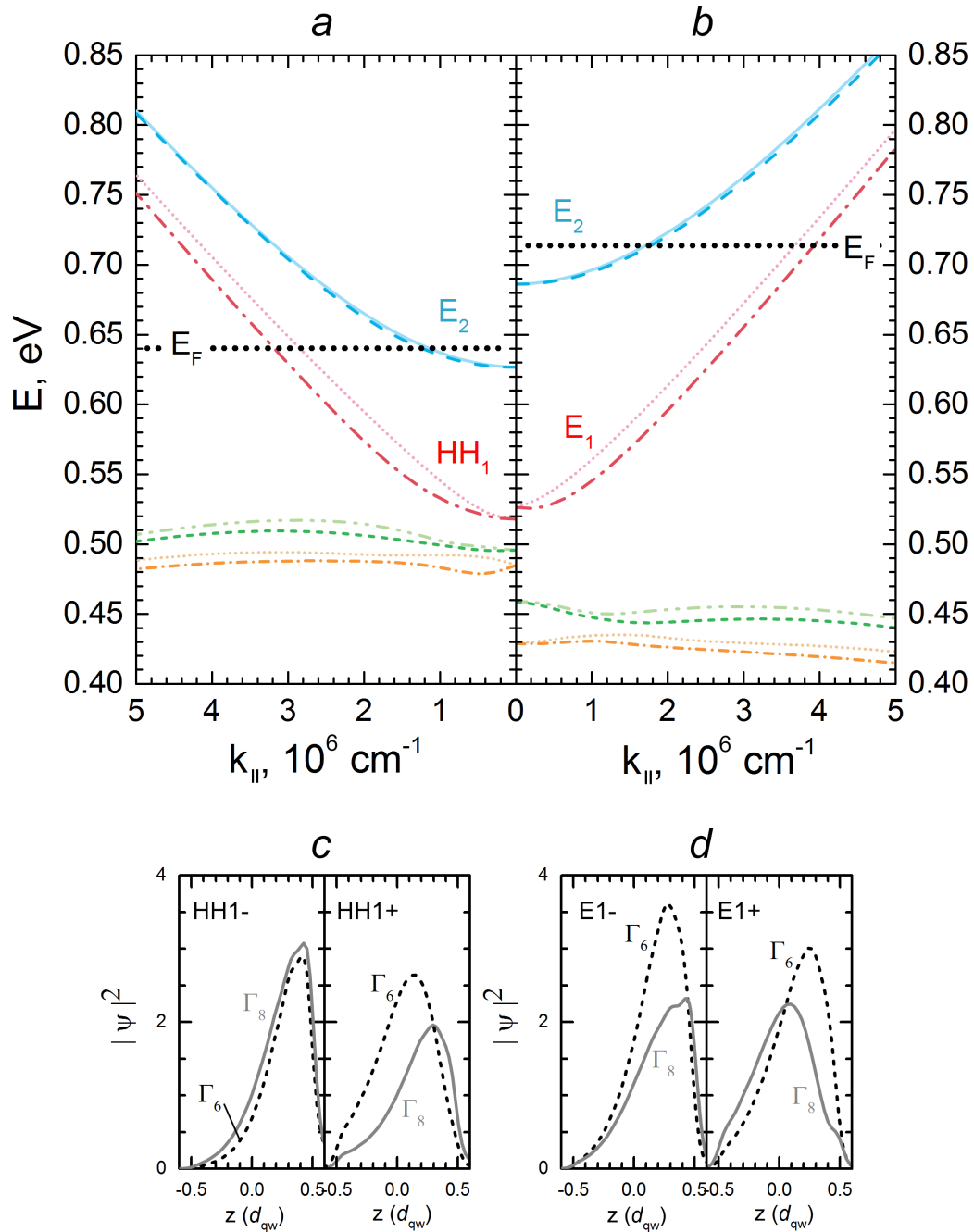


Fig. 26. Calculated $E(k)$ dispersion law with regard to low symmetry effects for sample A at a density of $n_s = 1.7 \cdot 10^{12} \text{ cm}^{-2}$ (a) and sample B at a density of $n_s = 2.8 \cdot 10^{12} \text{ cm}^{-2}$ (b). A thick horizontal dotted line shows the Fermi-level position. (c, d) The sums of the squared absolute values of the wave functions of the s-type (Γ_6) and p-type (Γ_8) states for the lower spin-split conduction subband at $k = 4 \times 10^6 \text{ cm}^{-1}$.

It can be seen in Fig. 26 that the calculation predicts significant spin splitting of the lower subband in the conduction band for both samples, which attains 21 meV for sample A and 17 meV for sample B. Such a giant spin splitting for the inverted band structure from [57, 59] was attributed to the hole character of the states of the subband H1, which leads to stronger spin-orbit interaction as compared with, say, the electron-like subband E2, the states of which are formed mainly by s-type wave functions. Indeed, as can be seen in Fig. 26(c), the contribution

of p -type states to the 8-component wave function in the subband H1 reaches 50%. At the same time, it turns out that in the sample with the normal band structure and relatively wide (~ 65 meV) band gap (Fig. 26(b)), the states of the E1 subband contain a noticeable fraction of p -type wave functions (see Fig. 26(d)), which leads to its noticeable spin splitting, multiple of the splitting of the second subband E2. We note that taking into account the BIA and IIA effects introduces an additional correction to the spin splitting. For instance, in the H1 band, the spin splitting increases by 1–2 meV, which is lost against the Rashba-splitting value $\propto k_{\parallel}^3$; however, in the subband E2, the BIA and IIA splitting is 2–3 meV, which is higher than slight Rashba splitting $\propto k_{\parallel}$ since the share of Γ_8 state is negligible.

4.2 Irregular splitting of cyclotron resonance modes

Fig. 27 shows the measured transmission spectra in magnetic fields of up to 9.8 T. Due to a high carrier density, the normalized absorption by a magnetic field on the CR is tens of percent (in [24], it reaches 30%, but at a lower density). In this study, we observe a complex structure of intraband absorption feature. For specific values of magnetic field, we obtain plain and clear double-peaked spectrum of cyclotron resonance modes, while we clearly can notice additional absorption feature is in-between, which is indicative of significant magnetic-quantization effects. This is related, first of all, to the subband E2 with a lower electron density, in which only 4–5 Landau levels are filled even in a field of $B = 4$ T. The calculated band mass in the E2 subband at the Fermi level in both samples appears somewhat smaller than the effective masses in the lower split subband. As the magnetic field increases, the population of the Landau levels, between which cyclotron transitions occur, changes, which apparently leads, under the conditions of nonparabolic dispersion $E(k)$ [27], to the observed oscillations of the splitting of the CR line, which is a superposition of absorption on the cyclotron transitions in both quantum-confinement subbands. As was shown in the previous experimental studies in inclined fields [24, 57], the Zeeman correction is insignificant, and, in addition, intersubband scattering is excluded [141].

The insets in Fig. 27 show the position of the absorption maxima for the spectra where pronounced CR line splitting ($\Delta E/E_{\text{res}} \approx 8\text{--}10\%$) is visible and straight lines are constructed, which correspond to effective masses of $0.0376 m_0$ and $0.0417 m_0$ (a difference of 9.9%) for sample A and $0.0459 m_0$ and $0.498 m_0$ (a difference of 7.8%) for sample B (m_0 is the free electron mass, respectively). In [24], this splitting was attributed to the difference between the cyclotron electron masses at the Fermi level in two branches of the spin-split subband H1. The calculations of the dispersion law using the Hartree approximation allowed us to estimate the band masses from the dispersion relation as follows:

$$dE/dk = \hbar^2 k/m^*, \quad \text{Eq. 5}$$

Calculations of the dispersion law for different directions of the k vector in the xy -plane (the QW plane) showed that, at the Fermi level, the dispersion law is axially symmetric with good accuracy. Therefore, taking into account spin splitting, the k values at the Fermi level for each subband can be calculated as

$$k_F = \sqrt{4\pi n}, \quad \text{Eq. 6}$$

where n is the charge-carrier density in the subband determined from analysis of the SdH oscillations. The results obtained are given in Table VII together with the experimental values presented above. It can be seen that the absolute values (m_1^* and m_2^*) of the calculated effective masses agree reasonably with the experiment, but the calculated mass difference ($1 - m_1^*/m_2^*$) in the spin-split lower subband of the conduction band in both investigated samples was significantly smaller than that observed in the experiment. The nature of this discrepancy in classical magnetic fields is unclear; it does not fit the single-electron analysis and is possibly related to collective effects. We note that significant CR-line splitting in asymmetric QWs with

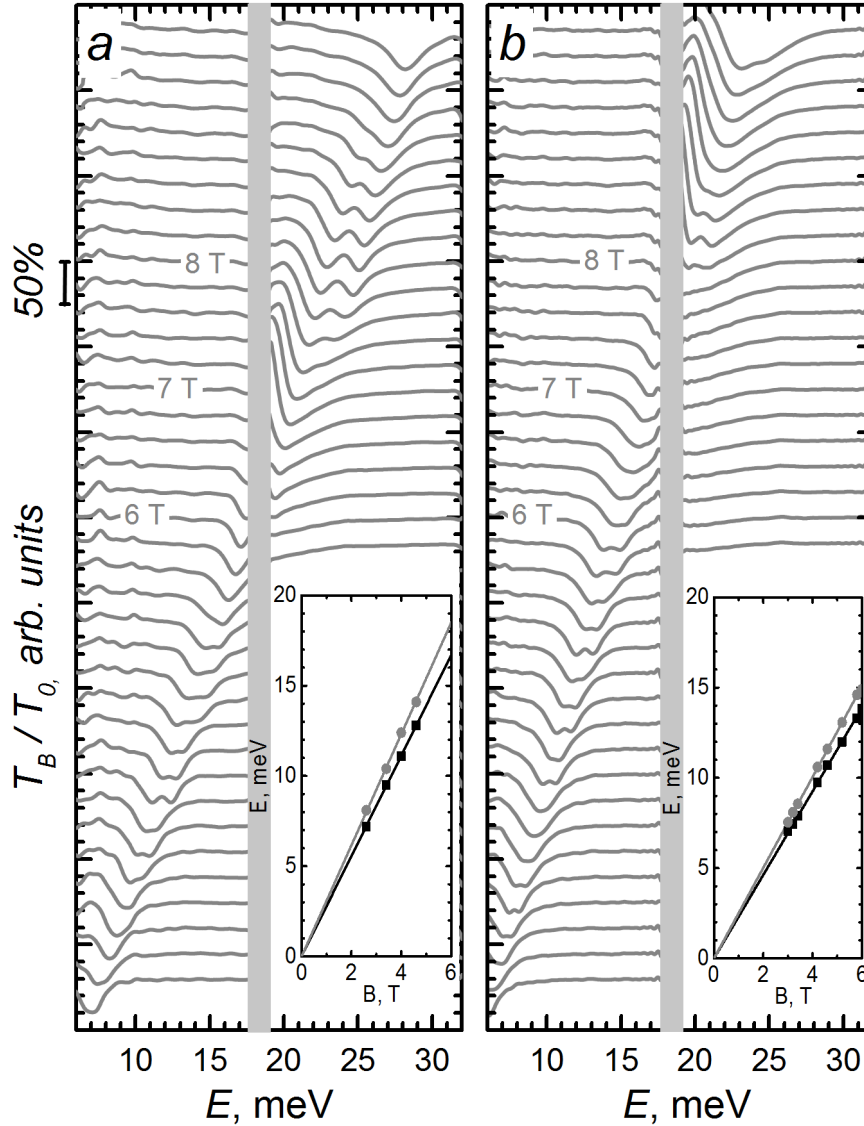


Fig. 27. Characteristic transmission spectra in magnetic fields from 2.4 to 9.8 T with a step of 0.2 T for samples A (on the left) and B (on the right). The spectra corresponding to magnetic fields of 6, 7, and 8 T are marked in the plot. The normalized transmittance attains 50%; the characteristic scale is marked on the left axis. The insets show the positions of the absorption maxima (symbols).

inverted band spectra was observed also in [25], where it was $\sim 10\%$ in a field of 1 T at an electron density of $2 \times 10^{12} \text{ cm}^{-2}$ and in study [24], where it was $\sim 7\%$ in a field of 3 T at an electron density of 10^{12} cm^{-2} .

Table VII. Experimental and calculated cyclotron masses in the spin-split lower subband

Sample		m_1^*	m_2^*	$1 - m_1^* / m_2^*$
A	Experiment	0,0376	0,0417	9,9%
	Calculation	0,0397	0,0414	4,1%
B	Experiment	0,0459	0,0498	7,8%
	Calculation	0,0448	0,0463	3,2%

4.3 Spin vs magnetic quantization in fields up to 34 T

In magnetic fields stronger than 6 T, the field dependence of the CR modes becomes sublinear (Fig. 27). In this quantizing-magnetic-field region, discussion of the results in terms of effective mass is meaningless. Indeed, in sample A, a magnetic field of 7 T corresponds to the Landau-level filling factor $\nu \approx 10$ (in this case, only two levels are filled in the second subband E2) and, in sample B, $\nu \approx 16$. Below, we discuss the transitions between Landau levels for only sample A, which was investigated in magnetic fields of up to 34 T (Fig. 28).

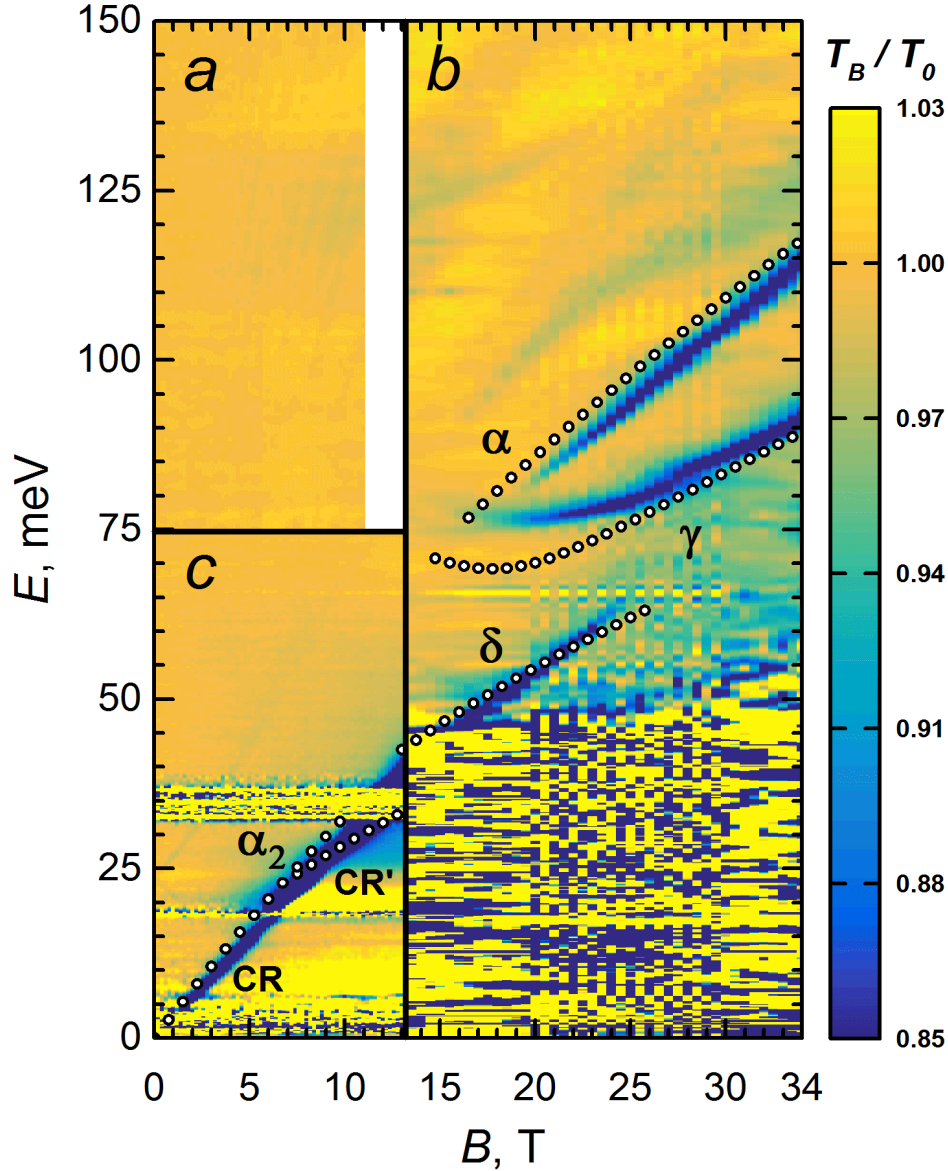


Fig. 28. Frequency and magnetic-field dependence of the transmittance of sample A at $T = 1.6$ K. The darker color corresponds to stronger absorption (see the scale on the right). The results were obtained in three experiments in different optical configurations: (a) ZnSe filter and KBr beam splitter, (b) Ge filter and KBr beam splitter, (c) black polyethylene filter and T222 mylar beam splitter. Symbols in (b) show the calculated energies of γ_2 , δ , γ and α transitions between the Landau levels discussed in the text. At energies below 50 meV, the KBr beam splitter is opaque. In (c), there are also two opacity regions: the region around 20 meV related to phonon absorption in CdHgTe and the region around 35 meV corresponding to the reststrahlen band of GaAs substrate.

Fig. 29 shows the Landau levels in sample A calculated in the axial approximation. Vertical arrows show selected transitions active in the electric dipole approximation ($\Delta n = 1$ for the case of spin conservation) indicated by Greek letters in line with notation introduced earlier in study [26]. The polygonal line shows the calculated Fermi-level position $E_F \approx 641$ meV. As can be seen in Fig. 27(a), there are two absorption lines in the magnetic-field range of 7.8–9.2 T, which are not resolved in Fig. 28 due to their weak contrast against the strong background absorption. The higher-frequency line apparently corresponds to the transition of α_2 within the subband E2 and its damping in fields above 9.2 T is attributed to depletion of the Landau level $n = -1_{\downarrow}$, which is the initial level for the transition. The lower-frequency line continues the classical CR in the subband H1.

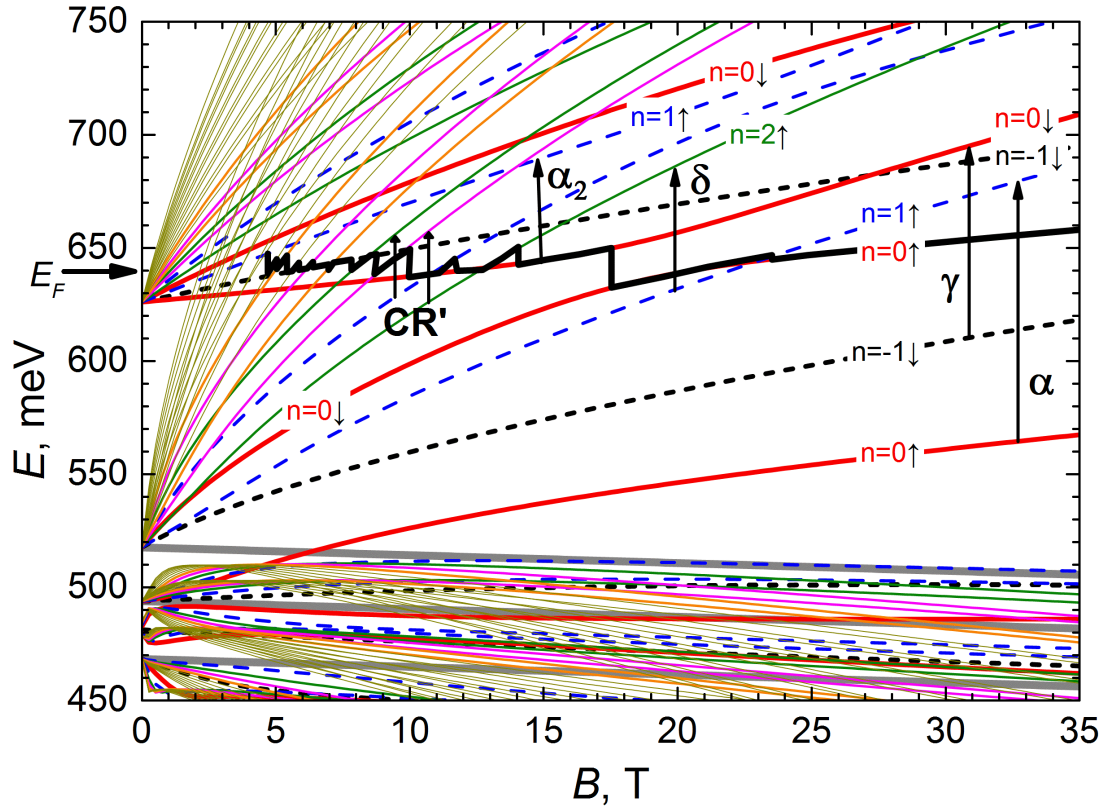


Fig. 29. Calculated Landau levels for sample A. The polygonal line shows the approximate Fermi-level position in the magnetic field. Vertical arrows show the allowed γ_2 , α_2 , δ , γ , α magneto-optical transitions (see the text) with an increase in the Landau-level number.

The magneto-absorption spectra in higher (up to 34 T) magnetic fields, in which magnetic-quantization, i.e. Landau level splitting, effects prevail over Rashba spin splitting, illustrate the transition from the classical to quantum CR and in the first quantum-confinement subband H1. As can be seen in Fig. 28, in fields over 15 T, there are three intense absorption lines corresponding to optical transitions from the three lower Landau levels in the conduction band H1 (Fig. 29). The transitions γ and α represent a quantum limit of cyclotron transitions in classical magnetic fields in two Landau-level ladders in the spin-split subbands H_{1-} and H_{1+} . The δ line, which continues the classical CR line, corresponds to the transition from the level $n = 1_{\uparrow}$ to the level $n = 2_{\uparrow}$ in the conduction band H_{1-} . The magnetic fields in which α and γ lines arise and δ line decays correspond, at first, to depopulation of the final Landau levels $n = 1_{\uparrow}$ and $n = 0$ for the investigated transitions and, in the second case, to depopulation of the initial

Landau level $n = 1_{\uparrow}$ for the δ transition. Thus, δ line decay leads to occurrence of α line. The unusual γ line bending in the field range of 15–20 T (Fig. 29) reflects the anticrossing of the interacting Landau levels $n = 0$ from the subbands H1 and E2 (Fig. 28) in these fields. It is noteworthy that, according to calculations, the probabilities of transitions from the level $n = -1_{\downarrow}$ in a field of 20 T to the levels $n = 0_{\downarrow}$ and $n = 0_{\uparrow}$ are similar due to state mixing at these levels [148]. The latter transition can be related to the horizontal absorption line with an energy of 52 meV in the magnetic field range of 15–20 T, which is poorly distinguished at the noise level due to the proximity of the absorption edge in the KBr beam splitter.

To conclude, we investigated the absorption spectra and magnetotransport in asymmetric heterostructures with HgCdTe/CdHgTe quantum wells with selective barrier doping with a high electron density ($\sim n_s \sim 2 \times 10^{12}$) in the samples with inverted and, for the first time, normal band spectra. Using the Fourier analysis of Shubnikov-de Haas oscillations, we determined the electron densities in two populated quantum-confinement subbands in the conduction band. To interpret the experimental results, self-consistent calculations of the energy spectra at $B = 0$ with regard to the absence of an inversion center in the crystal lattice and the anisotropy of chemical bonds at the heterointerfaces and the Landau levels in the 4-band Kane model were made in the Hartree approximation. At weak magnetic fields, a strong cyclotron resonance line splitting was observed, which is related to the Rashba effect and reaches $\sim 10\%$ in the sample with the inverted band structure and 8% in the sample with the normal one. It was shown that, in both cases, in the states of the lower subband of the conduction band, there is a large (up to 50%) admixture of p -type (hole) wave functions, which leads to giant (over 20%) spin splitting of the lower subband at the Fermi level. The CR-line splitting oscillations with the field were found and attributed to magnetic quantization in the upper subband with a smaller number of filled Landau levels. The magnetic-field evolution of the absorption lines was investigated up to 34 T, when the magnetic quantization already prevails over the Rashba splitting. In magnetic fields of 15–20 T, the absorption spectra reveal the anticrossing of Landau levels from the first and second quantum-confinement subbands.

Chapter 5. Activation conductivity in HgTe/CdHgTe quantum wells at integer Landau level filling factors: role of the random potential

Shubnikov-de Haas oscillations have been studied in 8-nm-wide HgTe/CdHgTe quantum wells with an electron concentration of $(1.7\text{--}13)\times 10^{11}\text{ cm}^{-2}$ in the temperature range from 1.6 to 40 K. The gaps between Landau levels and the quantum relaxation time have been determined from the temperature dependence of the oscillation amplitude at integer filling factors. The experimental gap values are found to be in good agreement with the results of the single-particle calculation of the level energies using the 8-band Kane model. The experimental widths of the density of states are indicative of a profound screening of the exchange interaction in HgTe/CdHgTe quantum wells.

- Bovkun, L.S., et al., Exchange enhancement of the electron g-factor in a two-dimensional semimetal in HgTe quantum wells. *Semiconductors*, 2015. 49(12): p. 1627-1633.
- Bovkun, L.S., et al., Activation conductivity in HgTe/CdHgTe quantum wells at integer Landau level filling factors: role of the random potential. *Semiconductors*, 2017. 51(12): p. 1562-1570.

As already noted in this manuscript, an effective method for studying the band structure of the HgTe / CdHgTe quantum well is magnetospectroscopy in THz and in the middle IR ranges where both intraband and interband carrier transitions occur (e.g. [23, 28, 60, 88, 89, 115]). In other sections, this approach was used to investigate the single and double *p*-type QWs. However, this method does not allow us to determine the energy distances between neighboring Landau levels with opposite spins, since such transitions are forbidden by the selection rules in the electric dipole approximation. At the same time, magnetotransport measurements make it possible to trace the successive movement of the Fermi level over the Landau levels (for example, changing its position with the aid of a shutter) and thus restore the picture of the Landau levels in a magnetic field (e.g. [131, 153]). The strong spin-orbit interaction in the HgTe/CdHgTe quantum well leads to large values of the spin splittings of the states and the effective g-factor of the electrons (reaching values of 50 and higher [60, 88, 89]). As a result, the pronounced quantum Hall effect and Shubnikov-de Haas oscillations are observed even in magnetic fields $B \sim 0.1\text{ T}$ [115] and at high temperatures [154, 155].

In the present chapter, we report on measurements of the activation conductivity in perpendicular magnetic fields, which were used to determine the distances between neighboring Landau levels in the conduction band in the HgTe/CdHgTe quantum well [133-135]. If the Fermi level lies in the region of localized states between neighboring Landau levels, the thermal excitation of electrons into delocalized states at the higher level leads to an activation behavior of the conductivity with increasing temperature. Thus, by analyzing the temperature dependence of the amplitude of the SdH oscillations for various occupation factors of the Landau levels ν , it is possible to determine the magnitude of the mobility gap Δ_T .

5.1. Experimental details

In the present chapter, we study HgTe/CdHgTe samples containing QWs with similar growth parameters; the samples were prepared by molecular-beam epitaxy on a semi-insulating GaAs(013) substrate [14, 150]. A ZnTe buffer layer, relaxed CdTe buffer layer, lower $\text{Cd}_x\text{Hg}_{1-x}\text{Te}$ barrier layer, 8-nm-thick HgTe QW, upper $\text{Cd}_x\text{Hg}_{1-x}\text{Te}$ barrier layer, and CdTe coating layer were sequentially grown. To form the 2D electron gas, the barriers were symmetrically doped with shallow donors (indium) on both sides of the QW.

The QHE and SdH oscillations were measured upon sweeping the magnetic field up to 12 T, in the temperature range from 1.6 to 40 K. We used a Cryofree SC magnet system consisting of two cryostats, one of which contains a superconducting solenoid with a room temperature aperture of 52 mm in diameter; the second, variable temperature cryostat (Optistat PT) was inserted in this aperture. The 2D electron concentration was determined from the period of the SdH oscillation and from the slope of the magnetic field dependence of the Hall resistance R_{xy} . Typical magnetic-field dependences of the longitudinal (R_{xx}) and transverse resistances are presented in the inset of Fig. 30. The n_s values obtained using the two techniques are consistent within the measurement error, which indicates the absence of parallel conduction channels in the investigated samples. In addition, the absence of the parallel conductivity channels is confirmed by zero longitudinal resistance at high magnetic fields.

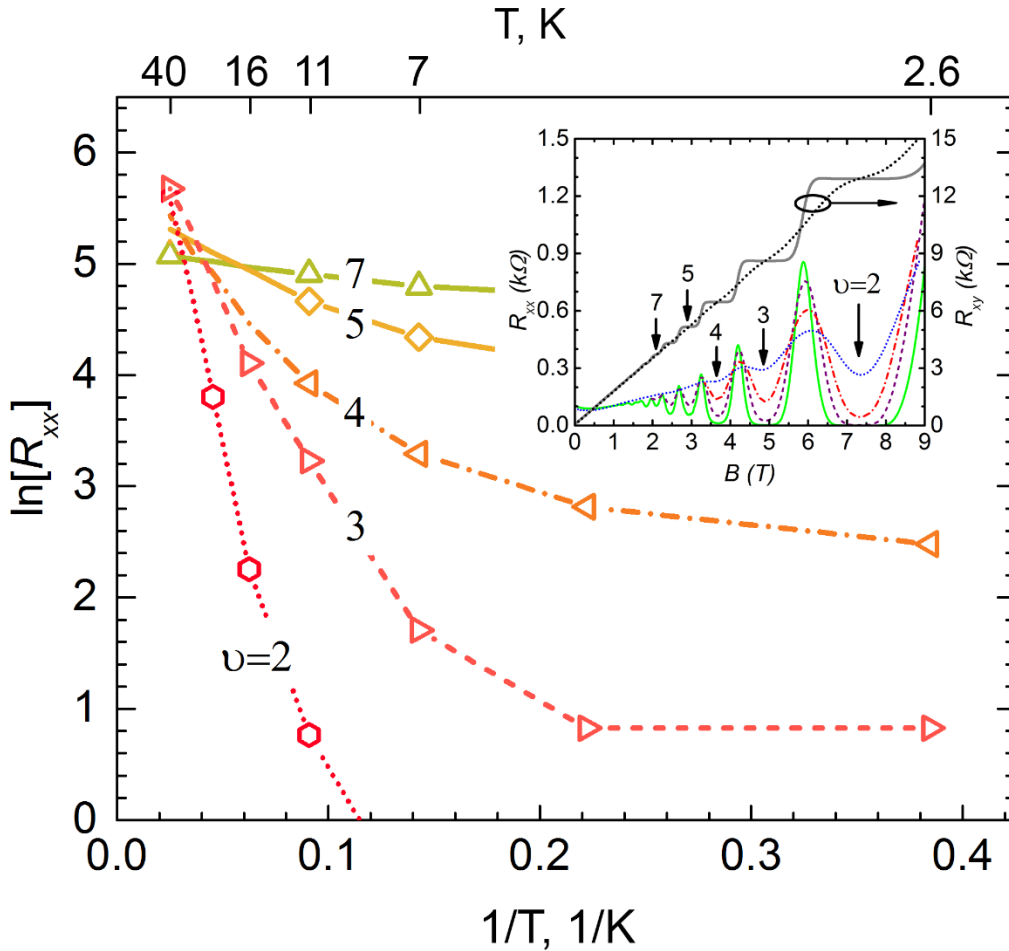


Fig. 30. Arrhenius plots for sample 091223*; the integer filling factors of the Landau levels for each curve are specified. The inset: magnetic-field dependences of R_{xx} ($T = 2.6, 11, 22, 40$ K) and R_{xy} ($T = 2.6$ K for the solid curve and $T = 40$ K for the dotted curve) are shown. Vertical arrows indicate magnetic fields corresponding to the integer values of ν .

Table VIII lists the growth and electrical parameters, as well as the parameters determined for the investigated samples using the Lifshitz–Kosevich theory. The asterisk marks the samples subjected to short-term illumination by a blue light-emitting diode [27], which cause corresponding changes in transport properties. The electron concentration in these latter samples is higher due to the persistent photoconductivity effect, which remained constant during the experiment. This is confirmed by the reproducibility of longitudinal magnetoresistance minima measured in the course of experiment with different temperatures.

Table VIII. Parameters of the investigated structures. The samples are presented in order of increasing electron concentration n_s

Growth parameters			Transport data (1.6 K)			Lifshitz-Kosevich model		
Sample	d_{qw} , nm	x	n_s , 10^{11} cm $^{-2}$	μ , 10^3 cm 2 /V s	τ_{tr} , ps	m_{LK}^* , m_0	Γ_L , meV	α
101221*	8.0	41	1.70	198	2.25	0.020	5.6	38.6
091223	8.0	62	1.90	77	0.74	0.017	8.3	18.7
091222*	8.0	70	3.40	45	0.54	0.021	10.3	17
091223*	8.0	62	3.60	80	1.10	0.024	5.5	18.4
101109	8.0	77	5.50	100	1.49	0.026	4.9	22.6
130212	8.3	78	13.0	70	1.46	0.037	5.8	25.3

5.2. Determination of the mobility gap Δ_T and broadening Γ

At low temperatures, the SdH oscillations occur if the energy gap between the Landau levels near the Fermi level exceeds the width of the density of states of neighboring levels. In high magnetic fields, when the densities of states of the Landau levels do not overlap, the longitudinal conductivity and R_{xx} turn to zero. As the temperature is increased, the probability of the thermal transfer of electrons to the Landau level located above the Fermi level grows, which, in turn, leads to an increase in conductivity. If the mobility gap Δ_T between the neighboring Landau levels significantly exceeds the thermal energy $k_B T$, then the temperature dependence of the magnetoresistance at a fixed magnetic field is expressed as [136, 156, 157]:

$$\sigma_{xx} = \sigma_0 \exp\left(-\Delta_T/2k_B T\right) \quad \text{Eq. 7}$$

where Δ_T and σ_0 are temperature-independent. The typical dependences of R_{xx} at the minima corresponding to integer filling factors ν on the reciprocal temperature are presented in Fig. 30.

The mobility gap Δ_T is determined from the slope of the curves in the Arrhenius plot in the high-temperature region. At low temperatures, we observe a decrease in the slope of the curves and even saturation of the dependences, which is apparently related to the contribution of hopping conductivity [158, 159]. At large (over $\nu = 6$) filling factors, in the weak-field region of the onset of SdH oscillations, the parameter Δ_T is very small due to a significant overlap of the densities of states of Landau levels. Δ_T increases with magnetic field strength, in our case, steadily, for all heterostructures, except for sample 130212 with the highest concentration (see below).

The presence of the random potential (due to scattering centers) in 2D systems leads to broadening of Landau levels. Studying the magnetoresistance oscillations in a magnetic field at different temperatures makes it possible to determine the effective mass m^* and quantum relaxation time τ_q for charge carriers; the latter time determines the Landau-level broadening. The oscillations of ΔR_{xx} in weak magnetic fields can be described using the formula [168, 169]:

$$\Delta R_{xx}/R_0 = 4 \frac{\psi}{\sinh(\psi)} \exp\left(\frac{-\pi}{\omega_c \tau_q}\right) \cos\left(\frac{2\pi \epsilon_F}{\hbar \omega_c} - \Phi\right) \quad \text{Eq. 8}$$

where R_0 is the sample resistance in zero magnetic field, $\omega_c = eB/m^*c$ is the cyclotron frequency, ϵ_F is the Fermi energy, $\psi = 2\pi^2 k_B T / \hbar \omega_c$ determines the temperature dependence of the SdH oscillation amplitude, and Φ is the oscillation phase. Expression (Eq. 8) corresponds to the Lorentzian profile of the density of states at the Landau levels [170, 171]. In this case, formula (Eq. 8) at a fixed temperature can be presented in the form:

$$\Delta R_{xx}/R_0 = A \cdot \exp\left(-2\pi\Gamma_L/\hbar\omega_c\right) \quad \text{Eq. 9}$$

where A is the fitting parameter and $\Gamma_L = \hbar/2\tau_q$ is the width of the density of delocalized states at the Landau levels. Similar calculation for the Gaussian profile of the density of states yields the following expression for the SdH oscillation amplitude [171]:

$$\Delta R_{xx}/R_0 = A \cdot \exp\left(-\pi^2 \left[\Gamma_G/\hbar\omega_c\right]^2\right) \quad \text{Eq. 10}$$

Thus, the shape and extent of broadening of the density of states at the Landau levels in a specific sample can be determined by analyzing the dependence of the logarithm of the SdH oscillation amplitude on the inverse magnetic field from the type of field dependence (linear or quadratic). Typical Dingle (the term accepted in the publications [166]) plots for different samples are shown in Fig. 31.

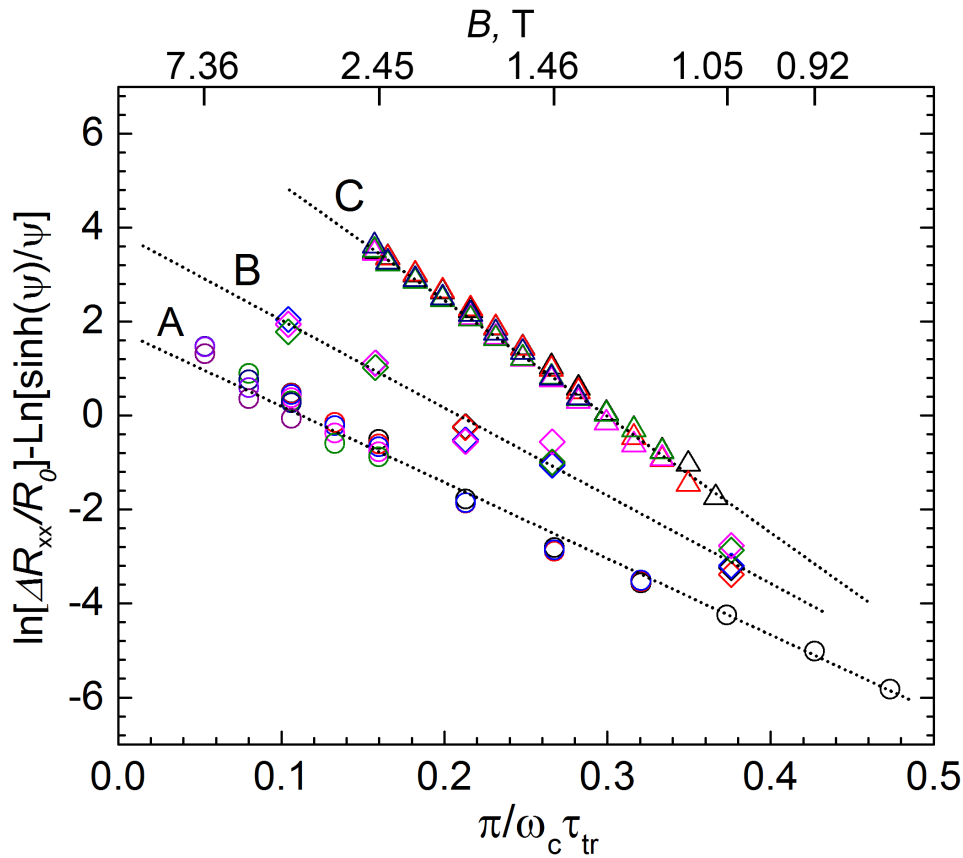


Fig. 31. Dingle plots [166] for samples 091223* with the linear approximation $y = 5.5 - 18.4x$ (A), 091223 with the linear approximation $y = 3.88 - 18.7x$ (B), and 130212 with the linear approximation $y = 3.53 - 25.3x$ (C, shifted by +2 along the ordinate axis for clarity).

The effective mass m^* was determined by least squares fitting of experimental data, the result is shown in Fig. 31. The results of analysis based on Lifshitz–Kosevich theory are listed in Table VIII. The obtained effective masses are in good agreement with the experiment on cyclotron resonance observation (sample A is 091222 in [23] and 091223 in [27]) and are qualitatively consistent with the theoretical dependence of the effective mass on the concentration.

All the investigated samples exhibit a linear dependence of the logarithm of the resistance R_{xx} on the reciprocal magnetic field. The slope of the linear dependence in Fig. 31 corresponds to the value $\alpha = \tau_{tr}/\tau_q$ and determines the type of scattering: unity at the short-range (δ -correlated) potential of the scattering center and larger than unity for a random potential with a finite correlation length [160]. In the case under consideration, the parameter α is in the range 17–38. The transport relaxation time was determined from the formula $\tau_{tr} = \mu m^*/e$; after that, the parameter $\Gamma_L = \hbar/2\tau_q = \alpha\hbar/2\tau_{tr}$ was calculated. It can be seen from Table VIII that the width of the density of states Γ_L at the Landau levels in the investigated samples amounts at least to 5 meV. Thus, it is incorrect to consider the region of delocalized states at the Landau levels to be infinitely narrow, as was considered in [154, 155].

It is of interest to compare the results obtained before and after short-term illumination of sample 091223 by a blue light-emitting diode. Illumination changes the electrical parameters: the concentration n_s and the effective mass m^* increase from 1.9×10^{11} to 3.6×10^{11} cm⁻² and from 0.017 to 0.024 m_0 , respectively. At the same time, the mobility μ increases from 7.7×10^4 to 8×10^4 cm²/(V s). The latter is indicative of an increase in the transport relaxation time τ_{tr} from 0.74 to 1.1 ps at almost invariable mobility. This is caused by a noticeable change in the effective mass. It can be seen from Fig. 31 that, in this case, the parameter α (angular coefficient of the Dingle plot) changes insignificantly, which eventually leads to a decrease in the parameter Γ_L from 8.3 to 5.5 meV. Such a variation can be related to the enhancement of screening of the random potential with increasing carrier concentration.

5.3. Determination of the energy gaps

In the previous sections, we described the techniques for determining the values of Δ_T and Γ_L . In our model, these values allow us to determine the energy gaps ΔE (see the inset in Fig. 32) [142]:

$$\Delta E = \Delta_T + \Gamma \quad \text{Eq. 11}$$

where Γ is the width of the density of states at the Landau levels (see below). We note that the chosen technique for determining ΔE is not commonly accepted. In particular, in some early studies with inversion layers in Si and GaAs/AlGaAs heterojunctions, it was believed that the parameter Δ_T should be doubled due to the nonzero “background” density of states between the Landau levels (see, for example, [134]). Doubling of the parameter Δ_T was suggested also in a recent study devoted to the HgTe/CdHgTe QWs [155]. First, we assume that the density of states at the tails of the Landau levels is very low and, then, analyzing the activation conductivity, we determine the total mobility gap between delocalized states at neighboring Landau levels. Second, our approach takes into account the effect of the random potential for each specific sample via the determination of the parameter Γ . Previous estimations of Γ for the structures with GaAs/AlGaAs QWs yielded small values and, therefore, the region of delocalized states was assumed very narrow. The Γ values determined in this study suggest a need to take into account the Landau-level broadening in MCT-based structures. Let us consider in more detail the choice of the model for describing the density of states at the Landau levels.

As we mentioned above, the density of states is usually described by several models of Landau-level broadening, in particular, the Lorentzian, Gaussian, and semi-elliptical shape. The latter model has nonphysical sharp edges of the density of states, which result from the self-consistent Born approximation. Therefore, this model is not considered below. In the Lorentz model, the Landau-level width Γ_L is independent of the magnetic field. In the Gaussian model of the density of states, the Landau-level width is proportional to $B^{1/2}$ and amounts to

$$\Gamma_G = \sqrt{\hbar^2 \omega_c / 2\pi\tau_q} = \sqrt{\hbar\omega_c \Gamma_L / \pi} \quad \text{Eq. 12}$$

Below, we demonstrate that the Gaussian model describes the best the results obtained for HgTe/CdHgTe QWs. We note that formula given by Eq. 10 suggests the quadratic dependence of the resistance logarithm on the inverse magnetic field for the case of field-independent Gaussian broadening. However, for the Landau-level width (Eq. 12), the dependence in the Dingle plot becomes linear. In view of the aforesaid, the observed linear dependence of the logarithm of $\Delta R_{xx}(1/B)$ corresponds to two cases of Landau level broadening: Lorentzian $\Gamma_L = \text{const}(B)$ and Gaussian $\Gamma_G(B) \sim B^{1/2}$.

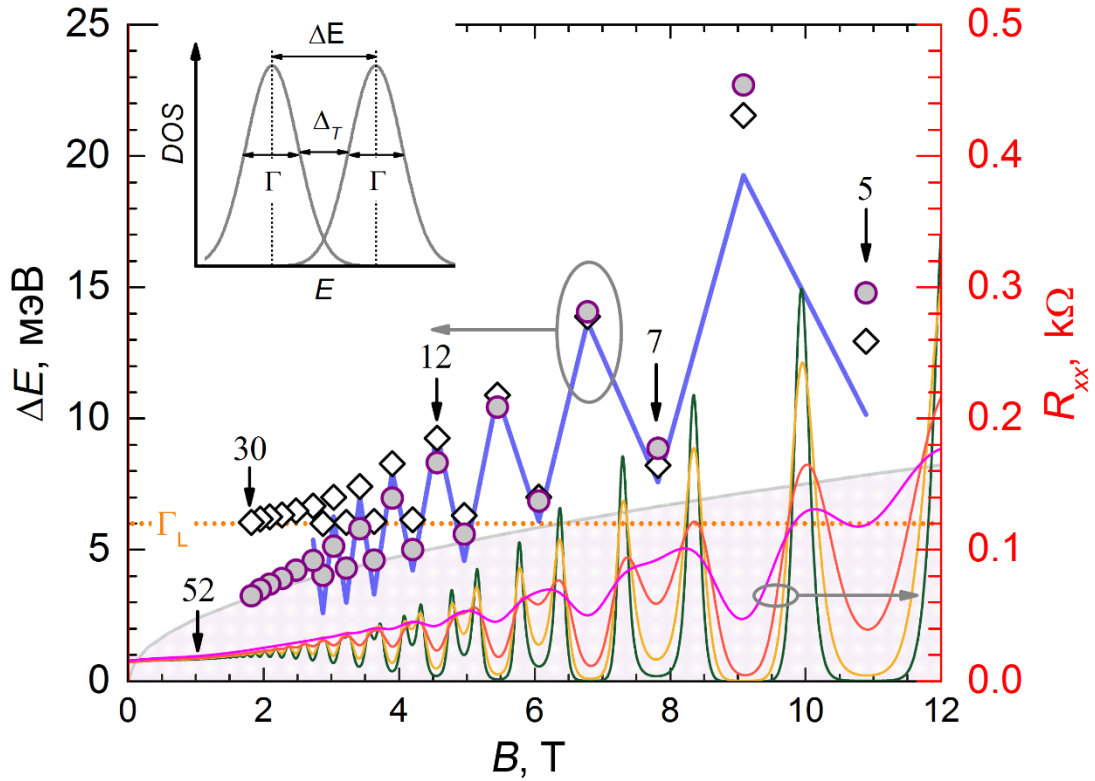


Fig. 32. SdH oscillations in sample 130212 (solid lines; right-hand axis; $T = 1.6, 6.4, 19.2, 38.4$ K) and ΔE values (symbols, left-hand axis) at the integer Landau-level filling factors (shown by vertical arrows). The grey region corresponds to the $\Gamma_G(B)$ dependence and the value $\Gamma_L = 5.8$ meV is shown by the horizontal dotted line. Circles and rhombs show the ΔE values for the Gaussian and Lorentzian models of the density of states at the Landau levels, respectively. The solid broken line connects the gaps between Landau levels calculated using the Kane model for integer ν values. The inset: technique for determining the ΔE value at a finite width of the densities of states of the neighboring Landau levels is illustrated.

Below, when describing the experimental data, we use the model of Gaussian broadening proportional to $B^{1/2}$. Fig. 32 presents the results for sample 130212 with the highest charge-carrier concentration. At low temperatures, a large number of SdH oscillation minima were observed starting from $\nu = 52$ ($B \approx 1$ T) and up to $\nu = 5$ ($B \approx 11$ T). The experimental Δ_T value is shown in Fig. 32 in the implicit form and corresponds to the difference $\Delta E - \Gamma$. It can be seen that the minima of the R_{xx} oscillations are deeper for even filling factors than for odd ones, which is indicative of the fact that the orbital splitting of Landau levels exceeds the spin splitting, as in most of 2D semiconductor systems. Our calculations confirms previous statement as well: the oscillating dependence of the energy gaps ΔE between neighboring

Landau levels at the Fermi level (see Fig. 32). In the experiment, we observe good agreement at $\nu = 7-12$. It can be seen in Fig. 32 that, in this magnetic field range, the determined gaps between the Landau levels in the Lorentz model of level broadening also agree satisfactorily with the calculation. However, in lower magnetic fields (at $\nu > 12$), the Lorentz model, which suggests an invariable Landau-level width, yields nonphysical results. In particular, it predicts the width of the density of states, which multiply exceeds the distances between the Landau levels, while pronounced SdH oscillations are observed up to $\nu = 52$. Thus, the Gaussian model of the density of states is preferred in determining the energy gaps between the Landau levels from magnetotransport measurements.

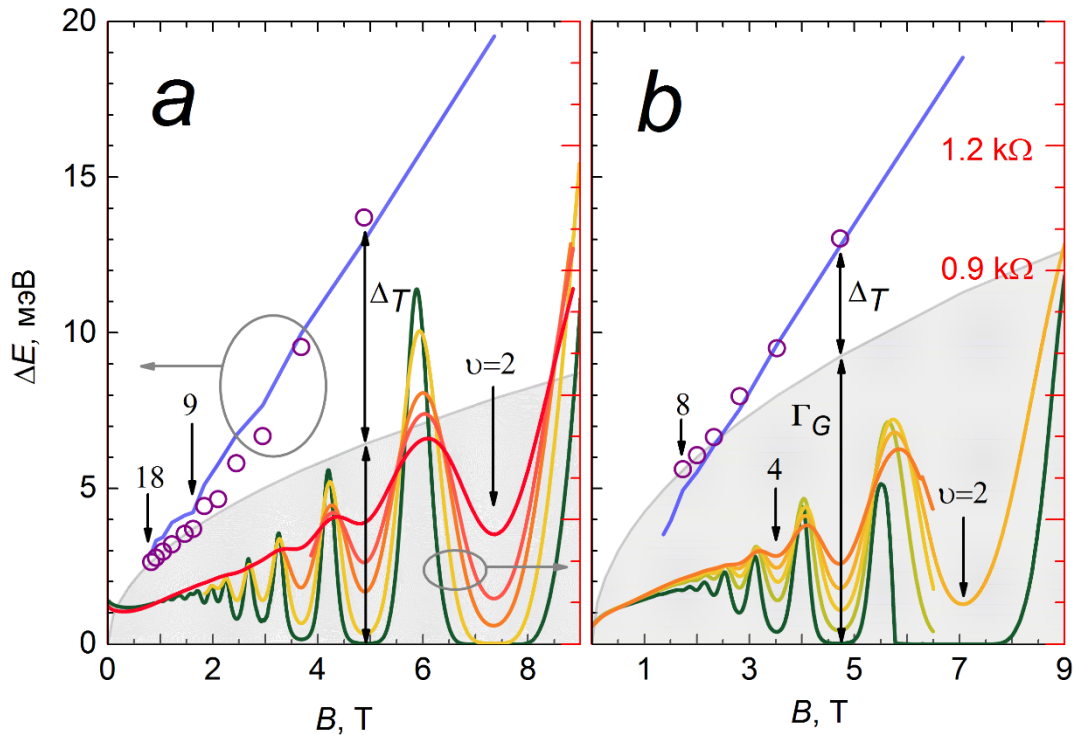


Fig. 33. SdH oscillations in samples (a) 091223* and (b) 091222* (solid lines; right-hand axes; $T = 1.6, 6.4, 12.8, 18,$ and 25.6 K) and ΔE values (circles, left-hand axis) at the integer Landau-level filling factors (some of them are shown by vertical arrows and are marked). The solid grey regions correspond to the $\Gamma_G(B)$ dependences. The solid broken lines connect the gaps between the Landau levels calculated using the Kane model for integer ν values.

Fig. 33 presents the results of determination of the ΔE values for samples 091222* and 091223* with similar charge-carrier concentrations (see Table VIII). The growth parameters of the samples are also similar and only slightly differ in terms of the Cd fractions in the barriers. Therefore, these samples have nearly identical band structures. At the same time, the mobility in sample 091223* ($\mu = 8 \times 10^4$ cm²/(V s)) is significantly higher than in sample 091222* ($\mu = 4.5 \times 10^4$ cm²/(V s)). In the first case, the SdH oscillations are observed starting at $\nu = 18$ in a field of 0.83 T. In the second case, they are observed only starting at $\nu = 10$ in a field of 1.36 T. All this indicates the significantly larger Landau-level broadening in sample 091222*, due to the random potential. Indeed, the analysis using the Lifshitz–Kosevich model yields different parameters Γ_L for these samples: 5.5 meV for sample 091223* and 10.3 meV for sample 091222*. In the first sample, however, the observed activation energies ΔT are significantly higher (see Fig. 33). Therefore, the gaps between neighboring Landau levels at integer filling factors, which are determined as $\Delta E = \Delta T + \Gamma_G$, are almost the same for both samples.

We note that in contrast to sample 130212, where ΔE oscillations are observed (Fig. 32), the distances between the neighboring Landau levels in samples 091223* and 091222* at the same

magnetic fields steadily increase with increasing magnetic field (Fig. 33). This circumstance indicates that the spin splitting for the Landau levels with small numbers is found to be of the same order of magnitude as the orbital splitting.

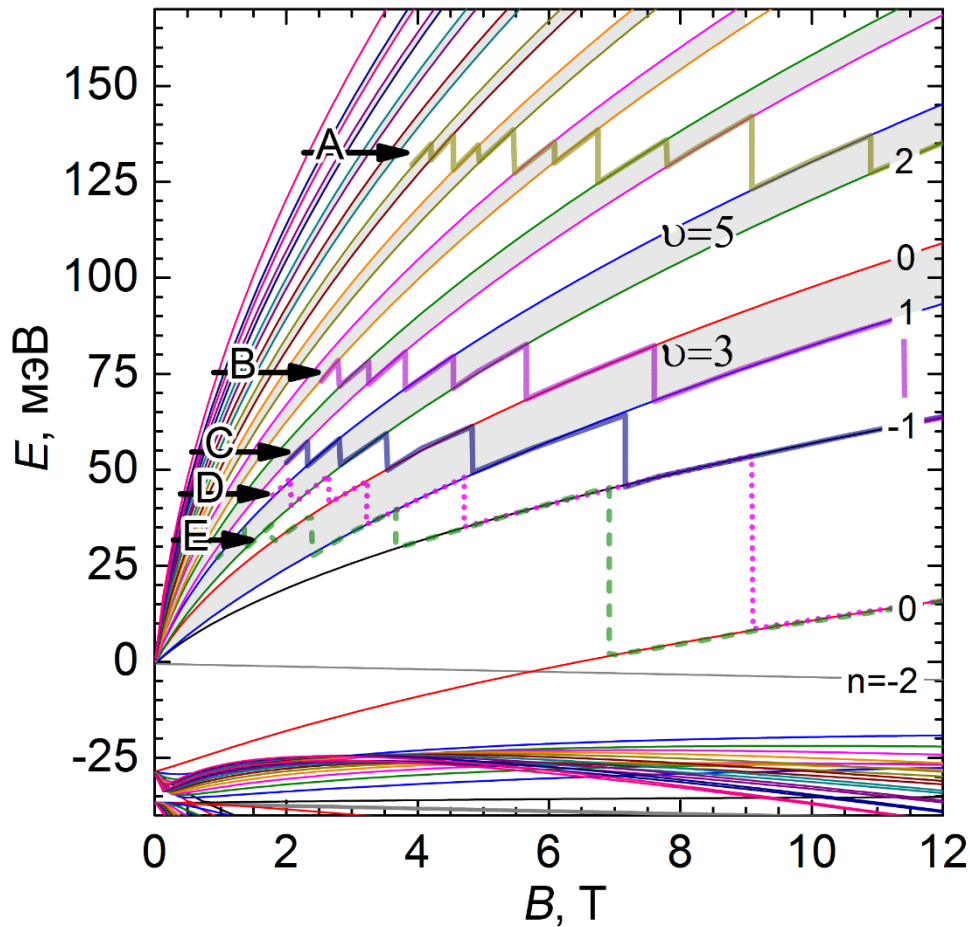


Fig. 34. Landau-level spectrum in the axial Kane model 8×8 for the structural parameters $d_{QW} = \text{nm}$ and $x_b = 0.7$, which corresponds to the sample 091222. The characters correspond to samples 130212 (A), 101109 (B), 091222* and 091223* (C), 091223 (D), and 101221* (E). Spin energy gaps, starting at $\nu = 3$, are colored with grey. The zigzag lines show the Fermi-level positions for the investigated samples. The numbers of some Landau levels are given on the right-hand edge.

5.4. Comparison with the calculated Landau levels

The samples under study have similar growth parameters and, consequently, similar band structures. To make a comparison with the experimental ΔE values, we calculated the Landau-level energies for each sample (a part of the results is presented in Fig. 32 and Fig. 33) in a model developed by V. Ya. Aleshkin. The calculation was performed in the single particle approximation using the 8-band $\mathbf{k}\mathbf{p}$ Kane Hamiltonian with regard to terms describing the effect of elastic strain on the energy spectrum (see, for example, [172]). The Landau levels calculated for sample 091222 are shown in Fig. 34 (the Landau levels for the rest of the samples differ insignificantly).

The band structure of the samples under study is inverted: the lower Landau level in the conduction band is a “hole” level with the number $n = -2$ and the upper level in the valence band is an “electron” level $n = 0$ (compare with [63, 68]), which intersect in a field of $B \approx 6$ T. The broken lines in Fig. 34 schematically show the change in the Fermi level in the investigated

samples with different carrier densities increasing magnetic field (sample 091223* with parameters similar to those of sample 091222* is not shown in Fig. 34). It can be seen that at high Fermi energies, (samples 130212 and 101109) the spin splittings of the Landau levels at even ν values are smaller than the “orbital” splittings at odd ν values. In samples 091222* and 091223, these splittings are similar. In sample 101221* with the lowest electron concentration (and, consequently, the lowest Fermi energy at zero magnetic field), the spin splitting at high magnetic fields becomes larger than the “orbital” splitting. This results from the inverted band structure of the sample.

As it was mentioned when discussing the results for samples 130212, 091223*, and 091222* (Fig. 32 and Fig. 33), the experimental gaps between the neighboring Landau levels agree well with the data calculated in the one-electron approximation using the 8-band $k\cdot p$ Kane Hamiltonian. In addition, we obtained a satisfactory agreement for three other samples investigated in this study. We note that the effect of band structure rearrangement with temperature [65, 116, 173, 174] affects, first of all, the band gap and does not noticeably change the gap ΔE between the neighboring Landau levels in the conduction band, up to the maximum temperature (40 K) used in experiments. This is obviously with the exception for the lower level $n = 0$, which passes to the conduction band after crossing the level $n = -2$. Thus, the obtained experimental data are described well by the one-electron calculations.

It is known, however, that the values of the spin gap in different 2D systems obtained by analyzing the temperature dependence of the SdH oscillation amplitude at odd Landau-level filling factors can significantly differ from the one-electron values due to the exchange interaction between 2D electrons [140, 175, 176]. The theory of spin gap renormalization was proposed first by Ando and Uemura [140] for 2D systems with parabolic dispersion law, in which case the electron effective mass is independent of the density. Later on, the theory of the exchange enhancement of the spin gap was developed also for narrow-gap QWs with the direct-band structure based on III–V semiconductors [175, 176]. The results of calculations of the significantly enhanced “many-body” gap using the Gaussian model to describe the density of states, which were performed for the InGaAs/InP [177] and InAs/AlSb [178-180] QWs, appeared to be in good agreement with the experimental values obtained from the magnetotransport investigations of these structures. We note that the width of the density of states at the Landau levels $\Gamma_G(B)$ in [142, 178-180] was not larger than 1 meV in a magnetic field of 1 T.

The absence of the exchange renormalization of spin splitting at odd values of the filling factors in the investigated samples is related to the much larger Landau-level widths $\Gamma_G(B)$ (see Fig. 32 and Fig. 33) than in other narrow-gap 2D systems [142, 178-180]. The exchange-related renormalization of the spin gap in such systems is determined not only by the degree of spin polarization, but also by the permittivity of 2D electrons, which is responsible for screening of the many-body interaction [140, 175]. Indeed, the permittivity of the 2D electron gas is determined by the density of states of the Landau levels at the Fermi level [175], which increases with $\Gamma_G(B)$ due to the overlap of the “Gaussian” tails of the neighboring spin-split levels. The increase in the overlap of spin-split levels brings about a decrease in the spin polarization and an increase in the permittivity and enhanced screening of the exchange interaction. Thus, due to the large width of the Landau levels in our samples, the exchange renormalization of the spin gap at odd values of the filling factors appears unobserved against the background of large values of “one-electron” spin splitting.

We note that the conclusion (drawn in the previous publication) concerning the influence of exchange effects on spin splitting in 20-nm-wide HgTe/CdHgTe QWs [167] is related to the use of the model of the constant (magnetic field-independent) broadening of Landau levels. Repeated analysis of the experimental data obtained in [167], which is based on using the Gaussian model with the square root magnetic-field dependence of the width of the density of

states (see formula (Eq. 12)), also provides good agreement between the obtained gaps between the Landau levels and the results of “single-electron” calculations using the Kane model.

Finally, it is worth noting that the obtained widths of the density of states at the Landau levels (see Table VIII and Fig. 32 and Fig. 33) noticeably exceed the width of the cyclotron-resonance lines observed in the same samples in both classical and quantizing magnetic fields. In particular, in sample 091223* [23, 27], the width of the cyclotron-resonance line in a field of 2 T is found equal to 2.3 meV, which is almost twice as small as the Γ_G values (2 T) in Fig. 33(a). This can be indicative of a more complex shape (significantly different from Gaussian one) of the density of states at the Landau levels, when there is a narrower “resonance” part, which determines the observed width of the cyclotron- resonance line, against the background of a wide contour.

The results obtained were described using the Gaussian model of the density of states at the Landau levels with the square root magnetic-field dependence of the width. The experimental gaps between the Landau levels agree well with the results of single-electron calculation of the level energy using the 8-band Kane model. The experimental widths of the density of states are indicative of the pronounced screening of the exchange interaction in our samples.

Chapter 6. Exploring magneto-optical properties of double quantum wells HgTe/CdHgTe

As noted in the Introduction, a single HgTe/CdHgTe QW can be in different phase states. As the width of the quantum well increases, its band structure is rearranged from the normal (corresponding to the state of a trivial insulator) to the inverted (corresponding to the 2D state of a topological insulator). The magnetoabsorption spectra in double HgTe/CdHgTe quantum wells (QWs) with normal and inverted band structures are investigated in this chapter. The Landau levels in symmetric QWs with a rectangular potential profile are calculated based on the Kane 8×8 model [67]. The presence of a tunnel-transparent barrier is shown to lead to the splitting of states and “doubling” of the main magnetoabsorption lines. We observe the band inversion and the emergence of a gapless band structure, similar to bilayer graphene, in the two coupled QW with critical width d_c . The visible shift of magnetoabsorption lines is detected as the carrier concentration changes. Latter happens due to the persistent photoconductivity effect associated with an alteration of potential profile because of trap charge exchange. This opens up the possibility for controlling topological phase transitions in such structures externally.

- Bovkun, L.S., et al., Magnetospectroscopy of double HgTe/CdHgTe quantum wells. *Semiconductors*, 2016. 50(11): p. 1532-1538.

6.1. Experimental details

The investigated samples were grown by molecular beam epitaxy with ellipsometric control of the layer composition and thickness on semi-insulating GaAs (013) substrates [14]. The “active part” of the structure was grown on a thick relaxed CdTe buffer layer and consisted of a lower $\text{Hg}_{1-x}\text{Cd}_x\text{Te}$ barrier layer with a thickness of 30 nm, two HgTe QWs of width d_{QW} separated by a tunnel transparent $\text{Hg}_{1-x}\text{Cd}_x\text{Te}$ barrier of thickness t bar, and an upper $\text{Hg}_{1-x}\text{Cd}_x\text{Te}$ barrier with a thickness of 30 nm. A 40-nm-thick coating CdTe layer was grown atop. The structures were not intentionally doped. The structure growth parameters are given in the Table IX. They were chosen in such a way that sample 150217 had a normal band structure, while sample 150218 corresponded to the “bilayer graphene” phase. The “amended” parameters obtained from the condition for best agreement between the observed and calculated energies of magneto-optical transitions are given in parentheses. The composition of sample 150218 is schematically shown in Fig. 35.

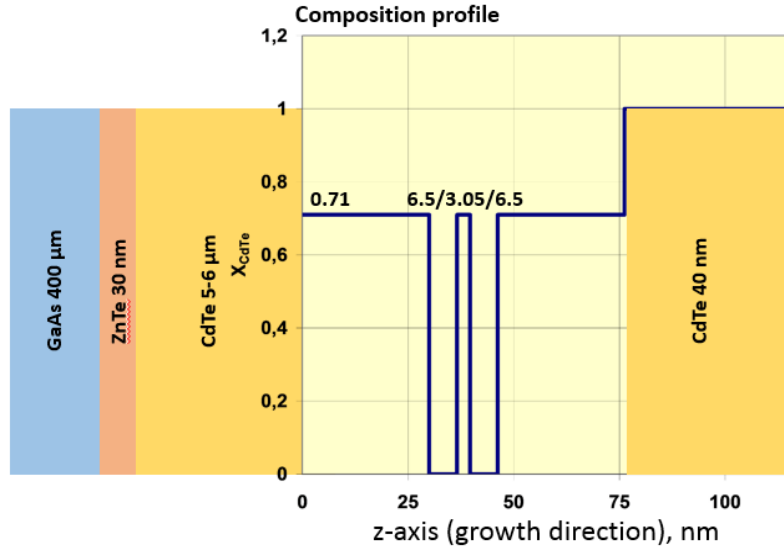


Fig. 35. From left to right – layer by layer deposition of heterostructure 150218. Composition profile of “active part” is shown with solid line, where two rectangular quantum wells are present clearly.

Table IX. Parameters of the investigated samples

Sample #	x	d_{QW} , nm	t_{bar} , nm	p_s , 10^{11} cm^{-2}
150217	0.64	4.5 (3.8)	3 (3.7)	0.5
150218	0.71	6.5 (6.3)	3 (2.8)	1.3

The magnetoabsorption spectra were measured in the Laboratoire National des Champs Magnetiques Intenses in Grenoble (France), the Laboratoire Charles Coulomb of the Centre National de la Recherche Scientifique and the Universite de Montpellier by means of Fourier spectroscopy with a resolution of 4–8 cm^{-1} at a temperature of $T = 4.2$ K in magnetic fields up to 15 T in the Faraday geometry on 5×5-mm samples. Global or a mercury lamp used as source of emission, while the composite silicon bolometer as a detector. The measured transmission spectra were normalized to the transmission spectrum in zero magnetic field. The charge-carrier concentration could change under short time (through the persistent photoconductivity effect) or continuous illumination of the sample by a blue light-emitting diode located in liquid helium near the sample. Four indium point contacts were located in the sample corners to determine the concentration by the van der Pauw method. Typical values of mobility at low temperature are $5 \times 10^4 \text{ cm}^2/\text{V s}$.

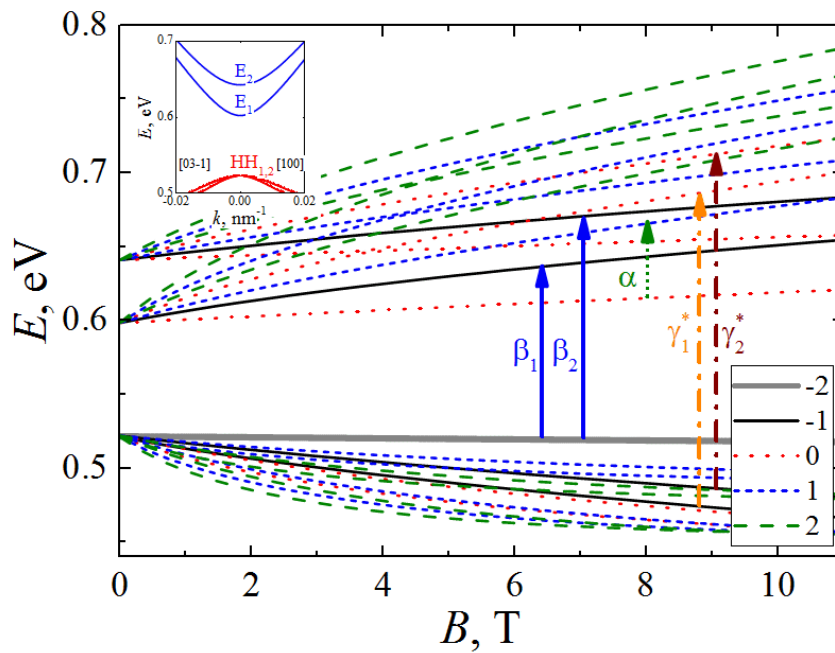


Fig. 36. Calculated Landau levels in the 150217 heterostructure with a double HgTe QW. The arrows indicate the observed magneto-optical transitions. The inset presents the calculated band structure of the sample in the absence of magnetic field.

6.2. «Doubling» of dominant absorption lines in spectra

The dispersion law (calculated by S. S. Krishtopenko) is shown as inset in Fig. 36 for two lower electron subbands (E_1 , E_2) and two upper hole subbands (HH_1 , HH_2) for sample 150217 with a normal band structure. It can be seen that the barrier is tunnel-transparent for the electron states (the E_1 and E_2 subbands are split), while the HH_1 and HH_2 subbands are degenerate at $\mathbf{k} = 0$. The Landau levels calculated in the axial approximation for this sample are presented in Fig. 36. The subband splitting in the conduction band is seen to give rise to two identical fans of Landau levels. In the valence band, where there was no splitting at $\mathbf{k} = 0$, applying a magnetic field leads to slight splitting of the hole Landau levels except the $n = -2$ level, which remains “doubly” degenerate (in terms of the number of QWs).

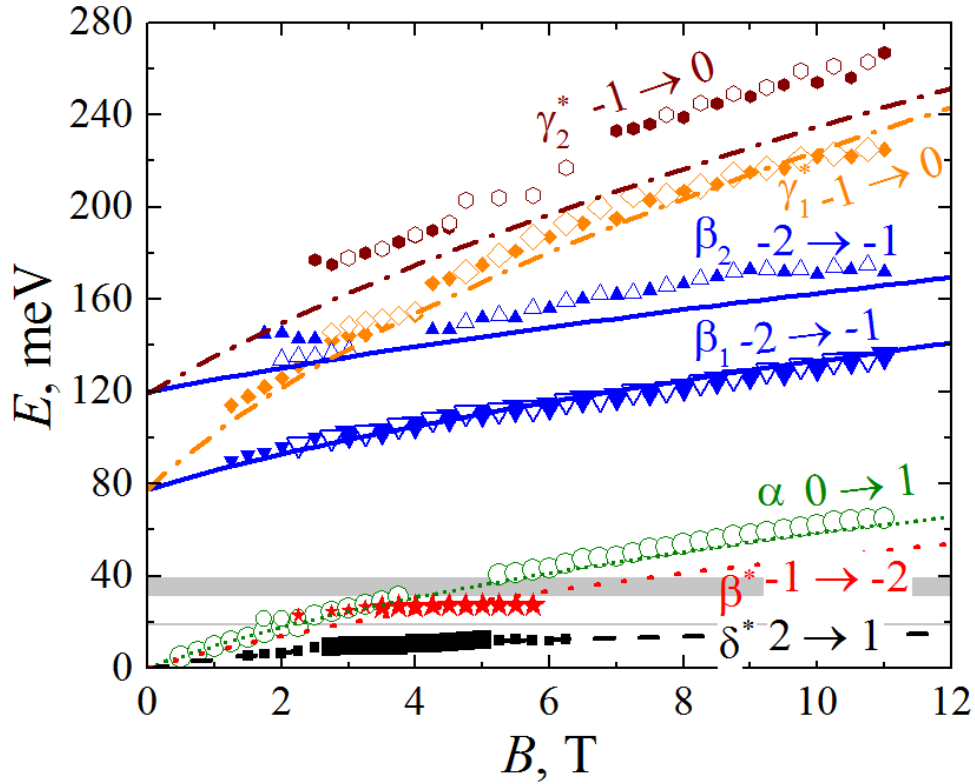


Fig. 38. Calculated (lines) and measured (dots) positions of the magnetoabsorption lines as a function of the magnetic field in the 150217 heterostructure. The filled and open symbols correspond to dark conditions and illumination by a blue light-emitting diode, respectively; the sizes of the symbols indicate the absorption-line intensity.

As already noted, under illumination the p -type conductivity of the sample 150217 changes to n -type, and the absorption α line appears in the spectra. Since the Landau-level filling factor $\nu < 1$ in this case beginning already at field as low as $B \sim 2$ T, this line, obviously, is associated with the $0 \rightarrow 1$ transition from the lower Landau level of the conduction band. In weaker magnetic fields, when the next Landau level begins to fill, the lower-frequency $-1 \rightarrow 0$ transition should be observed. However, the sensitivity of the setup drops in this frequency range, and the transition cannot be distinguished against the noise background. As can be seen from Fig. 38, the field dependence of this transition energy on the magnetic field calculated for “amended” parameters of the structure, in general, is consistent with experimental data, although a systematic overestimates of the observed transition energies over the calculated ones is obvious. We note that the observed width of the δ^* , β^* , and α lines associated with transitions between Landau levels belonging to the same subband (Fig. 37) is several times smaller than the characteristic width of the interband-transition lines discussed below. This is most likely attributable to fluctuations in the QW width (over the area of the structure) causing the corresponding fluctuations of the band gap.

Let us now analyze the magnetoabsorption spectra at high frequencies. It is natural to associate the most intense β_1 absorption line, which is observed both under dark conditions and under illumination, with the interband $-2 \rightarrow -1$ transition from the upper Landau level of the valence band to the $n = -1$ level belonging to the E1 subband. This transition must also be observed under dark conditions (in the sample with p -type conductivity) starting from fields corresponding to the filling factor of the hole Landau levels $\nu = 2$ (due to the “double”

degeneracy of the $n = -2$ level), i.e., from $B \sim 1$ T, which corresponds to the observed pattern (Fig. 38). Linear extrapolation of the position of this line to zero magnetic field gives a band gap of $\Delta E \sim 80$ meV, which was used as an input parameter of our calculation of the band spectra. The second such quantity was the splitting of the E1 and E2 subbands, $\Delta E \sim 40$ meV, which was determined from linear extrapolation to zero magnetic field of the β_2 line that we associate with the transition from the $n = -2$ level to the $n = -1$ level belonging to the E2 subband. Our calculations of the interband transition probabilities show that the intensities of the β_1 and β_2 absorption lines must exceed those of other interband transition lines several-times. The intensity of the β_1 line must be by a factor of 1.5 – 2 higher than that of the β_2 line. However, as can be seen from the spectra presented in Fig. 37, the observed intensity ratio is appreciably larger, by a factor of 3 – 4. Such a discrepancy can be caused by slight $n = -2$ level splitting due to a difference in the thicknesses of the nominally identical QWs, as a result of which the population of the upper level turns out to be smaller, leading to a decrease in the intensity of the β_2 absorption line. We note that the $1 \rightarrow 0$ transitions from the upper pair of $n = 1$ Landau levels in the valence band to the lower pair of $n = 0$ Landau levels in the conduction band also have close (to the $-2 \rightarrow -1$ transitions) energies. As our numerical calculations show, out of the four such possible transitions, only the lower-to-lower and upper-to-upper Landau level transitions are allowed. Their probabilities turn out to be lower by almost an order of magnitude than probabilities for the $-2 \rightarrow -1$ transitions.

At even greater photon energies, the spectra contain fairly weak interband transitions designated as γ^*_1 and γ^*_2 (see Fig. 37 and Fig. 38). We associate these lines with the transitions from the pair of $n = -1$ Landau levels in the valence band to the second pair of $n = 0$ Landau levels in the conduction band (the lower-to-lower and upper-to-upper transitions again turn out to be the allowed ones). Our assumption is based on the observed B -dependences of the resonance energies and the calculated transition probabilities (the interband-transition probabilities decrease with increasing numbers of the “involved” Landau levels),

It can be seen from Fig. 38 that, just as for α line, our calculation for the interband transitions (β_2 , γ^*_1 and γ^*_2) gives a slightly underestimated slope of the B -dependence of the line. This discrepancy cannot be removed completely by varying the structure parameters of the investigated sample within reasonable limits (compared to the growth data). Similar discrepancies were also observed previously for single HgTe/CdHgTe QWs [23, 28]. These discrepancies are most likely attributable both to the imperfectness of the axial model of the dispersion law used (which disregards symmetry-reduction effects associated with the absence of a crystal-lattice inversion center and the mixing of hole states at the heterointerfaces) and to inaccuracy in determining the material parameters of the HgTe/CdTe heterostructures used in our calculations. Additional studies of simple model structures, to which double QWs obviously cannot be attributed, are required to solve these problems. The main result of our study of a double QW with a normal band structure (the 150217 sample) is the observation of a doubling of the interband-transition lines suggesting the implementation of a tunnel-transparent barrier and the splitting of states in the conduction band.

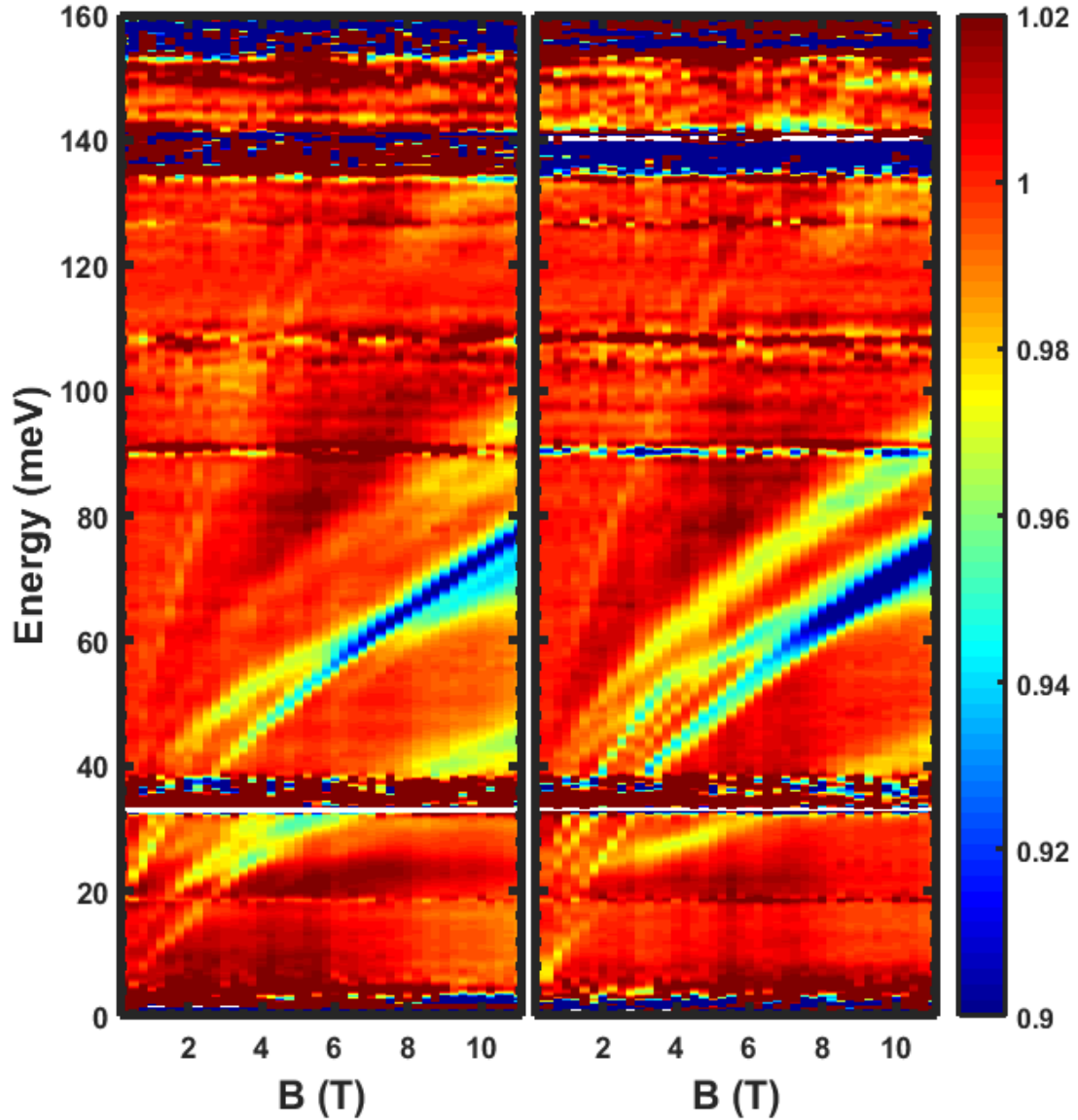


Fig. 39. Transmittance versus the frequency and magnetic fields for the sample 150218 in the absence of illumination (left) and at maximal illumination (right).

False-color maps obtained on the second heterostructure 150218 are shown in Fig. 39. This sample has p -type conductivity at all illumination levels; the hole concentration decreases from $p \approx 1.5 \times 10^{11} \text{ cm}^{-2}$ under dark conditions to $p \sim 2 \times 10^{10} \text{ cm}^{-2}$ under long term (or continuous) illumination by a blue light emitting diode. Therefore, transitions between hole Landau levels and interband transitions can be observed in this sample. As one can see from “raw” data in Fig. 39, there are many absorption features in magneto-optical response of the sample, i.e. both interband and intraband transition, with different slopes and intensities. There is a clear distinction in responses before and after illumination. Above-mentioned effects discussed below in the text, after short excursus into band structure calculations.

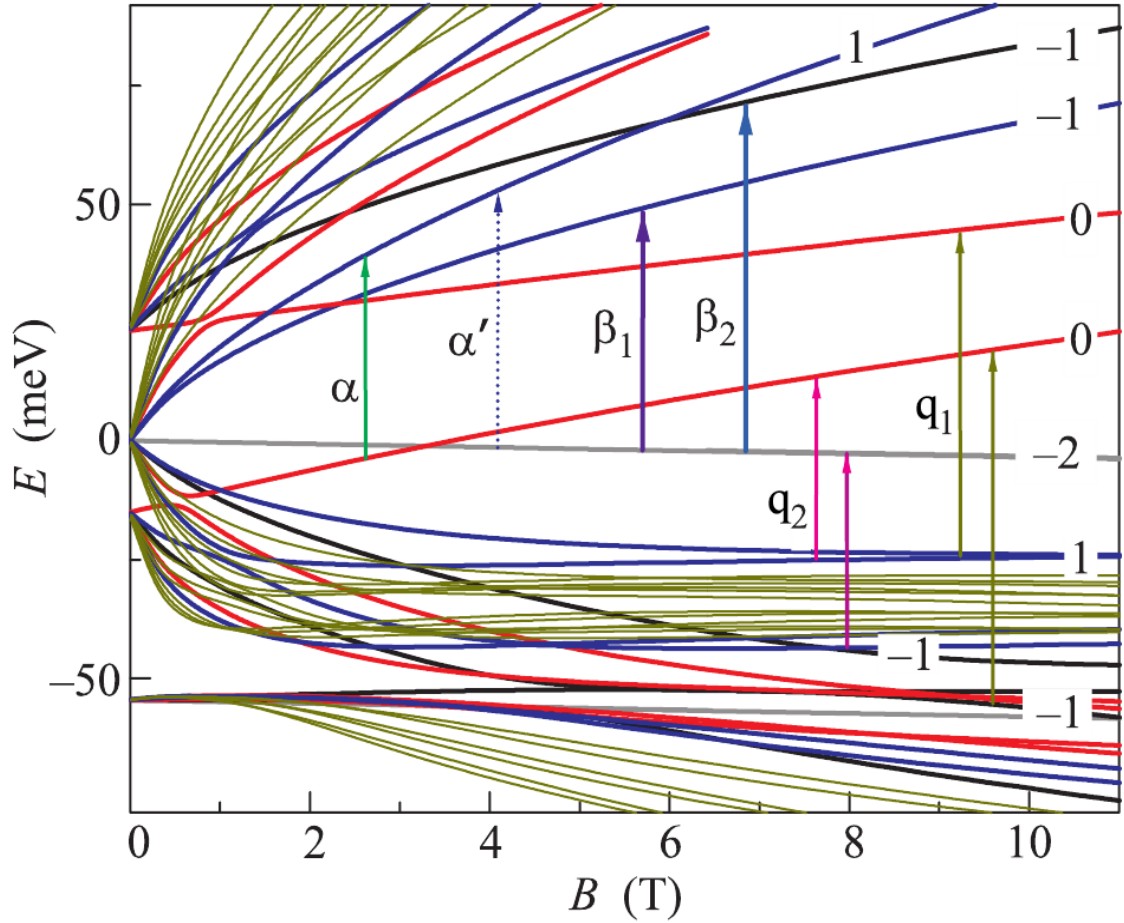


Fig. 40. Calculated Landau levels in the 150218 heterostructure with a double HgTe QW. The arrows indicate the allowed magneto-optical transitions.

The thickness of each of the QWs is close to the critical one (i.e. $d_c = 6.4$ nm for a single QW), but the band spectrum becomes inverted due to the tunnel-transparent (for electron states) separating barrier. The E1 and HH1 subbands are inverted in this sample. As a result, a gapless band structure formed by the “parabolic” HH1 and HH2 subbands touching at point $\mathbf{k} = 0$ emerges, just as in bilayer graphene [67]. The degeneracy of the HH1 and HH2 subbands at $\mathbf{k} = 0$ is related to the opacity of the separating barrier for hole-like states. Landau levels for this sample calculated in the axial approximation are presented in Fig. 40. It can be seen that, as in the 150217 sample, the number of Landau levels with identical numbers (the $n = -2$ level remains doubly degenerate) increases by a factor of two in this DQW. However, the inversion of the E1 and HH1 subbands manifests itself in the fact that the lower of the $n = 0$ levels crosses the $n = -2$ levels at particular field $B_c \approx 4.6$ T and, thus, begins to belong to the valence band (accordingly, one of the $n = -2$ levels below B_c belongs to the conduction band). Note that above-mentioned $n = 0$ Landau level belongs to the conduction band in the sample 150217 with normal band structure.

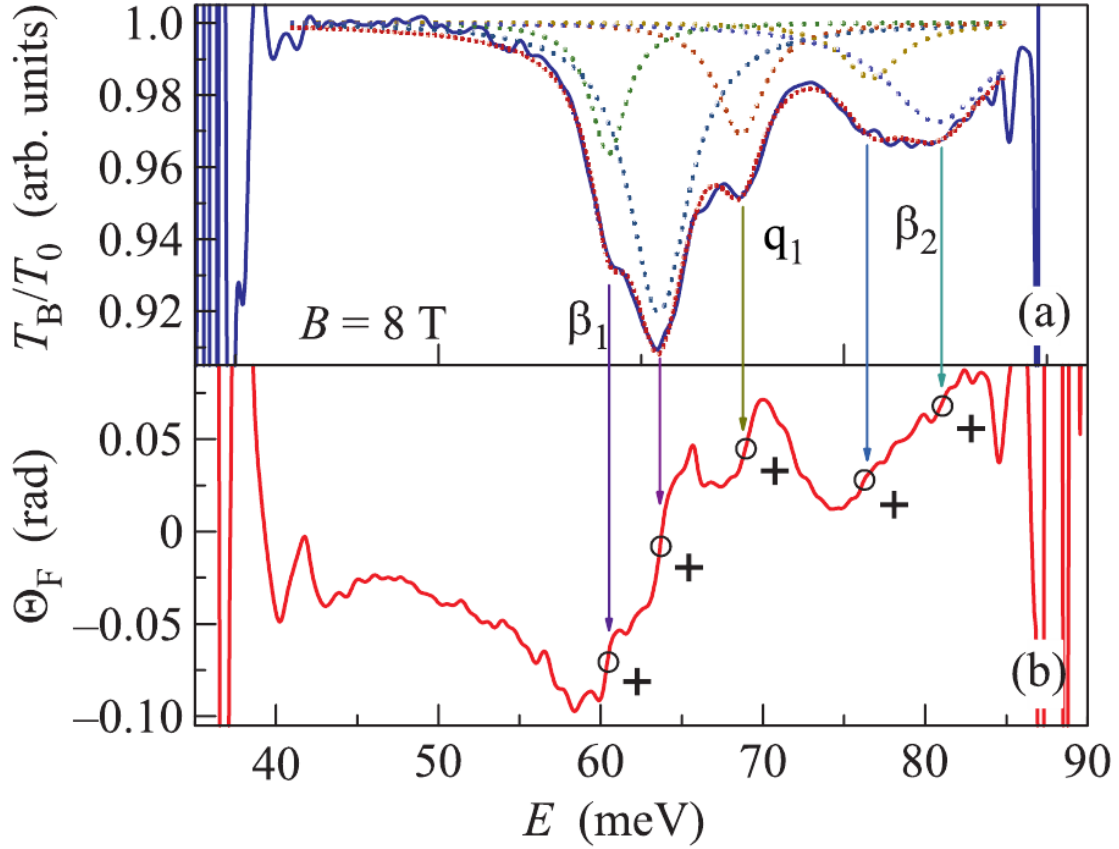


Fig. 41. Transmittance (a) and Faraday rotation (b) spectra in sample 150218 for a fixed $B = 8$ T. For each feature in spectrum (a) there is a characteristic sign of the slope in spectrum (b) corresponding to hole-like (+) transition type. Compare with Fig. 16.

Our first attempt of identification absorption features in the sample 150218 reported in [183] and though it was rather correct, we perform additional polarization-sensitive experiment provided additional information. Fig. 41 presents the result of transmittance and Faraday rotation, where for each observed feature in the top spectrum there is a corresponding slope in the bottom spectrum. For a given spectra, we observe only hole-like transitions, corresponding to a change in the number of the Landau level $\Delta n = +1$ and positive derivatives in the spectrum of the Faraday rotation. The shape of β_2 absorption line of clearly indicates presence of several peaks. Therefore, the magnetoabsorption spectra were decomposed to a set of Lorentzian functions, thus not only the position of each peak, but also its width and area of each line can be extracted. The results of a detailed analysis of the magnetoabsorption spectra for different B are shown in Fig. 42. Each circle corresponds to an absorption peak, whilst the symbol size is proportional to the area of the fitted peak. The sign of the derivative in the spectrum of Faraday rotation depicted in overlay with "+", "0", or "-" sign for particular absorption lines. The solid lines in Fig. 42 show the transitions calculated in the framework of the axial approximation. The best agreement between the experimental and theoretical data was achieved with a slight decrease in the thicknesses of both quantum wells to 6.3 nm. There are two β_1 and β_2 strongest lines in the magnetoabsorption spectra, which correspond to the known transition $-2 \rightarrow -1$ (Fig. 40). It is the transparency of the barrier between two quantum wells that explains interaction of two identical levels -1 and, in turn, the appearance of two transitions from $n = -2$ to bonding $n = -1$ and anti-bonding $n = -1$ states both unoccupied in conduction band. These transitions occur with an *increase* in the Landau level number by one in the entire range of B , which is observed in the spectra of the Faraday rotation.

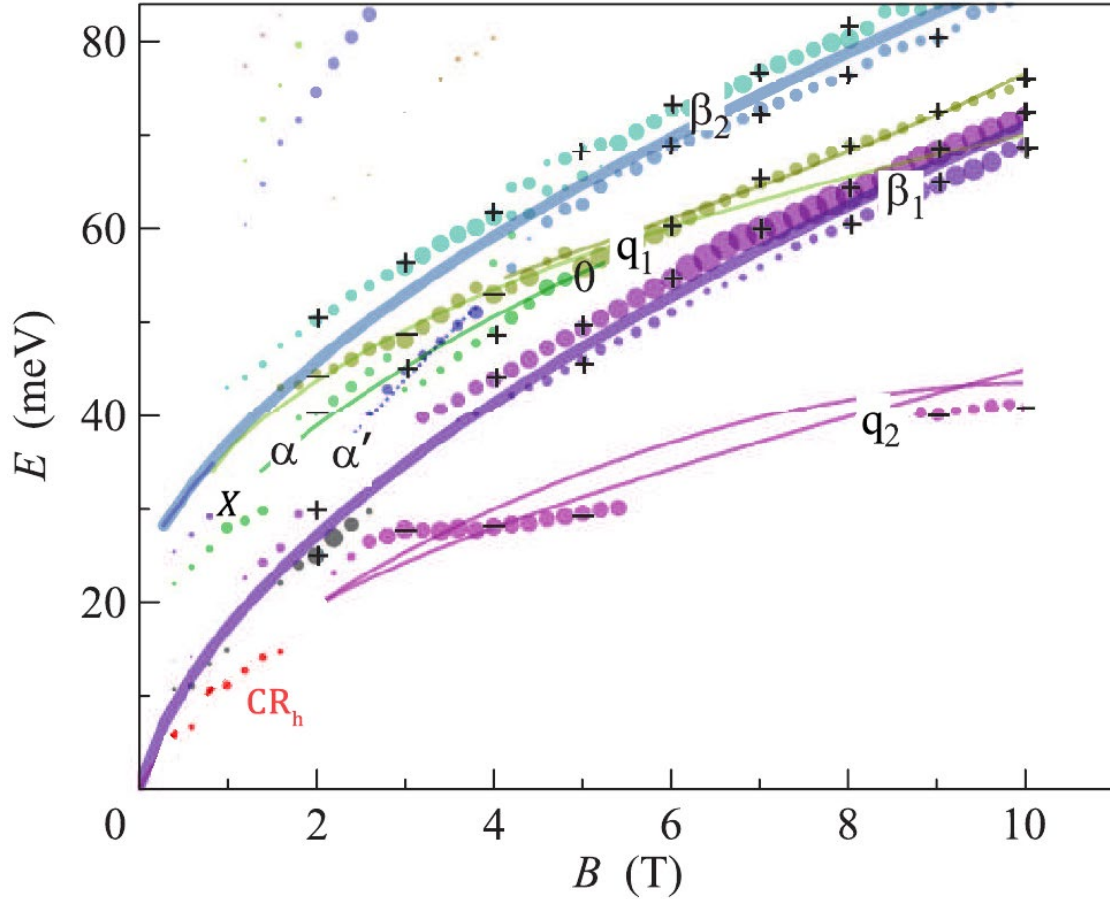


Fig. 42. Calculated (lines) and measured (dots) positions of the magnetoabsorption lines as a function of magnetic field in the 150218 heterostructure. The area of the symbols is proportional to the area of the magnetoabsorption feature; the thickness of the lines is proportional to the transitions' probabilities. Sign of the derivative $d\Theta/dE$ is represented by symbols '+', '-', or '0' in corresponding regions.

A much wider line q_2 , lying in the energy range 30–40 meV, corresponds to two transitions: interband $1 \rightarrow 0$ and intraband $1 \rightarrow -2$ (see Fig. 40). Both these transitions occur with a *decrease* in the Landau level number by one, i.e. the negative derivative in the spectra of the Faraday rotation. Finally, the q_1 line, observed between the lines β_1 and β_2 (Fig. 42), presumably has a more complex nature than was assumed in [183]. It corresponds to a negative derivative of Faraday rotation at low fields $2 < B < 4.5$, where its position is well described by the transition $1 \rightarrow 0$ (Fig. 40) in the same way as was assumed in [183]. However, with a further increase of B up to 5.5 T, the sign of the derivative is not surely determined (the derivative in the Faraday rotation spectra is close to zero), and for even larger fields the sign of the derivative becomes positive (see Fig. 41(b)). Such behavior may indicate the “crossover” between different transitions. Indeed, the transition $-1 \rightarrow 0$ with $\Delta n = +1$ turns out to be close in energy at $B > 4$ T. In the crossover region 4.5–5.5 T, both the $1 \rightarrow 0$ and $-1 \rightarrow 0$ transitions (Fig. 40) are active and starting from 5.5 T, the main contribution to the line q_1 is given by the hole-like (+) transition.

An entire group of lines is observed at 3–4 T just below q_1 line (see Fig. 42). Exactly the same region correspond to the theoretical prediction (see Fig. 40) for intersection of zero-mode LLs $n = 0$ and $n = -2$ (compare with [26, 63, 68]). Latter works actually demonstrate not an intersection but avoiding crossing, thus axially forbidden α' transition $-2 \rightarrow 1$ is observed in vicinity of B_c [63, 68]. It is most likely that observed group of lines is associated with the manifestation of this anticrossing (i.e., the contributions will be $0 \rightarrow 1$ (α) and $-2 \rightarrow 1$ (α')).

Moreover, an additional "entanglement" introduces a splitting of the level $n = -2$ (discussed in the following section), which should lead to double anticrossing. Since the splitting of the $n = -2$ level is relatively small (~ 4 meV), it is not possible to study in detail the manifestations of double anticrossing in these measurements in this sample within our experimental data.

6.3. Splitting of $n = -2$ Landau levels in heterostructures with inverted band

Analysis of data obtained at $B < 14$ T from the previous section does not allow complete identification of the absorption lines, due to (i) the complexity of the energy spectrum of the valence band, (ii) a large number of possible transitions, and (iii) the non-obvious influence of illumination (not only the change in concentration, but also the change in the profile of the potential). One of solutions to the above problems is to carry out an experiment in magnetic fields up to 30 T, where the quantum limit is presumably achieved in the samples under study, with all carriers at the upper Landau level of the valence band. Moreover, as the magnetic field increases, the cyclotron and spin splittings increase, the difference in the energy of the transitions between different Landau levels increases, and the identification of the absorption lines becomes much simpler.

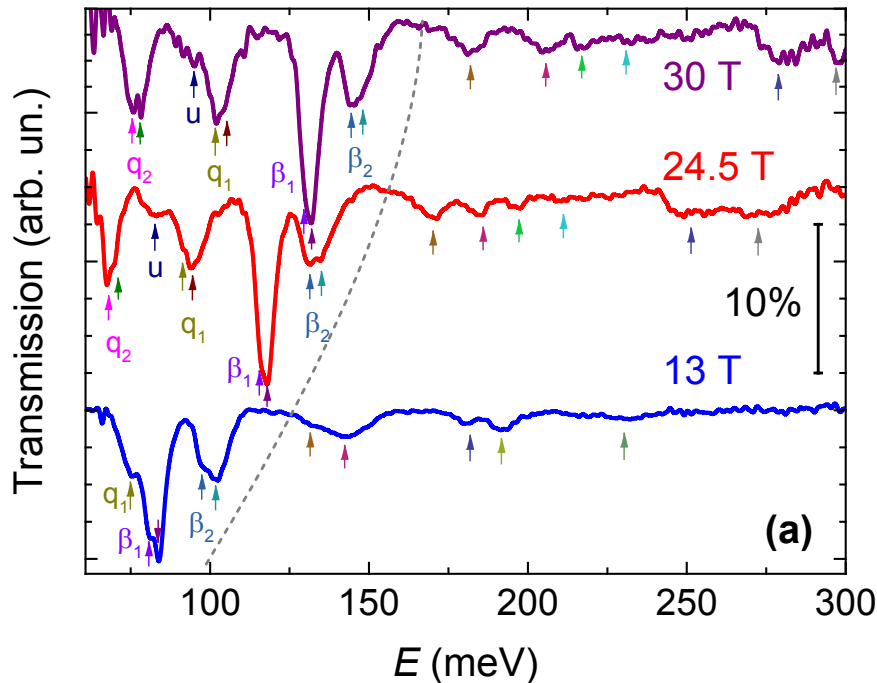


Fig. 43. Typical magnetoabsorption spectra in sample 150218, measured in different magnetic fields. The arrows indicate the observed spectral features. The dotted line denotes the symbolic boundary between low-frequency and high-frequency lines.

Fig. 43 shows typical magnetoabsorption spectra measured in the sample 150218. We fit each spectrum with multiple peaks and determined the position, the width and the area of each spectral feature. To distinguish between a weak absorption line and a noise we analyze each spectrum independently and take into account only the lines that exist in several successive spectra and which positions shift with magnetic field.

The results of this analysis are shown on Fig. 44. Each symbol corresponds to one peak in the magnetoabsorption spectra. The symbol area is proportional to the integral intensity of a peak; the error bar represents the peak's half width at half maximum. One can see that the results of the measurements in moderate magnetic fields up to 11 T and in high magnetic fields up to 30 T coincide well. Some discrepancies are most likely associated with a slight differences in band structure and hole density in samples. In fact, we studied different fragments of the same heterostructure in mentioned experiments.

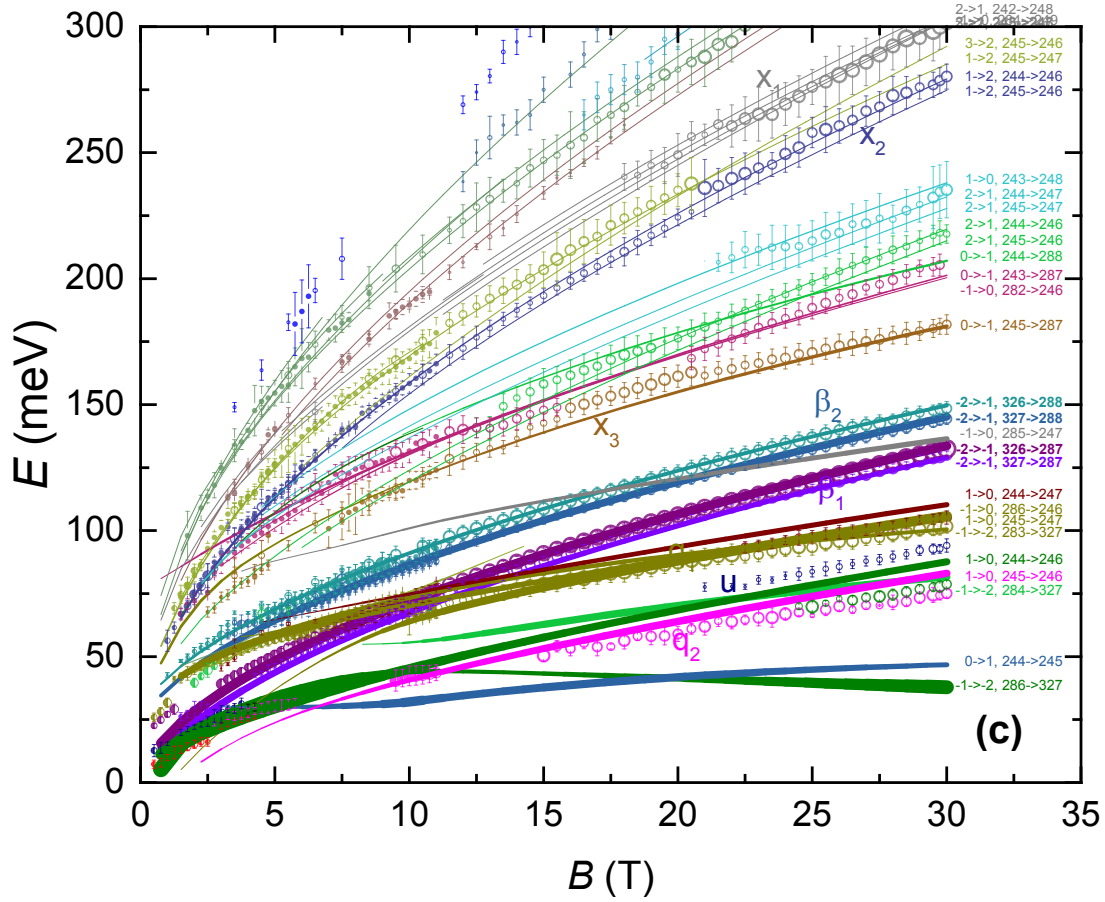


Fig. 44. The positions of magnetoabsorption lines versus magnetic field. Open symbols correspond to the measurements in the magnetic fields up to 30 T, solid and half-filled symbols correspond to the measurements in fields up to 11 T. Error bars show the peaks' half width at half maximum. The area of the symbols is proportional to the area of the magnetoabsorption feature. Lines represent calculated energy of possible transitions for sample 150218 taking into account the electric field of $E = 5$ kV/cm. The thickness of the lines is proportional to the transitions' probabilities.

In Fig. 44, one can distinguish two main areas divided by 100–150 meV gap: (i) the region of low-frequency narrow lines, in which there are all the main and most intense transitions, and (ii) the region of wider high-frequency lines (everything higher than line x_3 in Fig. 44). We note that the intensities of the lines (ii) strongly depend on the “baseline” of the spectrum (see Fig. 43), so one should not compare directly the areas of high-frequency (ii) and low frequency lines (i).

To identify the magnetoabsorption lines we calculate the LL energies, wave functions, and the probabilities of the optical transitions between LL for the unpolarized radiation in all range of magnetic field. Thanks to the theoretical model developed by V. Ya. Aleshkin, authors we able to calculate the LL spectrum by the diagonalization of the 8×8 $k \cdot p$ Hamiltonian for (013) - oriented heterostructures [23, 27], We used an axial approximation, neglecting both BIA and IIA effects, since their influence is insignificant in moderate and high fields discussed below. To achieve the best agreement between calculations and experimental data we slightly adjusted the parameters of our structures (see Table IX). The result of the LLs calculation is shown on Fig. 45. Each level is characterized by the LL index n ($n = -2, -1, 0, 1 \dots$). The second number enumerates LLs in our calculations. It arises when the finite-dimensional matrix is diagonalized (in this case, 8×41). This number has no particular physical meaning; however, a pair of these numbers uniquely identifies a specific LL (e.g. Fig. 45 and Fig. 44).

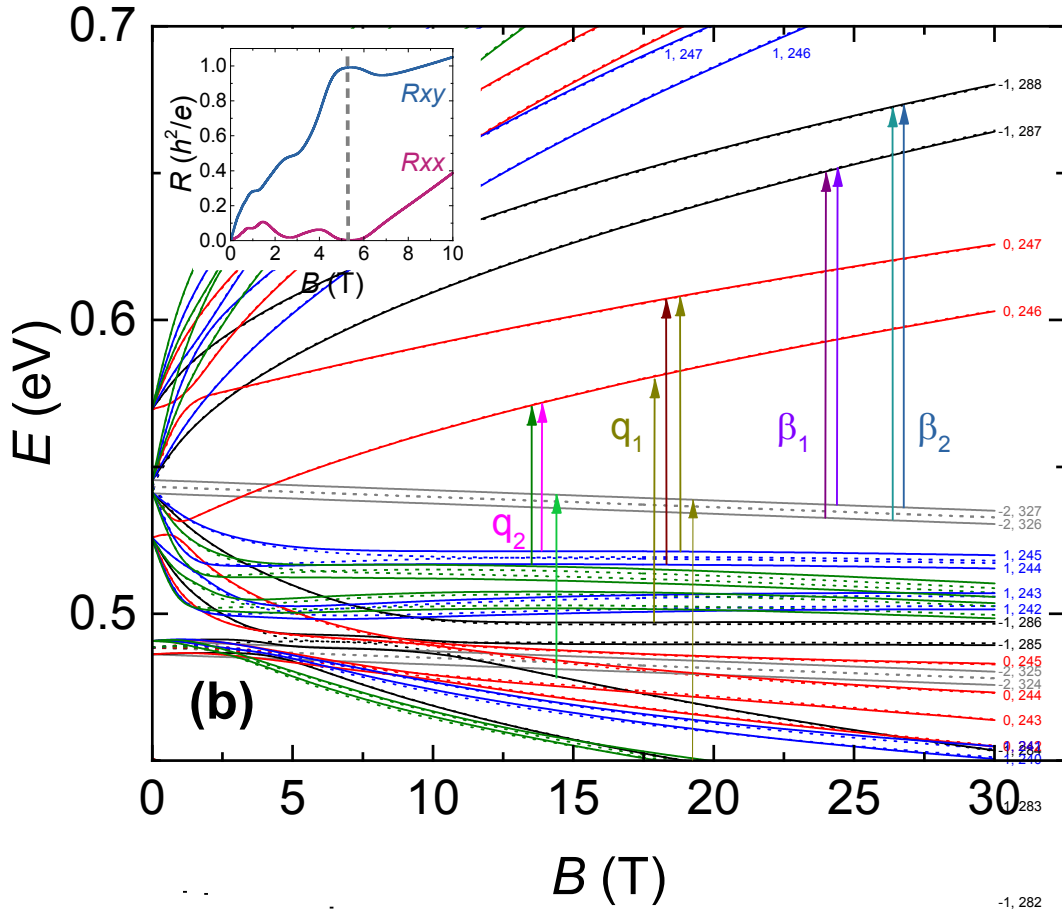


Fig. 45. Calculated LLs in sample 150218 taking into account the electric field of $E = 5$ kV/cm (solid lines) and $E = 0$ (dotted lines). The arrows indicate some observable transitions. Numbers denote a concrete LL. The Fermi level in high magnetic fields is situated on level $n = -2, 327$. Inset shows the magnetotransport data, the dashed line indicates a value of the magnetic field in which the filling factor is unity.

Let us make a small digression now and consider the position of the Fermi level. Despite the fact that magnetotransport experiments in HgTe DQW revealed an unusual structure of the quantum Hall effect [184, 185] we can claim that even for the maximum hole concentration in our samples under dark conditions, the LL filling factor ν is less than unity for the magnetic fields above 6 T (see inset on Fig. 45). This means that the Fermi level is placed at the upper Landau level $-2, 327$ (Fig. 45). In turn, this means that in the high fields we can observe either interband transitions, or transitions from or to the above-mentioned LL $n = -2$ since all other transitions are not allowed due to occupation effect [23, 63, 68]. For the same reason, in this chapter we only consider transitions in high magnetic fields, since their interpretation is not tangled by the filling factor change and the zero-mode LLs crossing.

We start the discussion from consideration of the high-frequency lines. We calculated energies and the probabilities of the optical transitions between pairs of LLs, which satisfied the selection rules for electric-dipole excitations $\Delta n = \pm 1$. In Fig. 44 we show *all the transitions* which have any significant probabilities. One can see that for almost all possible transitions the corresponding lines are observed. Some lines correspond to multiple transitions (for example, the x_1 line, Fig. 44). Some transitions merge into one line only in a certain range of fields (lines x_2 & x_3). Anyway, one can see that there is a very good agreement between the position of the observed spectral features and the calculated transitions. All high-frequency lines correspond to interband transitions from the valence band to the conduction band. The width of these lines is determined by the non-homogeneity of the sample, which primarily affect the band-gap, and

the difference in the energies of the transitions that ‘compose’ a particular line. The notation for the specific transitions corresponding to a particular line in the spectra is shown in Fig. 44.

The low-frequency lines in high magnetic fields are represented by five lines: β_1 , β_2 , q_1 , q_2 and u (Fig. 44). The lines β_1 and β_2 correspond to well-known $-2 \rightarrow -1$ transitions from one of the zero-mode LL $n = -2$ to LL $n = -1$ in a conduction band [23, 26, 63, 68]. In a DQW system, the presence of a tunnel-transparent barrier leads to interaction of states in different QWs resulting in doubling of the LLs [67]. That is why we have two $-2 \rightarrow -1$ transitions (β_1 and β_2 lines) instead of the one in a single HgTe QW.

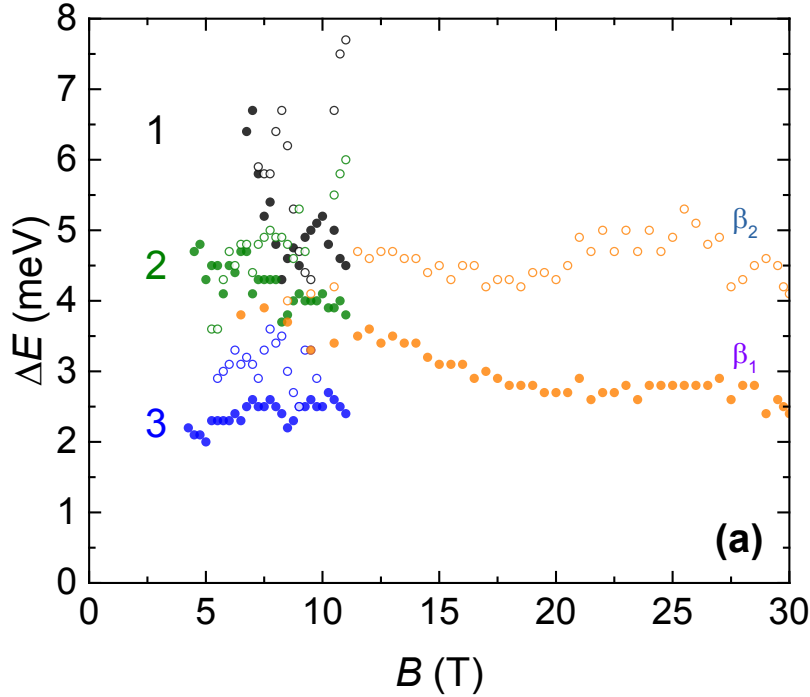


Fig. 46. The values of splitting of the lines β_1 and β_2 in various experiments for sample 150218. Solid symbols correspond to the line β_1 , open symbols correspond to the line β_2 . Orange symbols are taken from experiments in high magnetic fields up to 30 T, the others – from experiments in moderate fields up to 11 T for different hole concentrations: $1.3 \times 10^{11} \text{ cm}^{-2}$, $2 - 0.73 \times 10^{11} \text{ cm}^{-2}$, $3 - 0.65 \times 10^{11} \text{ cm}^{-2}$.

The other lines q_1 and q_2 are extension of line β^* from Fig. 42 and seem to consist of several transitions. The largest contribution to the q_1 line comes from the transitions $-1 \rightarrow 0$ ($286 \rightarrow 246$) and $1 \rightarrow 0$ ($245 \rightarrow 247$) shown as bold lines on Fig. 44. These transitions are connecting completely empty levels in conduction bands with completely populated levels in valence band, thus intensities of such lines should increase with B together with the degeneracy of LL. The q_2 line arises mostly from $1 \rightarrow 0$ ($244 \rightarrow 246$) and $1 \rightarrow 0$ ($244 \rightarrow 246$) transitions (Fig. 44 and Fig. 45). The origin of the u line remains unclear so far, as well as absence of any signatures (Fig. 44) of the presumably strong enough $-1 \rightarrow 0$ ($285 \rightarrow 247$) transition. Nevertheless, the interpretation of the remaining lines is unambiguous.

Thus, a reasonable agreement between the experimental data and the calculated transition energies allows us to assert the applicability of the axial approximation in strong magnetic fields in double HgTe QWs.

Let us now focus on the intriguing splitting of the topmost Landau level in valence band $n = -2$, which is doubly degenerate in the axial model, since the barrier is not transparent for hole-like states [67]. One can see that the lines β_1 and β_2 actually splits in two lines (Fig. 43 and Fig. 44). We plot the values of the splitting of β_1 and β_2 lines versus the magnetic field for the different experiments (Fig. 46). One can see that the characteristic values of the splitting in high

magnetic fields are about 3.5 meV for sample A and 4.5 meV for sample B. However, we must pay attention to some peculiarities.

- The values of splitting depend on the hole concentration (sensitive to blue led illumination) – the splitting becomes smaller when the hole concentration decreases (Fig. 46).
- The splitting of the β_2 line is usually greater than the splitting of the β_1 line by 0.5–2.5 meV.
- The splitting is mostly independent of the magnetic field.
- The intensities of the resolved lines are different: the right component of the β_1 line is stronger than the left component, while for the β_2 the situation is opposite (Fig. 46, Fig. 43). In other words, β_1 high-frequency component and β_2 low-frequency component are dominating in a single spectrum, i.e. for a fixed magnetic field.

The reason for this splittings is the following. In a symmetric DQW, zero-mode level $n = -2$ is doubly degenerate (it consists of $-2, 327$ and $-2, 326$ levels) (Fig. 45). The lowering of a symmetry can split them and open a gap. This may lead to the appearance of four separate $-2 \rightarrow -1$ transitions: $327 \rightarrow 287$ and $326 \rightarrow 287$ for β_1 line, and $327 \rightarrow 288$ and $326 \rightarrow 288$ for β_2 line. There are several possibilities, examined below.

(i) First, we calculated the LLs taking into account BIA & IIA effects, using the methods described in [71, 148]. Consideration of reduced symmetry does not lead to any significant splitting of the $n = -2$ levels in the DQW. In principle, the magnitude of this splitting increases with B , but it reaches only 1 meV at 30 T and cannot completely explain the experiment. Therefore, one should neither exclude the BIA and IIA from consideration nor stop searching for a stronger effect.

(ii) The most “obvious” reason seems to be the “dissimilarity” of quantum wells, which arise in the process of growth. Indeed, in sample 150218, the change in QW widths by value $\Delta d_{QW} = \pm 0.3$ nm (i.e., $d_{QW}^1 = 6.0$ nm, $d_{QW}^2 = 6.6$ nm, instead of $d_{QW}^1 = d_{QW}^2 = 6.3$ nm) leads to a splitting value of 3.5 meV. This width change seems reasonable for the MBE technology. However, the difference in the QW width does not explain the dependence of the splitting on the concentration in any way. Moreover, the calculations of transitions’ probabilities in the situation of different QWs give the opposite picture to the experiment: transitions’ probabilities for the low-energy component of β_1 line is stronger than for the high-energy component. The same contradiction is present for the β_2 line. Finally yet importantly, the inequality of QWs leads to a change in the position of all the lines, which in turn significantly worsens the agreement in the high-frequency region. Therefore, the inequality of the quantum well cannot be the main reason for the appearance of splitting.

(iii) The value of splitting clearly depends on the hole concentration controlled by the persistent photoconductivity effect, thus indicating the presence of a built-in electric field. The distribution of holes creates the electric field whose profile and magnitude depends on the number of carriers in the quantum well. The rough estimates of LLs energies with built-in constant (uniform) electric field applied perpendicular to the plane of the structure showed that the electric field “perturbs” mainly the $n = -2$ levels and certain Landau levels close to the valence band “ceiling” (in particular, the levels $n = -1, 244$ and $n = -1, 245$). Therefore, good agreement between the experimental data and the calculation results for the rectangular profile of the double QW potential for high-frequency absorption lines is also preserved when the electric field is taken into account. The required splitting of the levels $n = -2$ is about 5 meV is achieved by “switching on” the electric field of 5 kV/cm for sample A and 4 kV/cm for sample B. The calculated values of transition probabilities also agree with the experiment: from two components of the β_1 line, the transition from the lower of the levels $n = -2$, and for the line β_2 , from the upper one (compare Fig. 43, Fig. 45 and Fig. 44).

We note that the cause of the different splitting of the lines β_1 and β_2 remains unclear. (Fig. 46). The difference is small (less than the half-width of the absorption lines), but as can be seen from Fig. 46 this effect appears systematically. Perhaps a different splitting is associated with a systematic error in the decomposition of split absorption feature into two peaks, but a sophisticated reason, e.g. a difference in the structure of the wave functions within the broadened Landau levels, is not excluded, but requires additional theoretical considerations.

In conclusion, our experimental results justify the theoretical prediction [67], where the presence of a "vertical" electric field in the double quantum well HgTe / CdHgTe leads to a splitting of the degenerate level $n = -2$, i.e. to the opening of a gap in the spectrum of "bulk" states. We observe the transition of the system from the semimetallic state to the phase of the 2D topological insulator. Obviously, this phase transition can be controlled by applying an external electric field, for example, in a gated structure.

Chapter 7. Dirac fermions in InAs/GaSb/InAs

Scientific interest in semiconductor systems whose band structure is characterized by dispersion relations linear in momentum and therefore, hosting massless charge carriers resembling those in high-energy physics. The corresponding studies began with the discovery of graphene where electrons and holes are 2D massless Dirac fermions appearing in two nonequivalent valleys [186]. Since that time, 2D and 3D massless fermions were also discovered on the surfaces of 3D topological insulators [5] and in Dirac, Kane, and Weyl semimetals [187-190]. HgTe/CdHgTe quantum well is the first 2D system in which the existence of single-valley massless Dirac fermions was demonstrated experimentally [131]. The gapless state with a linear dispersion relation appears in quantum wells due to the accidental degeneracy of the lower electron-like (E1) and upper hole-like (H1) levels. It was recently predicted in [44] that a 2D system with massless Dirac fermions can also be implemented in InAs/GaSb “three-layer” quantum wells confined between wide-gap AlSb barriers. The appearance of a gapless state in such quantum wells is due to the unique location of the edges of the valence band of GaSb and the conduction band of InAs at InAs–GaSb heterojunctions. In three-layer QW InAs/GaSb/InAs at certain ratio between the thicknesses of the layer, the dispersion relation at the Γ -point of the Brillouin zone is linear with the velocities of massless Dirac fermions of $(1.5 - 3.5) \times 10^5$ m/s [44]. Such band structure is in contrast to bilayer quantum wells, where the “crossing” of the E1 and H1 subbands occurs at $k \neq 0$, which results in opening of a gap in the band spectrum because of the hybridization of subbands [96, 97]

- Krishtopenko, S.S., et al., Cyclotron resonance of Dirac fermions in InAs/GaSb/InAs quantum wells. *Semiconductors*, 2017. 51(1): p. 38-42.
- Ruffenach, S., et al., Magnetoabsorption of Dirac Fermions in InAs/GaSb/InAs “Three-Layer” Gapless Quantum Wells. *JETP Letters*, 2017. 106(11): p. 727-732.

7.1. Experimental details

The studied samples were grown by molecular beam epitaxy on GaAs (001) semi-insulating substrates with the control of the thickness by the reflection high-energy electron diffraction method at Institut d’Electronique et des Systèmes (IES, Montpellier, France; E38FT1 and E46FT2 samples) and the Rzhanov Institute of Semiconductor Physics, Siberian Branch, Russian Academy of Sciences (Novosibirsk, Russia; bp2823 sample and series st1522) [191, 192].



Structure E38 FT1 22/10/2015

		Epaisseurs visées	
		Nm	ML
	GaSb	6	
	AlSb	50	
	InAs	(12.6)	42
	GaSb	(2.7)	9
	InAs	(12.6)	42
	AlSb	50	
	Pause		
SR x 10	GaSb	1.56	
	AlSb	2.5	
	GaSb	1250	
	AlSb(As)	100	
	GaAs Buffer	<> 100	
Substrat	GaAs undoped	200	

Fig. 47. Characteristic growth parameters of the investigated heterostructures with QWs

The “active” part of the structure was grown on a composite buffer consisting of a 100- to 200-nm-thick *i*-GaAs layer and a 1.25 – 2.4 μm -thick GaSb metamorphic buffer layer (cf. [193] and Fig. 47). Further, a 10-period AlSb (2.5 nm)/GaSb (2.5 nm) “smoothing” superlattice, a 50-nm-thick AlSb lower barrier, an InAs–GaSb–InAs three-layer quantum well, a 50-nm-thick AlSb upper barrier, and a GaSb covering layer were grown with the use of technologies ensuring the formation of In–Sb bonds at the GaSb/InAs and AlSb/InAs heterojunctions [192, 193]. The samples were not specially doped. The thicknesses of the InAs and GaSb layers were taken as integers of monolayers (see Table X), using the calculations of the band structure.

Table X. Parameters of the studied InAs/GaSb/InAs three-layer quantum wells: the thickness of the GaSb buffer layer, the thickness of InAs layers in units of monolayer (1 ML = 0.303 nm), the thickness of the GaSb layer in units of monolayer, the electron density at liquid helium temperatures, and the calculated Fermi energy at a given density E_F ; the 4th line gives the parameters of the bp2823 sample under illumination

Sample	$d_{\text{buff}}, \mu\text{m}$	$d_{\text{InAs}}, \text{ML}$	$d_{\text{GaSb}}, \text{ML}$	$n_s, 10^{11} \text{cm}^{-2}$
E38FT1	1.25	42	9	7.2
E46FT2	2.0	42	9	9.2
bp2823	2.4	29	17	9.0
bp2823*	–/–	–/–	–/–	5.8
St1522(1)		29	17	
St1522(2)		30	15	
St1522(3)		33	12	

The band structure and Landau levels of InAs/GaSb/InAs three-layer quantum wells were calculated by S.S. Krishtopenko using the eight-band Kane Hamiltonian by the method of expansion of envelope wave functions in plane waves [44]. Internal elastic strains, which are due to the difference between the lattice constants of the materials in the plane of quantum

wells, were taken into account for structures grown on the GaSb buffer. The band parameters of the materials were taken from [194].

The band structure of the grown structures were experimentally investigated using cyclotron-resonance measurements in the terahertz and far-infrared ranges. Two different setups were used. In the first case, a quantum-cascade laser (QCL) operating at frequencies of $f = 3.0$ or 3.2 THz (pulse duration of $3 \mu\text{s}$; repetition period of $100\text{--}200 \mu\text{s}$) [195] was used as the source of monochromatic radiation, and the absorption spectra were recorded upon magnetic-field sweeping. The radiation passing through a sample was detected by Ge:Ga photoresistor. The signal from the photoresistor was amplified, fed into a Stanford Research Systems SR250 gated integrator, digitized, and stored in the computer memory as a function of the magnetic field. The probe with the whole optical system of source, sample and detector was immersed in liquid helium cryostat with a superconducting magnet.

In the second case, measurements were made at a set of fixed magnetic fields using a Fourier-transform spectrometer with a spectral resolution of 4 cm^{-1} . Such experiments were performed at Laboratoire Charles Coulomb, Université de Montpellier (L2C, Montpellier, France), in magnetic fields up to $B = 16 \text{ T}$ at $T = 1.6\text{K}$ and at Laboratoire National des Champs Magnétiques Intenses (LNCMI-G, Grenoble, France) in magnetic fields up to $B = 11 \text{ T}$ at $T = 4.2\text{K}$ using a superconducting solenoid and up to $B = 34 \text{ T}$ at $T = 1.6\text{K}$ using a resistive solenoid. The samples were placed in liquid helium; radiation transmitted through the sample was detected by a composite bolometer, the signal from which was amplified and was supplied to the input of the analog-to-digital converter of the spectrometer. The transmission spectrum measured in the magnetic field was normalized to $B = 0 \text{ T}$ spectrum. Simultaneously with cyclotron resonance measurements in the superconducting solenoid, the 2D electron density was determined by magnetotransport methods (Shubnikov–de Haas oscillations, Hall effect). The carrier concentration was varied owing to the negative persistent photoconductivity effect induced by a blue light emitting diode located in liquid helium near the sample (cf. [196]).

7.2. Determination of band mass in quasi-classical magnetic fields

Fig. 48 shows the calculated dependences of the energies of the four lowest electron subbands E1–E4 and the highest hole subband HH1 in a three-layer InAs/GaSb/InAs QW at $k = 0$ versus the InAs thickness for a fixed GaSb thickness of 15 ML (4.575 nm). One can see that, for an InAs-layer of 30 ML (9.15 nm , which corresponds to the parameters of sample St1522(2)), subbands E1 and HH1 cross each other and a gapless band structure with a linear dispersion relation at the Γ point (a Dirac cone) emerges in these subbands (see Fig. 49). For thicker InAs layers, the inversion of subband E1 and HH1 takes place and the system becomes a 2D topological insulator.

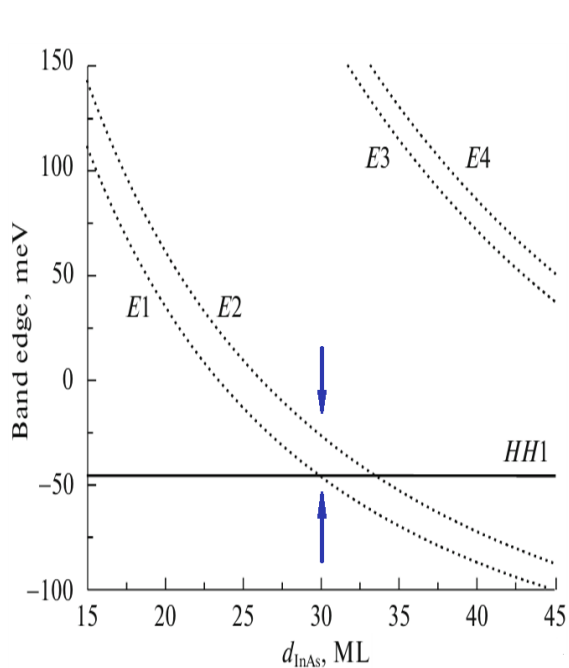


Fig. 48. Calculated edge energies of the electron subbands E1–E4 and the hole subband HH1 (dotted and solid lines, respectively) in a three-layer InAs/GaSb/InAs QW versus the thickness of the InAs layers for a GaSb-layer thickness of 15 ML (4.575 nm). It is assumed that the structure is grown on a metamorphic GaSb buffer layer.

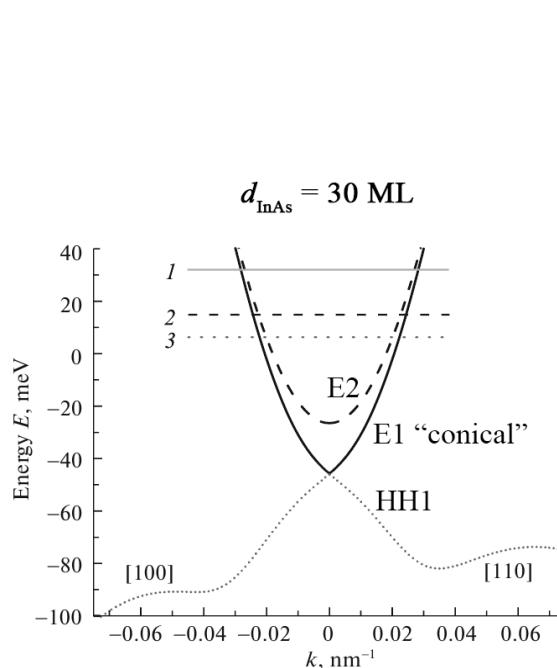


Fig. 49. Dispersion relations in the conduction and valence bands in heterostructure St1522(2) along two directions in the quasimomentum space. Horizontal lines show the positions of the Fermi level in the “dark” and upon sample illumination calculated on the basis of the measured charge-carrier concentrations $n_s = 2.4 \times 10^{12}$, 1.62×10^{12} , and $1.37 \times 10^{12} \text{ cm}^{-2}$ in (1), (2), (3), respectively.

In the insets in Fig. 50 we show the cyclotron resonance spectra in the samples under study recorded using the QCL setup for different values of the 2D electron concentration n_s . One can see that, for a high total concentration of electrons in subbands E1 and E2 ($n_s > 10^{12} \text{ cm}^{-2}$, which corresponds to “dark” conditions), the spectra feature a single absorption line. This is explained by the fact that the values of the cyclotron mass m_c at the Fermi level in the two subbands E1 and E2 are close to each other (see Fig. 50). In sample St1522(3), this line was observed up to magnetic fields of 15 T (Fig. 51). In the entire range of magnetic fields investigated, the position of this line varies linearly with field (see Fig. 51, inset). This corresponds to the “classical” cyclotron resonance at high filling factors ν . For lower values of the total electron concentration (in both subbands, E1 and E2, $n_s \sim 1.5 \times 10^{12} \text{ cm}^{-2}$), the cyclotron resonance line broadens considerably, which is caused by an increased difference in the effective masses in the “conical” subband E1 and “parabolic” subband E2. This effect is most pronounced in sample St1522(2), where it was possible to reduce the electron concentration to the greatest extent. According to Fig. 50(b), a decrease in the electron concentration is accompanied by a considerable shift of the absorption peak to lower magnetic fields (smaller cyclotron masses).

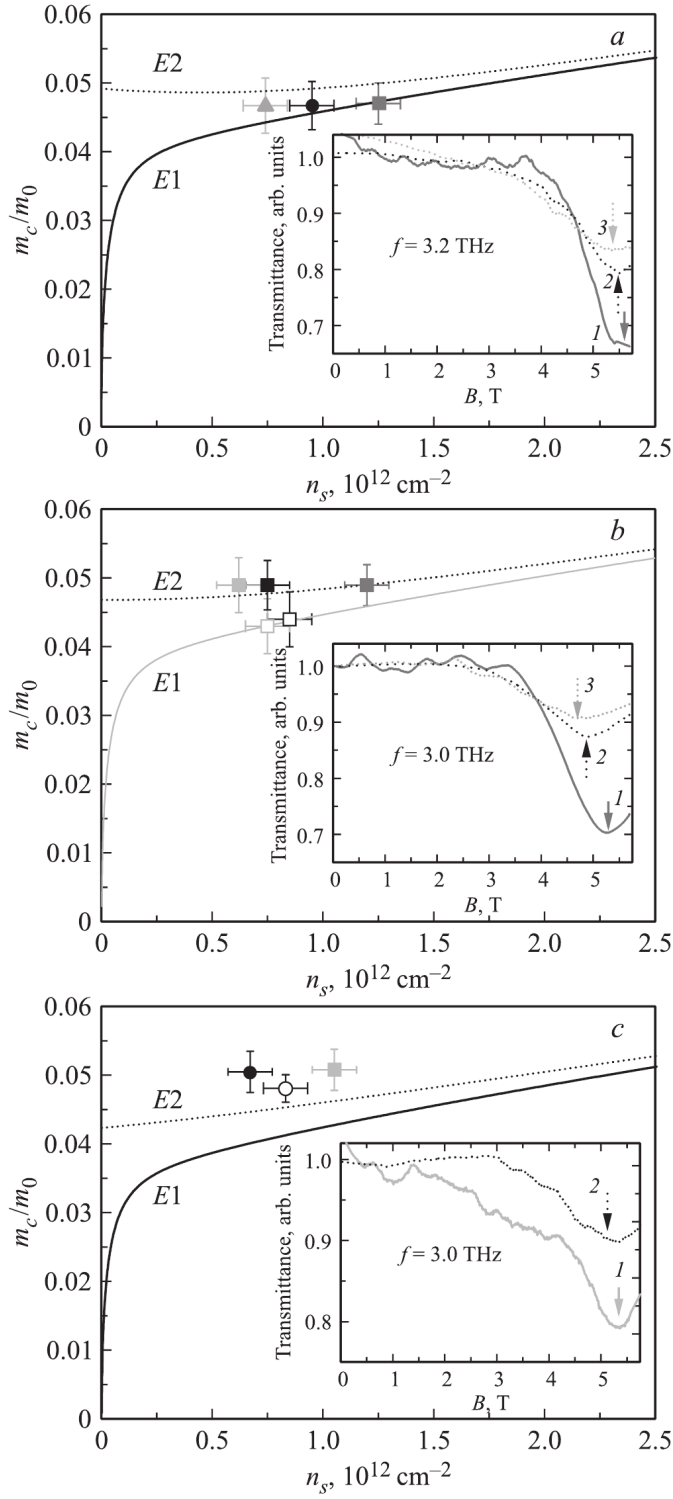


Fig. 50. Calculated dependences of the effective mass on the electron concentration in subbands E1 and E2 (solid and dashed lines, respectively) in samples St1522(1)–St1522(3) (panels (a)–(c), respectively). The experimentally determined values are shown by symbols. The insets show the cyclotron resonance spectra measured in the “dark” and upon sample illumination (solid and dashed lines, respectively). The carrier concentrations are (a:1,2,3) $n_s = 2.5$, 1.9 and $1.6 \times 10^{12} \text{ cm}^{-2}$; (b:1,2,3) $n_s = 2.4$, 1.62 and $1.37 \times 10^{12} \text{ cm}^{-2}$; and (c:1,2) $n_s = 2.1$ and $1.5 \times 10^{12} \text{ cm}^{-2}$.

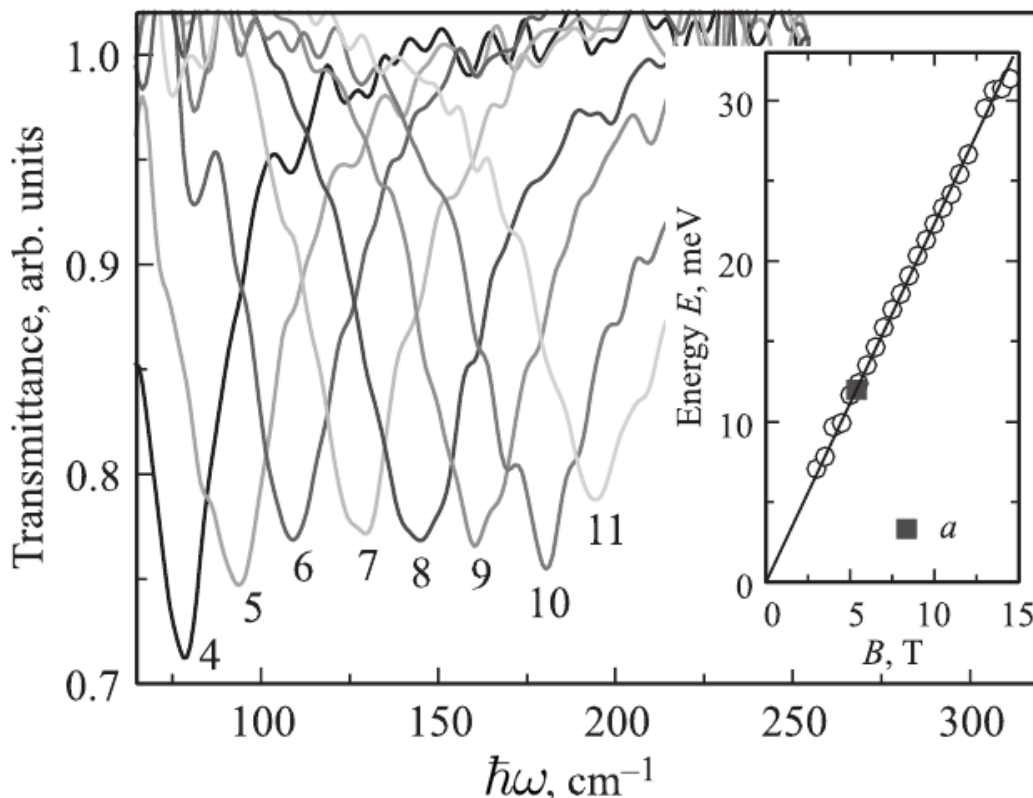


Fig. 51. Cyclotron resonance spectra of sample St1522(3) in the dark measured by Fourier-transform spectroscopy. The numbers next to each curve indicate the values of the magnetic field in tesla. The inset shows the position of the cyclotron resonance line as a function of magnetic field. Square symbol *a* shows the position of the line measured in the setup based on a QCL (see Fig. 50(c)).

The values of the cyclotron mass obtained from the measured magnetoabsorption spectra are shown by symbols in Fig. 50. The electron concentrations in each of the subbands E1 and E2 were determined on the basis of the calculated dispersion relation. One can see that, for samples St1522(1) and St1522(2), the experimentally obtained cyclotron masses agree very well with the calculated ones, but there is a discrepancy between the theoretical and experimental values for sample St1522(3). Its origin is currently unclear. Relying on the dispersion relation for sample St1522(2), plotted in Fig. 50, we find that, for a total 2D electron concentration of $n_s = 1.37 \times 10^{12} \text{ cm}^{-2}$, 55% and 45% of electrons reside in the “conical” subband E1 and “parabolic” subband E2, respectively. The observed shift of the cyclotron resonance line upon a decrease in the electron concentration to $n_s = 1.37 \times 10^{12} \text{ cm}^{-2}$ is in good agreement with the calculated value $m_c = 0.043 m_0$ of the effective mass in the subband with a conical dispersion relation for an electron concentration in this particular subband of $n_{E1} = 0.76 \times 10^{12} \text{ cm}^{-2}$. Such an adequate agreement confirms the correctness of the predicted band structure, in other words, profile of the band structure was calculated correctly.

7.3. Cyclotron resonance in quantizing magnetic fields up to 34 T

The results of investigations of the CR in the “three-layer” InAs/GaSb/InAs quantum wells in the previous section reveal the challenge concerning accurate detection of the difference in the dispersion laws of “conical” and parabolic subbands. Particular difficulties are related to the rather large persistent electron concentrations after illumination with blue led, thus the position of the Fermi level in the structures under study is far from the bottom of the conduction band, where one should observe effects that are more pronounced. Therefore, further experiments

obviously due to the classical electron cyclotron resonance (at $\hbar\omega_c \ll E_F$) and the absence of splitting indicates a small difference between cyclotron masses at the Fermi level in the E1 and E2 subbands. The second absorption line at higher energies appears in the spectra at high magnetic fields $B > 10$ T and its intensity increases with the B .

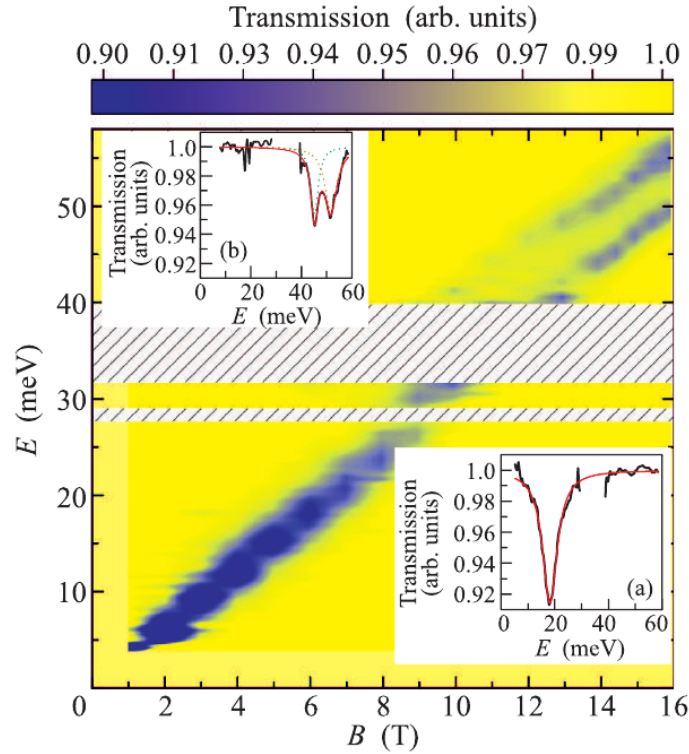


Fig. 53. Magnetoabsorption spectra in the E38FT2 sample at $T = 1.6$ K represented in the form of a false-color map. The insets show the transmission spectra at $B = 6$ T (a) and $B = 14.5$ T (b) and their Lorentzian approximations. The lower and upper gray shaded bands are the reststrahlen regions in InAs and in GaAs substrate, respectively.

The positions and intensities of magnetoabsorption lines in the E38FT1 and E46FT2 samples obtained from different experiments are summarized in Fig. 54. The careful analysis of absorption spectra makes it possible to reveal features not directly observed in the false-color map in Fig. 53. One can see that the field dependence of observed transition energies in fields up to $B = 8$ T are well described by a nearly sublinear dependence whose approximate slope at fields up to $B = 3$ T corresponds to the cyclotron mass $m_c = (0.038 \pm 0.002) m_0$. This value is in a good agreement with the calculated cyclotron masses. For a given value of the Fermi level in the size-quantized subbands one can obtain following values: $m_c \approx 0.034 m_0$ and $m_c \approx 0.037 m_0$ in the E1 and E2 subbands, respectively.

The lines in Fig. 54 represent theoretically expected B -dependences of the energies of allowed transitions between the lower Landau levels in the band (see Fig. 52). One can see that the observed positions of the cyclotron resonance line in fields up to $B = 8$ T correspond to a large number of transitions, the intensities of which depend on the occupation of involved LLs. Since the energies of different transitions are close to each other, they cannot be resolved in the measured magnetoabsorption spectra. However, differences in the energies of transitions should be observed in high magnetic fields where the effects due to nonparabolicity become more pronounced. As follows from Fig. 54, such differences in energies in the E38FT1 and E46FT2 samples start to be manifested in fields above $B = 8$ T. At the same time, in the E46FT2 sample in some magnetic fields (e.g., $B = 3.5, 4.5,$ and 5.5 T), a pronounced broadening was observed for the cyclotron resonance line. A noticeable deviation from a linear dependence, as well as the splitting of the cyclotron resonance line, was observed in the energy range of

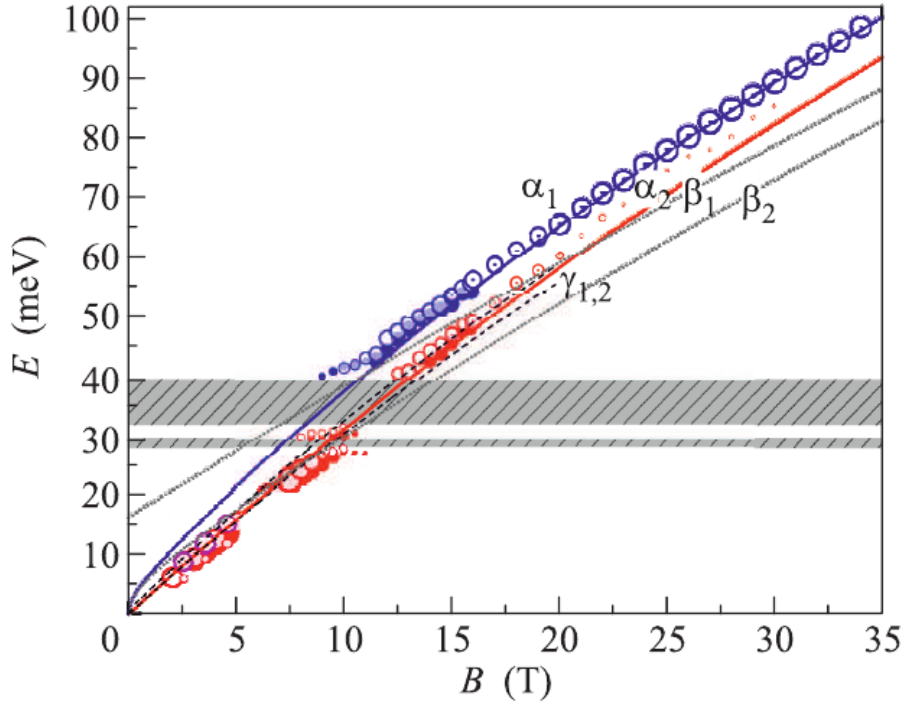


Fig. 54. (Lines) Calculated magnetic field dependences of the energies of transitions and (symbols) positions of the magnetoabsorption spectral lines. Closed and open symbols are results for the E38FT1 and E46FT2 samples, respectively, in the magnetic field up to $B = 16$ T in the superconducting solenoid. Open symbols with point are results for the E46FT2 sample in the magnetic field up to $B = 34$ T in the resistive solenoid. The areas of the symbols are proportional to the integral intensities of absorption lines. The gray shaded bands are the reststrahlen regions.

$\hbar\omega = 27.7\text{--}29.0$ meV in magnetic fields of $B = 8\text{--}11$ T. This is obviously due to the polaron effects (interaction between electrons and an LO phonon [197, 198]), but one cannot exclude dielectric artifact. The indicated energies are somewhat below the energy of the LO phonon in InAs ($\hbar\omega = 30.1$ meV), which is most likely caused by the screening effect in the 2D electron gas [199, 200].

Two cyclotron resonance modes were observed in magnetic fields above 10 T at energies above the reststrahlen regions in the GaAs substrate in both samples. The low-frequency line is the “extension” of the cyclotron resonance line observed in fields up to 8 T. The filling factor of Landau levels in fields above 10–12 T is smaller than $\nu < 3$ for both samples, thus γ_1 and α_2 transitions with close energies are the main transitions contributing to the low-frequency absorption line (see Fig. 52). At the same time, the Landau level $n = 1$ from subband E1 in these fields is empty, which results in the appearance of absorption (α_1 transition) between the $n = 0$ and $n = 1$ levels. The energy of this transition is noticeably higher than the energy of other transitions from lower Landau levels in the conduction band; just this transition is responsible for the second high-frequency cyclotron resonance line. The appearance of α_1 transition correlates well with the depletion of $n = 1$ levels and, cannot be directly seen in our experiment due to absorption in reststrahlen band of the GaAs substrate.

In magnetic fields above 18 T, corresponding to filling factors $\nu \leq 2$ in E46FT2 sample, the intensity of the low-frequency line decreases strongly. The reasons are (i) crossing of the Landau levels $n = -1$ and $n = 0$ (see Fig. 52) and switching off the γ_1 transition and (ii) depletion of the upper level $n = 0$ with the increasing magnetic field and, correspondingly, weakening of the α_2 transition. It is noteworthy that the $\beta_{1,2}$ transitions between the upper Landau level $n = -2$ in the valence band and the levels $n = -1$ in the conduction band were not observed in the

InAs/GaSb/InAs structures under study. Such a transition is one of the most intense in HgTe/CdHgTe quantum wells in quantizing magnetic fields [23, 26, 28]. The calculations show that oscillator strengths for the $\beta_{1,2}$ transitions are much smaller (by a factor of at least 5) than those for the discussed transitions between Landau levels in the conduction band. This relation is caused by the weak overlapping of electron-like (localized predominantly in InAs layers) and hole-like (localized in the GaSb layer) components of the wave functions of the states involved in these transitions.

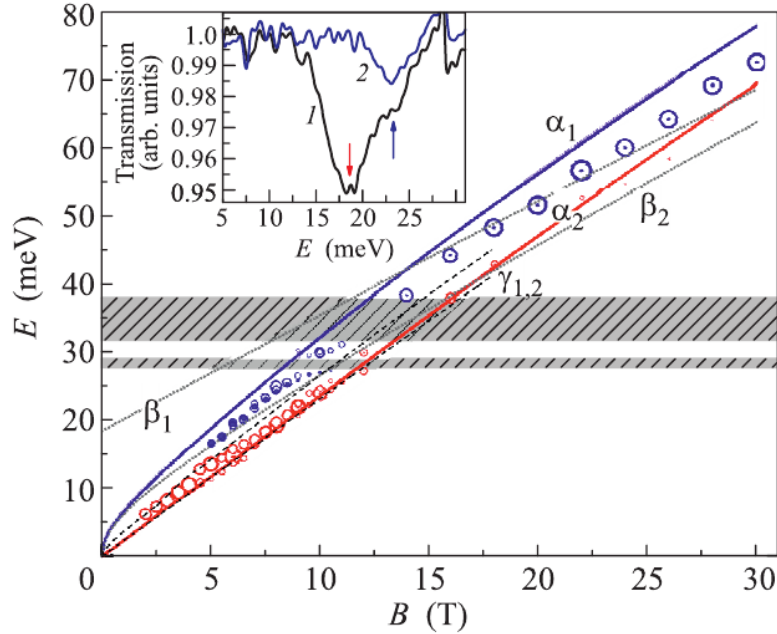


Fig. 55. Calculated magnetic field dependences of the energies of transitions and (symbols) positions of the magnetoabsorption spectral lines in the bp2823 sample. Open and closed symbols are obtained in dark and at illumination by a blue light emitting diode. Open symbols with point are results obtained in the magnetic field up to $B = 30$ T in the resistive solenoid. The areas of the symbols are proportional to the integral intensities of absorption lines. The gray shaded bands are the reststrahlen regions. The inset shows the magnetoabsorption spectra in the bp2823 sample in a magnetic field of $B = 7.5$ T obtained (1) in dark and (2) at illumination by a blue light emitting diode.

The magnetoabsorption data RAS at two electron densities are summarized in Fig. 55 for bp2823 sample grown in ISP SB. This figure also demonstrates two CR modes, but the high-frequency mode in dark was also detected at energies below the reststrahlen band in fields of $B = 7.5$ –11 T (see the inset of Fig. 55) because the energies of transitions in the bp2823 sample in a given magnetic field are lower than those in the E38FT1 and E46FT2 samples. The calculations of the transition energies (Fig. 55) indicate that the energy of the γ_1 transition in the bp2823 sample is noticeably higher than the energies of nearby transitions γ_2 , α_2 , δ_1 , δ_2 and is lower than the energy of the α_1 transition. At the dark electron density $n_s = 9 \times 10^{11} \text{ cm}^{-2}$, the depletion of the final Landau level $n = 1$ of the α_1 transition (Fig. 56) starts above 7.2 T, which correspond to the filling factor of Landau levels $\nu < 5$. As seen in the inset of Fig. 55, the high-energy tail of the absorption line (caused by the γ_2 , α_2 and δ_1 transitions) at $B = 7.5$ T under dark conditions exhibits a feature which lies between the energies of the α_1 and γ_1 transitions and can be traced down to $B = 6.5$ T according to Fig. 55. After illumination by a blue light-emitting diode, when the electron density decreases by a factor of more than 1.5 (inset of Fig. 55), only this high-frequency line remains. In this case, the α_2 and γ_2 transitions should appear in spectra in a field below $B = 7.5$ T. The calculation shows that these transitions have the oscillator strength 20–30% smaller than that for the α_1 and γ_1 transitions and they are

apparently hidden in noise (the signal-to-noise ratio decreases with decreasing frequency because of a decrease in the spectral power density of the radiation source, in this case, global).

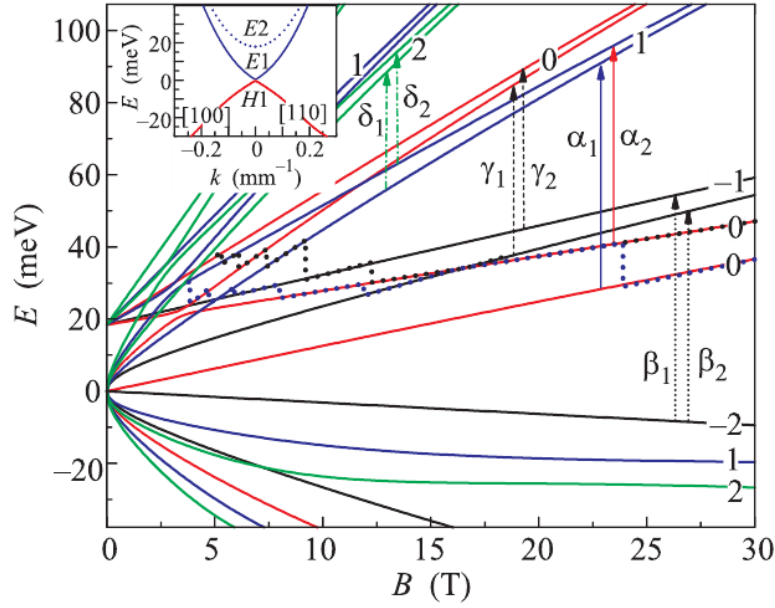


Fig. 56. Calculated Landau levels for the bp2823 sample. The numbers of the levels are indicated near the curves. Broken dotted lines are the positions of the Fermi levels calculated using the measured densities in dark and at illumination (see Table X). Vertical arrows mark possible magneto-optical transitions. The inset shows the calculated dispersion relations in the conduction and valence bands for two directions of the quasimomentum.

The calculated cyclotron masses at the Fermi level in dark ($n_s = 9 \times 10^{11} \text{ cm}^{-2}$) are $m_{E1} = 0.043 m_0$ in the “conical” E1 subband and $m_{E2} = 0.049 m_0$ in the “parabolic” E2 subband. According to Fig. 55, the spectral position of the low frequency line in dark in low (classical) magnetic fields deviates from a linear dependence toward higher energies, which corresponds to the transition from the classical cyclotron resonance to quantized transitions between LLs. In particular, at $B = 3 \text{ T}$ ($\nu = 12$), the position of this line corresponds to the mass of $0.045 m_0$, i.e., is close to the average value of the masses in the parabolic and conical subbands. The spectral range above the reststrahlen band in the GaAs substrate in magnetic fields of 16–30 T includes two lines, strong high frequency and weak low frequency, similar to those observed in the E38FT1 and E46FT2 samples. These lines are “extensions” of the corresponding lines in fields up to $B = 11 \text{ T}$. Consequently, it is reasonable to attribute the high and low frequency lines to the α_1 and α_2 transitions, respectively. The γ_1 transition should not contribute to the low-frequency line because the filling factor in fields above 18 T is $\nu < 2$ and the initial Landau level $n = -1$ of the γ_1 transition becomes empty. A small difference of the position of the high-frequency line from the calculated position of the α_1 transition is most likely due to the difference of real parameters of structures from those used in the calculation.

To summarize, the measurements of magnetoabsorption spectra in magnetic fields up to $B = 34 \text{ T}$ in InAs/GaSb/InAs “three-layer” quantum wells have revealed the absorption line associated with the transition from the several lowest Landau levels in the subband with the conical dispersion relation. Reasonable agreement of the experimental energies of transitions with theoretical calculations qualitatively confirms the predicted gapless band structure with massless Dirac fermions in studied samples.

Conclusions

This doctoral thesis has been dedicated to experimental and theoretical investigations of 2D and quasi-2D heterostructures based on HgCdTe and InAs/InAb compounds using tools of infrared and THz magneto-spectroscopy combined with complementary magneto-transport measurements. This combination of experimental methods, accompanied by theoretical modelling using the expanded 8×8 Kane model, allowed us to get deeper insights in the electronic band structure of explored systems, in particular, to identify the symmetry-lowering effects having relatively strong impact on electronic band in the explored systems. The set of investigated samples comprises single HgTe quantum wells (either symmetric or with an asymmetric doping in the barriers), HgTe double quantum wells and heterostructures based on InAs/InSb.

Main achievements/conclusions of this work are:

1. Both interband and intraband resonant absorption lines between Landau levels in valence and conduction bands have been revealed in the spectral range of 5–250 meV in quantizing magnetic fields of p -type quantum wells HgTe / CdHgTe with both normal and inverted band structure. We have shown that the spectral positions of the lines associated with interband transitions and dominant (most intense) lines due to transitions within the valence band are in good agreement with the results of calculations of the transition energies between Landau levels in the framework of the axial approximation in the 4-band Kane model.
2. Axially forbidden transitions are found in the transmittance spectra in quantum wells with a normal band structure. We show that the violation of the selection rules is related to the mixing of states in the valence band due to the anisotropy of the chemical bonds at the heterointerfaces and the absence of an inversion center in the crystal lattice. This mixing of states leads to a redistribution of the eight-component wave functions across neighbouring Landau levels and consequently redistribution of probabilities of transitions allowed in the axial model between interacting Landau levels of the valence band. This explains the applicability of the axial approximation to the majority of observed transitions. In a sample with an inverted band structure, an avoided crossing was first observed for the case of partial filling of the "zero" Landau levels, which indicates a single-particle character of the phenomenon.
3. The absorption spectra were studied in both classical and quantizing magnetic fields in asymmetric heterostructures with HgCdTe / CdHgTe quantum wells with a selective one-sided doping of barriers with a large electron density ($n_s \geq 10^{12} \text{ cm}^{-2}$). A strong splitting of the cyclotron resonance line ($\sim 10\%$) is observed at low fields, which is related to the Rashba effect in samples with both inverted and, for the first time, normal band structure. The obtained results are in good agreement with the data of self-consistent calculations of energy spectra (at $B = 0$) and Landau levels in the framework of the 8-band Kane model in the Hartree approximation. It is shown that in both cases a large share (up to 50%) of "hole" wave functions (p -type) is present in the states of the lower subband of the conduction band, leading to a giant (over 20 meV) spin splitting of the lower subband at the Fermi level. The complex composition of cyclotron resonance modes changes with B , which is associated with magnetic quantization in the upper subband with a smaller number of filled Landau levels. The evolution of the absorption lines with a magnetic field is traced up to 34 T, when the magnetic quantization already prevails over the Rashba splitting. In magnetic fields of 15–20 T in the absorption spectra, a manifestation of the anticrossing of the Landau levels from the first and second subbands of size quantization was observed.
4. Shubnikov-de Haas oscillations at $T = 1.6 - 40$ K were investigated in HgTe/CdHgTe quantum wells of width $d_{QW} = 8$ nm with electron concentration $(1.7-13) \times 10^{11} \text{ cm}^{-2}$.

Analysis of the temperature dependence of the oscillation amplitude for integer filling factors provide the values of the energy gaps between the adjacent Landau levels and the quantum scattering time. The experimental values of the gaps are in good agreement with the results of single-electron energy level calculations within the framework of the four-band Kane model. The obtained experimental values of the density of states indicate a strong screening of the exchange interaction in the quantum wells of HgTe / CdHgTe.

5. The magnetoabsorption spectra of double quantum wells HgTe/CdHgTe of different parameters were studied. We demonstrated doubling (compared to a single QW) of the number of main magnetoabsorption lines, associated with tunnelling transparency of the barrier for electronic states. Good agreement was obtained between the spectral positions of the absorption lines and the results of calculations of the Landau levels in the framework of the 8-band Kane model with a rectangular potential profile, which made it possible to uniquely determine the type of the band structure: normal and inverted (similar structure in bilayer graphene). In a sample with a QW width close to the critical value ($d_c = 6.3$ nm), a shift in the magnetoabsorption lines was observed with a change in the carrier concentration due to the persistent photoconductivity effect associated with a change in the potential profile upon recharge of traps. Thus, the possibility of opening a gap in the spectrum and controlling a topological phase transition due to the application of an electric field in such structures is shown.

Author's publications related to this work

- A1. Bovkun, L.S., et al., Exchange enhancement of the electron g-factor in a two-dimensional semimetal in HgTe quantum wells. *Semiconductors*, 2015. 49(12): p. 1627-1633.
- A2. Bovkun, L.S., et al., Magneto spectroscopy of double HgTe/CdHgTe quantum wells. *Semiconductors*, 2016. 50(11): p. 1532-1538.
- A3. Bovkun, L.S., et al., Activation conductivity in HgTe/CdHgTe quantum wells at integer Landau level filling factors: role of the random potential. *Semiconductors*, 2017. 51(12): p. 1562-1570.
- A4. Ikonnikov, A.V., et al., On the Band Spectrum in p-type HgTe/CdHgTe heterostructures and its transformation under temperature variation. *Semiconductors*, 2017. 51(12): p. 1531-1536.
- A5. Krishtopenko, S.S., et al., Cyclotron resonance of Dirac fermions in InAs/GaSb/InAs quantum wells. *Semiconductors*, 2017. 51(1): p. 38-42.
- A6. Ruffenach, S., et al., Magnetoabsorption of Dirac Fermions in InAs/GaSb/InAs "Three-Layer" Gapless Quantum Wells. *JETP Letters*, 2017. 106(11): p. 727-732.
- A7. Bovkun, L.S., et al., Landau level spectroscopy of valence bands in HgTe quantum wells: Effects of symmetry lowering. <https://arxiv.org/abs/1711.08783>, 2018 (with referees).
- A8. Bovkun, L.S., et al., Magneto-optics in HgTe/CdTe quantum wells with giant Rashba splitting in magnetic fields up to 34 T. *Semiconductors*, 2019 (in print).
- A9. Bovkun, L.S., et al., Polarization-sensitive Fourier spectroscopy of HgTe quantum wells. *JETP Letters*, 2018. 108(5): p. 352 (in print).

Bibliography

1. Weiler, M.H., *Magneto-optical Properties of Hg(1-x)Cd(x)Te Alloys*, in *Semiconductors and Semimetals*, R.K. Willardson and A.C. Beer, Editors. 1981, Elsevier. p. 119-191.
2. Kruse, P.W., *Review of the Electrical, Optical, and Structural Properties*, in *Mercury Cadmium Telluride*, R.K. Willardson and A.C. Beer, Editors. 1981, Academic Press. p. 383.
3. Becker, C.R. and S. Krishnamurthy, *Band Structure and Related Properties of HgCdTe*, in *Mercury Cadmium Telluride: Growth, Properties and Applications*, P. Capper and J. Garland, Editors. 2010, Wiley.
4. Fu, L., C.L. Kane, and E.J. Mele, *Topological Insulators in Three Dimensions*. Physical Review Letters, 2007. **98**(10): p. 106803.
5. Hasan, M.Z. and C.L. Kane, *Colloquium: Topological insulators*. Reviews of Modern Physics, 2010. **82**(4): p. 3045-3067.
6. König, M., S. Wiedmann, C. Brune, A. Roth, H. Buhmann, L.W. Molenkamp, X.L. Qi, and S.C. Zhang, *Quantum spin hall insulator state in HgTe quantum wells*. Science, 2007. **318**(5851): p. 766-70.
7. Krishtopenko, S.S. and F. Teppe, *Realistic picture of helical edge states in HgTe quantum wells*. Physical Review B, 2018. **97**(16): p. 165408.
8. Ruan, J., S.-K. Jian, H. Yao, H. Zhang, S.-C. Zhang, and D. Xing, *Symmetry-protected ideal Weyl semimetal in HgTe-class materials*. Nature Communications, 2016. **7**: p. 11136.
9. Capper, P., *Bulk Growth of Mercury Cadmium Telluride*, in *Mercury Cadmium Telluride: Growth, Properties and Applications*, P. Capper and J. Garland, Editors. 2010, Wiley.
10. Micklethwaite, W.F.H., *The Crystal Growth of Cadmium Mercury Telluride*, in *Mercury Cadmium Telluride*, R.K. Willardson and A.C. Beer, Editors. 1981, Academic Press.
11. Whitsett, C.R., J.G. Broerman, and C.J. Summers, *Crystal Growth and Properties of HgCdSe Alloys*, in *Semiconductors and Semimetals*, R.K. Willardson and A.C. Beer, Editors. 1981, Elsevier. p. 54-114.
12. Kershaw, S.V., M. Burt, M. Harrison, A. Rogach, H. Weller, and A. Eychmüller, *Colloidal CdTe/HgTe quantum dots with high photoluminescence quantum efficiency at room temperature*. Applied Physics Letters, 1999. **75**(12): p. 1694-1696.
13. Rogach, A.L., M.T. Harrison, S.V. Kershaw, A. Kornowski, M.G. Burt, A. Eychmüller, and H. Weller, *Colloidally Prepared CdHgTe and HgTe Quantum Dots with Strong Near-Infrared Luminescence*. physica status solidi (b), 2001. **224**(1): p. 153-158.
14. Mikhailov, N.N., R.N. Smirnov, S.A. Dvoretzky, Y.G. Sidorov, V.A. Shvets, E.V. Spesivtsev, and S.V. Rykhliitski, *Growth of HgCdTe nanostructures by molecular beam epitaxy with ellipsometric control*. International Journal of Nanotechnology, 2006. **3**(1): p. 120.
15. Chu, J.H. and A. Sher, *Superlattice and Quantum Well*, in *Device Physics of Narrow Gap Semiconductors*. 2010, Springer.
16. Rogalski, A., *HgCdTe infrared detector material: history, status and outlook*. Reports on Progress in Physics, 2005. **68**(10): p. 2267.

17. Eisen, Y. and A. Shor, *CdTe and CdZnTe materials for room-temperature X-ray and gamma ray detectors*. Journal of Crystal Growth, 1998. **184-185**: p. 1302-1312.
18. Bernevig, B.A., T.L. Hughes, and S.C. Zhang, *Quantum spin Hall effect and topological phase transition in HgTe quantum wells*. Science, 2006. **314**(5806): p. 1757-61.
19. Guldner, Y., C. Rigaux, A. Mycielski, and Y. Couder, *Magneto-optical Investigation of Hg(1-x)Cd(x)Te Mixed Crystals II. Semiconducting Configuration and Semimetal → Semiconductor Transition*. physica status solidi (b), 1977. **82**(1): p. 149-158.
20. Groves, S.H., T.C. Harman, and C.R. Pidgeon, *Interband magnetoreflexion of HgCdTe*. Solid State Communications, 1971. **9**(8): p. 451-455.
21. McCombe, B.D., R.J. Wagner, and G.A. Prinz, *Infrared pulsed gas laser studies of combined resonance and cyclotron-phonon resonance in Hg1-xCdxTe*. Solid State Communications, 1970. **8**(21): p. 1687-1691.
22. Harman, T.C., A.J. Strauss, D.H. Dickey, M.S. Dresselhaus, G.B. Wright, and J.G. Mavroides, *Low Electron Effective Masses and Energy Gap in HgCdTe*. Physical Review Letters, 1961. **7**(11): p. 403-405.
23. Zholudev, M., F. Teppe, M. Orlita, C. Consejo, J. Torres, N. Dyakonova, M. Czupkiewicz, J. Wróbel, G. Grabecki, N. Mikhailov, S. Dvoretiskii, A. Ikonnikov, K. Spirin, V.Y. Aleshkin, V. Gavrilenko, and W. Knap, *Magneto-spectroscopy of two-dimensional HgTe-based topological insulators around the critical thickness*. Physical Review B, 2012. **86**(20): p. 205420.
24. Schultz, M., F. Heinrichs, U. Merkt, T. Colin, T. Skauli, and S. Løvold, *Rashba spin splitting in a gated HgTe quantum well*. Semiconductor Science and Technology, 1996. **11**(8): p. 1168.
25. Spirin, K.E., A.V. Ikonnikov, A.A. Lastovkin, V.I. Gavrilenko, S.A. Dvoretiskii, and N.N. Mikhailov, *Spin splitting in HgTe/CdHgTe (013) quantum well heterostructures*. JETP Letters, 2010. **92**(1): p. 63-66.
26. Schultz, M., U. Merkt, A. Sonntag, U. Rössler, R. Winkler, T. Colin, P. Helgesen, T. Skauli, and S. Løvold, *Crossing of conduction- and valence-subband Landau levels in an inverted HgTe/CdTe quantum well*. Physical Review B, 1998. **57**(23): p. 14772-14775.
27. Ikonnikov, A.V., M.S. Zholudev, K.E. Spirin, A.A. Lastovkin, K.V. Maremyanin, V.Y. Aleshkin, V.I. Gavrilenko, O. Drachenko, M. Helm, J. Wosnitza, M. Goiran, N.N. Mikhailov, S.A. Dvoretiskii, F. Teppe, N. Diakonova, C. Consejo, B. Chenaud, and W. Knap, *Cyclotron resonance and interband optical transitions in HgTe/CdTe(013) quantum well heterostructures*. Semiconductor Science and Technology, 2011. **26**(12): p. 125011.
28. Zholudev, M.S., A.V. Ikonnikov, F. Teppe, M. Orlita, K.V. Maremyanin, K.E. Spirin, V.I. Gavrilenko, W. Knap, S.A. Dvoretiskiy, and N.N. Mihailov, *Cyclotron resonance in HgTe/CdTe-based heterostructures in high magnetic fields*. Nanoscale Research Letters, 2012. **7**(1): p. 534.
29. Ikonnikov, A.V., M.S. Zholudev, K.V. Maren'yanin, K.E. Spirin, A.A. Lastovkin, V.I. Gavrilenko, S.A. Dvoretiskii, and N.N. Mikhailov, *Cyclotron resonance in HgTe/CdTe(013) narrowband heterostructures in quantized magnetic fields*. JETP Letters, 2012. **95**(8): p. 406-410.
30. Shuvaev, A., V. Dziom, Z.D. Kvon, N.N. Mikhailov, and A. Pimenov, *Universal Faraday Rotation in HgTe Wells with Critical Thickness*. Phys Rev Lett, 2016. **117**(11): p. 117401.

31. Pakmehr, M., C. Bruene, H. Buhmann, L.W. Molenkamp, A.V. Stier, and B.D. McCombe, *Landau levels and spin splitting in the two-dimensional electron gas of a HgTe quantum well near the critical width for the topological phase transition*. Physical Review B, 2014. **90**(23): p. 235414.
32. Dantscher, K.M., D.A. Kozlov, M.T. Scherr, S. Gebert, J. Bärenfänger, M.V. Durnev, S.A. Tarasenko, V.V. Bel'kov, N.N. Mikhailov, S.A. Dvoretzky, Z.D. Kvon, J. Ziegler, D. Weiss, and S.D. Ganichev, *Photogalvanic probing of helical edge channels in two-dimensional HgTe topological insulators*. Physical Review B, 2017. **95**(20): p. 201103.
33. Dziom, V., A. Shuvaev, A. Pimenov, G.V. Astakhov, C. Ames, K. Bendias, J. Bottcher, G. Tkachov, E.M. Hankiewicz, C. Brune, H. Buhmann, and L.W. Molenkamp, *Observation of the universal magnetoelectric effect in a 3D topological insulator*. Nat Commun, 2017. **8**: p. 15197.
34. Schulman, J.N. and T.C. McGill, *The CdTe/HgTe superlattice: Proposal for a new infrared material*. Applied Physics Letters, 1979. **34**(10): p. 663-665.
35. Berroir, J., Y. Guldner, and M. Voos, *HgTe-CdTe superlattices: Magneto-optics and band structure*. IEEE Journal of Quantum Electronics, 1986. **22**(9): p. 1793-1798.
36. Berroir, J.M., Y. Guldner, J.P. Vieren, M. Voos, and J.P. Faurie, *Magneto-optical determination of the HgTe-CdTe superlattice band structure*. Physical Review B, 1986. **34**(2): p. 891-894.
37. Perez, J.M., R.J. Wagner, J.R. Meyer, J.W. Han, J.W. Cook, Jr., and J.F. Schetzina, *Magneto-optical properties of highly anisotropic holes in HgTe/CdTe superlattices*. Phys Rev Lett, 1988. **61**(19): p. 2261-2264.
38. Hoffman, C.A., J.R. Meyer, F.J. Bartoli, J.W. Han, J.W. Cook, J.F. Schetzina, and J.N. Schulman, *Band-gap-dependent electron and hole transport in p-type HgTe-CdTe superlattices*. Physical Review B, 1989. **39**(8): p. 5208-5221.
39. Meyer, J.R., R.J. Wagner, F.J. Bartoli, C.A. Hoffman, and L.R. Ram-Mohan, *Double hole cyclotron resonance in zero-gap HgTe-CdTe superlattices*. Physical Review B, 1989. **40**(2): p. 1388-1391.
40. Dobrowolska, M., T. Wojtowicz, H. Luo, J.K. Furdyna, O.K. Wu, J.N. Schulman, J.R. Meyer, C.A. Hoffman, and F.J. Bartoli, *Far-infrared magneto-optical study of holes and electrons in zero-band-gap HgTe/Cd_{0.85}Hg_{0.15}Te superlattices*. Physical Review B, 1990. **41**(8): p. 5084-5095.
41. von Truchseß, M., V. Latussek, F. Goschenhofer, C.R. Becker, G. Landwehr, E. Batke, R. Sizmann, and P. Helgesen, *Magneto-optics and valence-band discontinuity in a HgTe-HgCdTe superlattice*. Physical Review B, 1995. **51**(24): p. 17618-17623.
42. Ruffenach, S., A.M. Kadykov, V. Romyantsev, J. Torres, D. Coquillat, D. But, S.S. Krishtopenko, C. Consejo, W. Knap, M. Helm, M.A. Fadeev, N. Mikhailov, S.A. Dvoretzki, V. Gavrilenko, S. Morozov, and F. Teppe, *HgCdTe-based heterostructures for terahertz photonics*. APL Materials, 2017. **5**(3): p. 035503.
43. Morozov, S.V., V.V. Romyantsev, M.A. Fadeev, M.S. Zholudev, K.E. Kudryavtsev, A.V. Antonov, A.M. Kadykov, A.A. Dubinov, N.N. Mikhailov, S.A. Dvoretzky, and V.I. Gavrilenko, *Stimulated emission from HgCdTe quantum well heterostructures at wavelengths up to 19.5 μ m*. Applied Physics Letters, 2017. **111**(19): p. 192101.
44. Krishtopenko, S.S. and F. Teppe, *Quantum spin Hall insulator with a large bandgap, Dirac fermions, and bilayer graphene analog*. Science Advances, 2018. **4**(4).
45. Zholudev, M. 2013, '*Terahertz Spectroscopy of HgCdTe / CdHgTe quantum wells*', PhD Thesis, Université de Montpellier 2

46. Guldner, Y., G. Bastard, J.P. Vieren, M. Voos, J.P. Faurie, and A. Million, *Magneto-Optical Investigations of a Novel Superlattice: HgTe-CdTe*. Physical Review Letters, 1983. **51**(10): p. 907-910.
47. Chang, Y.-C., J.N. Schulman, G. Bastard, Y. Guldner, and M. Voos, *Effects of quasi-interface states in HgTe-CdTe superlattices*. Physical Review B, 1985. **31**(4): p. 2557-2560.
48. Guldner, Y., G. Bastard, and M. Voos, *Calculated temperature dependence of the band gap of HgTe-CdTe superlattices*. Journal of Applied Physics, 1985. **57**(4): p. 1403-1405.
49. Reno, J., I.K. Sou, J.P. Faurie, J.M. Berroir, Y. Guldner, and J.P. Vieren, *HgTe-CdTe superlattices: Experimental and theoretical curves of band gap versus HgTe layer thickness*. Applied Physics Letters, 1986. **49**(2): p. 106-108.
50. Germanenko, A.V., G.M. Minkov, V.A. Larionova, O.E. Rut, C.R. Becker, and G. Landwehr, *Two-dimensional states at the HgTe/HgCdTe interface as determined from the tunneling investigations*. Physical Review B, 1995. **52**(24): p. 17254-17259.
51. Minkov, G.M., A.V. Germanenko, V.A. Larionova, and O.E. Rut, *Tunneling studies of two-dimensional states in semiconductors with inverted band structure: Spin-orbit splitting and resonant broadening*. Physical Review B, 1996. **54**(3): p. 1841-1852.
52. Stepniewski, R., *Two-dimensional states in inversion layer on zero-gap semiconductor*. Journal of Physics C: Solid State Physics, 1984. **17**(31): p. L853.
53. von Truchsess, M., V. Latussek, C.R. Becker, and E. Batke, *Landau-split and spin-split cyclotron resonance of two-dimensional electron systems in HgTe quantum wells*. Journal of Crystal Growth, 1996. **159**(1-4): p. 1104-1107.
54. Schultz, M., U. Merkt, A. Sonntag, U. Rössler, T. Colin, P. Helgesen, T. Skauli, and S. Løvold, *Density dependent cyclotron and intersubband resonance in inverted CdTe/HgTe/CdTe quantum wells*. Journal of Crystal Growth, 1998. **184**: p. 1180-1184.
55. Pfeuffer-Jeschke, A., F. Goschenhofer, S.J. Cheng, V. Latussek, J. Gerschütz, C.R. Becker, R.R. Gerhardt, and G. Landwehr, *Cyclotron masses of asymmetrically doped HgTe quantum wells*. Physica B: Condensed Matter, 1998. **256–258**: p. 486-489.
56. Landwehr, G., J. Gerschütz, S. Oehling, A. Pfeuffer-Jeschke, V. Latussek, and C.R. Becker, *Quantum transport in n-type and p-type modulation-doped mercury telluride quantum wells*. Physica E: Low-dimensional Systems and Nanostructures, 2000. **6**(1-4): p. 713-717.
57. Zhang, X.C., A. Pfeuffer-Jeschke, K. Ortner, V. Hock, H. Buhmann, C.R. Becker, and G. Landwehr, *Rashba splitting in n-type modulation-doped HgTe quantum wells with an inverted band structure*. Physical Review B, 2001. **63**(24): p. 245305.
58. Ortner, K., X.C. Zhang, A. Pfeuffer-Jeschke, C.R. Becker, G. Landwehr, and L.W. Molenkamp, *Valence band structure of HgTe/Hg(1-x)Cd(x)Te single quantum wells*. Physical Review B, 2002. **66**(7).
59. Gui, Y.S., C.R. Becker, N. Dai, J. Liu, Z.J. Qiu, E.G. Novik, M. Schäfer, X.Z. Shu, J.H. Chu, H. Buhmann, and L.W. Molenkamp, *Giant spin-orbit splitting in a HgTe quantum well*. Physical Review B, 2004. **70**(11): p. 115328.
60. Zhang, X.C., K. Ortner, A. Pfeuffer-Jeschke, C.R. Becker, and G. Landwehr, *Effective g factor of n-type HgTe/HgCdTe single quantum wells*. Physical Review B, 2004. **69**(11): p. 115340.

61. Novik, E.G., A. Pfeuffer-Jeschke, T. Jungwirth, V. Latussek, C.R. Becker, G. Landwehr, H. Buhmann, and L.W. Molenkamp, *Band structure of semimagnetic $Hg(1-y)Mn(y)Te$ quantum wells*. Physical Review B, 2005. **72**(3): p. 035321.
62. Morozov, S.V., V.V. Rumyantsev, A.M. Kadykov, A.A. Dubinov, K.E. Kudryavtsev, A.V. Antonov, N.N. Mikhailov, S.A. Dvoretiskii, and V.I. Gavrilenko, *Long wavelength stimulated emission up to 9.5 μm from $HgCdTe$ quantum well heterostructures*. Applied Physics Letters, 2016. **108**(9): p. 092104.
63. Orlita, M., K. Masztalerz, C. Faugeras, M. Potemski, E.G. Novik, C. Brüne, H. Buhmann, and L.W. Molenkamp, *Fine structure of zero-mode Landau levels in $HgTe/Hg_xCd_{1-x}Te$ quantum wells*. Physical Review B, 2011. **83**(11): p. 115307.
64. Pang, M. and X.G. Wu, *Influence of bulk inversion asymmetry on the magneto-optical spectrum of a $HgTe$ topological insulator*. Physical Review B, 2013. **88**(23): p. 235309.
65. Marcinkiewicz, M., S. Ruffenach, S.S. Krishtopenko, A.M. Kadykov, C. Consejo, D.B. But, W. Desrat, W. Knap, J. Torres, A.V. Ikonnikov, K.E. Spirin, S.V. Morozov, V.I. Gavrilenko, N.N. Mikhailov, S.A. Dvoretiskii, and F. Teppe, *Temperature-driven single-valley Dirac fermions in $HgTe$ quantum wells*. Physical Review B, 2017. **96**(3): p. 035405.
66. Goschenhofer, F., J. Gerschütz, A. Pfeuffer-Jeschke, R. Hellmig, C.R. Becker, and G. Landwehr, *Investigation of iodine as a donor in MBE grown $Hg(1-x)Cd(x)Te$* . Journal of Electronic Materials, 1998. **27**(6): p. 532-535.
67. Krishtopenko, S.S., W. Knap, and F. Teppe, *Phase transitions in two tunnel-coupled $HgTe$ quantum wells: Bilayer graphene analogy and beyond*. Scientific Reports, 2016. **6**: p. 30755.
68. Zholudev, M.S., F. Teppe, S.V. Morozov, M. Orlita, C. Consejo, S. Ruffenach, W. Knap, V.I. Gavrilenko, S.A. Dvoretiskii, and N.N. Mikhailov, *Anticrossing of Landau levels in $HgTe/CdHgTe$ (013) quantum wells with an inverted band structure*. JETP Letters, 2015. **100**(12): p. 790-794.
69. Winkler, R., *Inversion-Asymmetry-Induced Spin Splitting*. Spin-Orbit Coupling Effects in Two-Dimensional Electron and Hole Systems, ed. R. Winkler. 2003, Berlin, Heidelberg: Springer Berlin Heidelberg. 69-130.
70. Tarasenko, S.A., M.V. Durnev, M.O. Nestoklon, E.L. Ivchenko, J.-W. Luo, and A. Zunger, *Split Dirac cones in $HgTe/CdTe$ quantum wells due to symmetry-enforced level anticrossing at interfaces*. Physical Review B, 2015. **91**(8): p. 081302(R).
71. Minkov, G.M., V.Y. Aleshkin, O.E. Rut, A.A. Sherstobitov, A.V. Germanenko, S.A. Dvoretiski, and N.N. Mikhailov, *Valence band energy spectrum of $HgTe$ quantum wells with an inverted band structure*. Physical Review B, 2017. **96**(3): p. 035310.
72. Kvon, Z.D., E.B. Olshanetsky, D.A. Kozlov, N.N. Mikhailov, and S.A. Dvoretiskii, *Two-dimensional electron-hole system in a $HgTe$ -based quantum well*. JETP Letters, 2008. **87**(9): p. 502-505.
73. Kvon, Z.-D., S.N. Danilov, N.N. Mikhailov, S.A. Dvoretisky, W. Prettl, and S.D. Ganichev, *Cyclotron resonance photoconductivity of a two-dimensional electron gas in $HgTe$ quantum wells*. Physica E: Low-dimensional Systems and Nanostructures, 2008. **40**(6): p. 1885-1887.
74. Kvon, Z.D., E.B. Olshanetsky, N.N. Mikhailov, and D.A. Kozlov, *Two-dimensional electron systems in $HgTe$ quantum wells*. Low Temperature Physics, 2009. **35**(1): p. 6-14.

75. Kozlov, D.A., Z.D. Kvon, N.N. Mikhailov, S.A. Dvoretiskii, and J.C. Portal, *Cyclotron resonance in a two-dimensional semimetal based on a HgTe quantum well*. JETP Letters, 2011. **93**(3): p. 170-173.
76. Minkov, G.M., A.V. Germanenko, O.E. Rut, A.A. Sherstobitov, S.A. Dvoretiski, and N.N. Mikhailov, *Two-dimensional semimetal in a wide HgTe quantum well: Magnetotransport and energy spectrum*. Physical Review B, 2013. **88**(15).
77. Minkov, G.M., A.V. Germanenko, O.E. Rut, A.A. Sherstobitov, S.A. Dvoretiski, and N.N. Mikhailov, *Hole transport and valence-band dispersion law in a HgTe quantum well with a normal energy spectrum*. Physical Review B, 2014. **89**(16): p. 165311.
78. Minkov, G.M., A.V. Germanenko, O.E. Rut, A.A. Sherstobitov, M.O. Nestoklon, S.A. Dvoretiski, and N.N. Mikhailov, *Spin-orbit splitting of valence and conduction bands in HgTe quantum wells near the Dirac point*. Physical Review B, 2016. **93**(15): p. 155304.
79. Zhang, H., C.-X. Liu, X.-L. Qi, X. Dai, Z. Fang, and S.-C. Zhang, *Topological insulators in Bi₂Se₃, Bi₂Te₃ and Sb₂Te₃ with a single Dirac cone on the surface*. Nature Physics, 2009. **5**: p. 438.
80. Roushan, P., J. Seo, C.V. Parker, Y.S. Hor, D. Hsieh, D. Qian, A. Richardella, M.Z. Hasan, R.J. Cava, and A. Yazdani, *Topological surface states protected from backscattering by chiral spin texture*. Nature, 2009. **460**: p. 1106.
81. Fu, L. and C.L. Kane, *Topological insulators with inversion symmetry*. Physical Review B, 2007. **76**(4): p. 045302.
82. Bouvier, C., T. Meunier, P. Ballet, X. Baudry, R.B.G. Kramer, and L. Lévy, *Strained HgTe: a textbook 3D topological insulator*. <https://arxiv.org/abs/1112.2092>, 2011.
83. Leubner, P., L. Lunczer, C. Brüne, H. Buhmann, and L.W. Molenkamp, *Strain Engineering of the Band Gap of HgTe Quantum Wells Using Superlattice Virtual Substrates*. Physical Review Letters, 2016. **117**(8): p. 086403.
84. Thomas, C., O. Crauste, B. Haas, P.H. Jouneau, C. Bäuerle, L.P. Lévy, E. Orignac, D. Carpentier, P. Ballet, and T. Meunier, *Revealing topological Dirac fermions at the surface of strained HgTe thin films via quantum Hall transport spectroscopy*. Physical Review B, 2017. **96**(24): p. 245420.
85. Brüne, C., C. Thienel, M. Stuiber, J. Böttcher, H. Buhmann, E.G. Novik, C.-X. Liu, E.M. Hankiewicz, and L.W. Molenkamp, *Dirac-Screening Stabilized Surface-State Transport in a Topological Insulator*. Physical Review X, 2014. **4**(4): p. 041045.
86. Bychkov, Y.A. and E.I. Rashba, *Properties of a 2D electron gas with lifted spectral degeneracy*. JETP Letters, 1984. **39**(2): p. 78.
87. Hinz, J., H. Buhmann, M. Schäfer, V. Hock, C.R. Becker, and L.W. Molenkamp, *Gate control of the giant Rashba effect in HgTe quantum wells*. Semiconductor Science and Technology, 2006. **21**(4): p. 501.
88. Yakunin, M.V., S.M. Podgornykh, N.N. Mikhailov, and S.A. Dvoretzky, *Spin splittings in the n- quantum well with inverted band structure*. Physica E: Low-dimensional Systems and Nanostructures, 2010. **42**(4): p. 948-951.
89. Yakunin, M.V., A.V. Suslov, S.M. Podgornykh, S.A. Dvoretzky, and N.N. Mikhailov, *Effects of spin polarization in the HgTe quantum well*. Physical Review B, 2012. **85**(24).
90. Ohta, T., A. Bostwick, T. Seyller, K. Horn, and E. Rotenberg, *Controlling the Electronic Structure of Bilayer Graphene*. Science, 2006. **313**(5789): p. 951-954.

91. Yankowitz, M., J.I.-J. Wang, S. Li, A.G. Birdwell, Y.-A. Chen, K. Watanabe, T. Taniguchi, S.Y. Quek, P. Jarillo-Herrero, and B.J. LeRoy, *Band structure mapping of bilayer graphene via quasiparticle scattering*. APL Materials, 2014. **2**(9): p. 092503.
92. Budich, J.C., B. Trauzettel, and P. Michetti, *Time Reversal Symmetric Topological Exciton Condensate in Bilayer HgTe Quantum Wells*. Physical Review Letters, 2014. **112**(14): p. 146405.
93. Michetti, P. and B. Trauzettel, *Devices with electrically tunable topological insulating phases*. Applied Physics Letters, 2013. **102**(6): p. 063503.
94. Michetti, P., J.C. Budich, E.G. Novik, and P. Recher, *Tunable quantum spin Hall effect in double quantum wells*. Physical Review B, 2012. **85**(12): p. 125309.
95. Schmidt, M.J., E.G. Novik, M. Kindermann, and B. Trauzettel, *Optical manipulation of edge-state transport in HgTe quantum wells in the quantum Hall regime*. Physical Review B, 2009. **79**(24): p. 241306.
96. Liu, C., T.L. Hughes, X.-L. Qi, K. Wang, and S.-C. Zhang, *Quantum Spin Hall Effect in Inverted Type-II Semiconductors*. Physical Review Letters, 2008. **100**(23): p. 236601.
97. Knez, I., R.-R. Du, and G. Sullivan, *Evidence for Helical Edge Modes in Inverted InAs/GaSb Quantum Wells*. Physical Review Letters, 2011. **107**(13): p. 136603.
98. Murakami, S., S. Iso, Y. Avishai, M. Onoda, and N. Nagaosa, *Tuning phase transition between quantum spin Hall and ordinary insulating phases*. Physical Review B, 2007. **76**(20): p. 205304.
99. Yang, M.J., C.H. Yang, B.R. Bennett, and B.V. Shanabrook, *Evidence of a Hybridization Gap in "Semimetallic" InAs/GaSb Systems*. Physical Review Letters, 1997. **78**(24): p. 4613-4616.
100. Cooper, L.J., N.K. Patel, V. Drouot, E.H. Linfield, D.A. Ritchie, and M. Pepper, *Resistance resonance induced by electron-hole hybridization in a strongly coupled InAs/GaSb/AlSb heterostructure*. Physical Review B, 1998. **57**(19): p. 11915-11918.
101. Naveh, Y. and B. Laikhtman, *Magnetotransport of coupled electron-holes*. Europhys. Lett., 2001. **55**(4): p. 545-551.
102. Knez, I., R.R. Du, and G. Sullivan, *Finite conductivity in mesoscopic Hall bars of inverted InAs/GaSb quantum wells*. Physical Review B, 2010. **81**(20): p. 201301.
103. Du, L., I. Knez, G. Sullivan, and R.-R. Du, *Robust Helical Edge Transport in Gated InAs/GaSb Bilayers*. Physical Review Letters, 2015. **114**(9): p. 096802.
104. Knez, I., C.T. Rettner, S.-H. Yang, S.S.P. Parkin, L. Du, R.-R. Du, and G. Sullivan, *Observation of Edge Transport in the Disordered Regime of Topologically Insulating InAs/GaSb Quantum Wells*. Physical Review Letters, 2014. **112**(2): p. 026602.
105. Petchsingh, C., R.J. Nicholas, K. Takashina, N.J. Mason, and J. Zeman, *Effects of electron-hole hybridization on cyclotron resonance in InAs/GaSb heterostructures*. Physical Review B, 2004. **70**(15): p. 155306.
106. Marlow, T.P., L.J. Cooper, D.D. Arnone, N.K. Patel, D.M. Whittaker, E.H. Linfield, D.A. Ritchie, and M. Pepper, *Ground State of a Two-Dimensional Coupled Electron-Hole Gas in InAs/GaSb Narrow Gap Heterostructures*. Physical Review Letters, 1999. **82**(11): p. 2362-2365.
107. Vasilyev, Y., S. Suchalkin, K. von Klitzing, B. Meltser, S. Ivanov, and P. Kop'ev, *Evidence for electron-hole hybridization in cyclotron-resonance spectra of InAs/GaSb heterostructures*. Physical Review B, 1999. **60**(15): p. 10636-10639.

108. Suchalkin, S.D., Y.B. Vasil'ev, K. von Klitzing, V.N. Golovach, G.G. Zegrya, S.V. Ivanov, P.S. Kop'ev, and B.Y. Mel'tser, *On the nature of the oscillations of cyclotron absorption in InAs/GaSb quantum wells*. Journal of Experimental and Theoretical Physics Letters, 1998. **68**(10): p. 792-798.
109. Kim, L.S., H.D. Drew, H. Munekata, L.L. Chang, and L. Esaki, *Electron and hole cyclotron resonance in semimetallic GaSb/InAs/GaSb quantum wells*. Solid State Communications, 1988. **66**(8): p. 873-876.
110. Yang, M.J., C.H. Yang, and B.R. Bennett, *Magnetocapacitance and far-infrared photoconductivity in GaSb/InAs composite quantum wells*. Physical Review B, 1999. **60**(20): p. R13958-R13961.
111. Krishtopenko, S.S., A.V. Ikonnikov, K.V. Maremyanin, L.S. Bovkun, K.E. Spirin, A.M. Kadykov, M. Marcinkiewicz, S. Ruffenach, C. Consejo, F. Teppe, W. Knap, B.R. Semyagin, M.A. Putyato, E.A. Emelyanov, V.V. Preobrazhenskii, and V.I. Gavrilenko, *Cyclotron resonance of dirac fermions in InAs/GaSb/InAs quantum wells*. Semiconductors, 2017. **51**(1): p. 38-42.
112. Stepniewski, R., K. Pastor, and M. Grynberg, *Gamma 8 -bands anisotropy and selection rules for far-infrared magneto-optical transitions in HgTe*. Journal of Physics C: Solid State Physics, 1980. **13**(31): p. 5783.
113. Stepniewski, R., M. Grynberg, A. Wittlin, and J.A. Chroboczek, *Far-infrared magnetoabsorption in HgTe involving resonant acceptor states*. Journal of Physics C: Solid State Physics, 1979. **12**(10): p. L395.
114. Shuvaev, A.M., G.V. Astakhov, A. Pimenov, C. Brüne, H. Buhmann, and L.W. Molenkamp, *Giant Magneto-Optical Faraday Effect in HgTe Thin Films in the Terahertz Spectral Range*. Physical Review Letters, 2011. **106**(10): p. 107404.
115. Ikonnikov, A.V., A.A. Lastovkin, K.E. Spirin, M.S. Zholudev, V.V. Rumyantsev, K.V. Maremyanin, A.V. Antonov, V.Y. Aleshkin, V.I. Gavrilenko, S.A. Dvoret'skii, N.N. Mikhailov, Y.G. Sadofyev, and N. Samal, *Terahertz spectroscopy of quantum-well narrow-bandgap HgTe/CdTe-based heterostructures*. JETP Letters, 2010. **92**(11): p. 756-761.
116. Ikonnikov, A.V., S.S. Krishtopenko, O. Drachenko, M. Goiran, M.S. Zholudev, V.V. Platonov, Y.B. Kudasov, A.S. Korshunov, D.A. Maslov, I.V. Makarov, O.M. Surdin, A.V. Philippov, M. Marcinkiewicz, S. Ruffenach, F. Teppe, W. Knap, N.N. Mikhailov, S.A. Dvoret'sky, and V.I. Gavrilenko, *Temperature-dependent magnetospectroscopy of HgTe quantum wells*. Physical Review B, 2016. **94**(15): p. 155421.
117. Maremyanin, K.V., V.V. Rumyantsev, A.V. Ikonnikov, L.S. Bovkun, E.G. Chizhevskii, I.I. Zasavitskii, and V.I. Gavrilenko, *Terahertz injection lasers based on PbSnSe alloy with an emission wavelength up to 46.5 μm* . Semiconductors, 2016. **50**(12): p. 1669-1672.
118. Knap, W., R. Stepniewski, and E. Fantner, *Optically Induced Nernst-Ettinghausen Effect in the Far Infrared and Strong Magnetic Fields in HgTe and InSb*. physica status solidi (b), 1985. **132**(1): p. 133-140.
119. Olbrich, P., C. Zoth, P. Vierling, K.M. Dantscher, G.V. Budkin, S.A. Tarasenko, V.V. Bel'kov, D.A. Kozlov, Z.D. Kvon, N.N. Mikhailov, S.A. Dvoret'sky, and S.D. Ganichev, *Giant photocurrents in a Dirac fermion system at cyclotron resonance*. Physical Review B, 2013. **87**(23): p. 235439.
120. Griffiths, P.R. and J.D. De Haseth, *Fourier Transform Infrared Spectrometry*. 2nd ed, ed. D. Winefordner. 560.

121. Haki, M. 2017, '*Infrared magneto-spectroscopy of relativistic-like electrons in three-dimensional solids*', Université Grenoble Alpes
122. Ikonnikov, A.V., L.S. Bovkun, V.V. Romyantsev, S.S. Krishtopenko, V.Y. Aleshkin, A.M. Kadykov, M. Orlita, M. Potemski, V.I. Gavrilenko, S.V. Morozov, S.A. Dvoretzky, and N.N. Mikhailov, *On the Band Spectrum in p-type HgTe/CdHgTe heterostructures and its transformation under temperature variation*. Semiconductors, 2017. **51**(12): p. 1531-1536.
123. Kvon, Z.D., S.N. Danilov, D.A. Kozlov, C. Zoth, N.N. Mikhailov, S.A. Dvoretzky, and S.D. Ganichev, *Cyclotron resonance of Dirac fermions in HgTe quantum wells*. JETP Letters, 2012. **94**(11): p. 816-819.
124. Dziom, V., A. Shuvaev, N.N. Mikhailov, and A. Pimenov, *Terahertz properties of Dirac fermions in HgTe films with optical doping*. 2D Materials, 2017. **4**(2): p. 024005.
125. Crassee, I., J. Levallois, A.L. Walter, M. Ostler, A. Bostwick, E. Rotenberg, T. Seyller, D. van der Marel, and A.B. Kuzmenko, *Giant Faraday rotation in single- and multilayer graphene*. Nature Physics, 2010. **7**: p. 48.
126. Volkov, A.A., G.V. Kozlov, and A.M. Prokhorov, *Progress in submillimeter spectroscopy of solid state*. Infrared Physics, 1989. **29**(2): p. 747-752.
127. Volkov, A.A., Y.G. Goncharov, G.V. Kozlov, S.P. Lebedev, and A.M. Prokhorov, *Dielectric measurements in the submillimeter wavelength region*. Infrared Physics, 1985. **25**(1): p. 369-373.
128. Katsuaki, S., *Measurement of Magneto-Optical Kerr Effect Using Piezo-Birefringent Modulator*. Japanese Journal of Applied Physics, 1981. **20**(12): p. 2403.
129. Kühne, P., C.M. Herzinger, M. Schubert, J.A. Woollam, and T. Hofmann, *Invited Article: An integrated mid-infrared, far-infrared, and terahertz optical Hall effect instrument*. Review of Scientific Instruments, 2014. **85**(7): p. 071301.
130. Levallois, J., I.O. Nedoliuk, I. Crassee, and A.B. Kuzmenko, *Magneto-optical Kramers-Kronig analysis*. Review of Scientific Instruments, 2015. **86**(3): p. 033906.
131. Buttner, B., C.X. Liu, G. Tkachov, E.G. Novik, C. Brune, H. Buhmann, E.M. Hankiewicz, P. Recher, B. Trauzettel, S.C. Zhang, and L.W. Molenkamp, *Single valley Dirac fermions in zero-gap HgTe quantum wells*. Nature Physics, 2011. **7**(5): p. 418-422.
132. Kadykov, A.M., S.S. Krishtopenko, B. Jouault, W. Desrat, M. Marcinkiewicz, J. Torres, S. Ruffenach, C. Consejo, N. Dyakonova, D. But, K. Spirin, S. Morozov, V. Gavrilenko, N. Mikhailov, S.A. Dvoretzky, Z.D. Kvon, W. Кнап, and F. Терпе. *Temperature-driven quantum spin Hall state in HgTe quantum well*. in *Труды XXI Международного симпозиума*. 2017. Нижний Новгород: Издательство Нижегородского государственного университета им. Н.И.Лобачевского.
133. Кукушкин, И.В., С.В. Мешков, and В.Б. Тимофеев, *Плотность состояний двумерных электронов в поперечном магнитном поле*. Успехи физических наук, 1988. **155**(6): p. 219-264.
134. Гаврилов, М.Г. and И.В. Кукушкин, *Плотность состояний в щелях энергетического спектра двумерных электронов в поперечном магнитном поле*. Письма в ЖЭТФ, 1986. **43**(2): p. 79.
135. Stahl, E., D. Weiss, G. Weimann, K.v. Klitzing, and K. Ploog, *Density of states of a two-dimensional electron gas in a strong magnetic field*. Journal of Physics C: Solid State Physics, 1985. **18**(26): p. L783.

136. Weiss, D., E. Stahl, G. Weimann, K. Ploog, and K. Von Klitzing, *Density of states in Landau level tails of GaAs/AlxGa1-xAs heterostructures*. Surface Science, 1986. **170**(1): p. 285-291.
137. Piot, B. 2006, '*Spin splitting in the quantum Hall regime*', Université Joseph-Fourier - Grenoble I
138. Ando, T., A.B. Fowler, and F. Stern, *Electronic properties of two-dimensional systems*. Reviews of Modern Physics, 1982. **54**(2): p. 437-672.
139. Gerhardt, R.R., *Cumulant approach to the two-dimensional magneto-conductivity problem*. Surface Science, 1976. **58**(1): p. 227-234.
140. Ando, T. and Y. Uemura, *Theory of Oscillatory g Factor in an MOS Inversion Layer under Strong Magnetic Fields*. Journal of the Physical Society of Japan, 1974. **37**(4): p. 1044-1052.
141. Zhang, X.C., A. Pfeuffer-Jeschke, K. Ortner, C.R. Becker, and G. Landwehr, *Absence of magneto-intersubband scattering in n-type HgTe quantum wells*. Physical Review B, 2002. **65**(4): p. 045324.
142. Криштопенко, С.С., К.В. Маремьянин, К.П. Калинин, К.Е. Спирин, В.И. Гавриленко, Н.В. Байдусь, and Б.Н. Звонков, *Обменное усиление g-фактора электронов в напряженных гетероструктурах InGaAs/InP*. Физика и техника полупроводников, 2015. **49**(12): p. 196-203.
143. Gudina, S.V., V.N. Neverov, E.V. Ilchenko, A.S. Bogolubskii, G.I. Harus, N.G. Shelushinina, S.M. Podgornyykh, M.V. Yakunin, N.N. Mikhailov, and S.A. Dvoretzky, *Electron Effective Mass and g Factor in Wide HgTe Quantum Wells*. Semiconductors, 2018. **52**(1): p. 12-18.
144. Suzuki, K. and J.C. Hensel, *Quantum resonances in the valence bands of germanium. I. Theoretical considerations*. Physical Review B, 1974. **9**(10): p. 4184-4218.
145. Hensel, J.C. and K. Suzuki, *Quantum resonances in the valence bands of germanium. II. Cyclotron resonances in uniaxially stressed crystals*. Physical Review B, 1974. **9**(10): p. 4219-4257.
146. Trebin, H.R., U. Rössler, and R. Ranvaud, *Quantum resonances in the valence bands of zinc-blende semiconductors. I. Theoretical aspects*. Physical Review B, 1979. **20**(2): p. 686-700.
147. Ranvaud, R., H.R. Trebin, U. Rössler, and F.H. Pollak, *Quantum resonances in the valence band of zinc-blende semiconductors. II. Results for p-InSb under uniaxial stress*. Physical Review B, 1979. **20**(2): p. 701-715.
148. Bovkun, L.S., A.V. Ikonnikov, V.Y. Aleshkin, K.E. Spirin, V.I. Gavrilenko, N.N. Mikhailov, S.A. Dvoretzki, F. Teppe, B.A. Piot, M. Potemski, and M. Orlita, *Landau level spectroscopy of valence bands in HgTe quantum wells: Effects of symmetry lowering*. <https://arxiv.org/abs/1711.08783>, 2018 (with referees).
149. Durnev, M.V. and S.A. Tarasenko, *Magnetic field effects on edge and bulk states in topological insulators based on HgTe/CdHgTe quantum wells with strong natural interface inversion asymmetry*. Physical Review B, 2016. **93**(7): p. 075434.
150. Dvoretzky, S., N. Mikhailov, Y. Sidorov, V. Shvets, S. Danilov, B. Wittman, and S. Ganichev, *Growth of HgTe Quantum Wells for IR to THz Detectors*. Journal of Electronic Materials, 2010. **39**(7): p. 918-923.
151. Ando, T., *Theory of Cyclotron Resonance Lineshape in a Two-Dimensional Electron System*. Journal of the Physical Society of Japan, 1975. **38**(4): p. 989-997.

152. Kalinin, K.P., S.S. Krishtopenko, K.V. Maremyanin, K.E. Spirin, V.I. Gavrilenko, A.A. Biryukov, N.V. Baidus, and B.N. Zvonkov, *Rashba spin splitting and cyclotron resonance in strained InGaAs/InP heterostructures with a two-dimensional electron gas*. Semiconductors, 2013. **47**(11): p. 1485-1491.
153. Kadykov, A.M., S.S. Krishtopenko, B. Jouault, W. Desrat, W. Knap, S. Ruffenach, C. Consejo, J. Torres, S.V. Morozov, N.N. Mikhailov, S.A. Dvoretiskii, and F. Teppe, *Temperature-Induced Topological Phase Transition in HgTe Quantum Wells*. Physical Review Letters, 2018. **120**(8): p. 086401.
154. Khouri, T., M. Bendias, P. Leubner, C. Brüne, H. Buhmann, L.W. Molenkamp, U. Zeitler, N.E. Hussey, and S. Wiedmann, *High-temperature quantum Hall effect in finite gapped HgTe quantum wells*. Physical Review B, 2016. **93**(12): p. 125308.
155. Kozlov, D.A., Z.D. Kvon, N.N. Mikhailov, S.A. Dvoretiskii, S. Weishäupl, Y. Krupko, and J.C. Portal, *Quantum Hall effect in HgTe quantum wells at nitrogen temperatures*. Applied Physics Letters, 2014. **105**(13): p. 132102.
156. Usher, A., R.J. Nicholas, J.J. Harris, and C.T. Foxon, *Observation of magnetic excitons and spin waves in activation studies of a two-dimensional electron gas*. Physical Review B, 1990. **41**(2): p. 1129-1134.
157. Wei, H.P., A.M. Chang, D.C. Tsui, and M. Razeghi, *Temperature dependence of the quantized Hall effect*. Physical Review B, 1985. **32**(10): p. 7016-7019.
158. Isihara, A. and L. Smrcka, *Density and magnetic field dependences of the conductivity of two-dimensional electron systems*. Journal of Physics C: Solid State Physics, 1986. **19**(34): p. 6777.
159. Shklovskii, B.I. and A.L. Efros, *Variable-Range Hopping Conduction*, in *Electronic Properties of Doped Semiconductors*, B.I. Shklovskii and A.L. Efros, Editors. 1984, Springer Berlin Heidelberg: Berlin, Heidelberg. p. 202-227.
160. Coleridge, P.T., R. Stoner, and R. Fletcher, *Low-field transport coefficients in GaAs/Ga_{1-x}Al_xAs heterostructures*. Physical Review B, 1989. **39**(2): p. 1120-1124.
161. Coleridge, P.T., *Small-angle scattering in two-dimensional electron gases*. Physical Review B, 1991. **44**(8): p. 3793-3801.
162. Endo, A. and Y. Iye, *The Effect of Oscillating Fermi Energy on the Line Shape of the Shubnikov-de Haas Oscillation in a Two-Dimensional Electron Gas*. Journal of the Physical Society of Japan, 2008. **77**(6): p. 064713.
163. Ando, T. and Y. Uemura, *Theory of Quantum Transport in a Two-Dimensional Electron System under Magnetic Fields II. Single-Site Approximation under Strong Fields*. Journal of the Physical Society of Japan, 1974. **36**(6): p. 1521-1529.
164. Califano, M., T. Chakraborty, P. Pietiläinen, and C.M. Hu, *Breaking of Larmor's theorem in quantum Hall states with spin-orbit coupling*. Physical Review B, 2006. **73**(11): p. 113315.
165. Lifshitz, I.M. and A.M. Kosevich, *Theory of Magnetic Susceptibility in Metals at Low Temperature*. JETP, 1956. **29**(4): p. 730.
166. Shoenberg, D., *Magnetic Oscillations in Metals*. Cambridge Monographs on Physics. 1984, Cambridge: Cambridge University Press.
167. Бовкун, Л.С., С.С. Криштопенко, М.С. Жолудев, А.В. Иконников, К.Е. Спири́н, С.А. Дворецкий, Н.Н. Михайлов, Ф. Тeppe, W. Кнар, and В.И. Гавриленко, *Обменное усиление g-фактора электронов в двумерном полуметалле в квантовых ямах HgTe*. Физика и техника полупроводников, 2015. **49**(12): p. 1676-1682.

168. Комник, Ю.Ф., И.Б. Беркутов, В.В. Андриевский, О.А. Миронов, М. Миронов, and Д. Ледли, *Особенности осцилляций Шубникова-де Гааза проводимости высокоподвижного двумерного дырочного газа в квантовой яме SiGe/Ge/SiGe*. Физика низких температур, 2006. **32**(1): p. 109-114.
169. Беркутов, И.Б., В.В. Андриевский, Ю.Ф. Комник, О.А. Миронов, and M.L. Миронов, D.R., *Осцилляции Шубникова-де Гааза проводимости двумерного дырочного газа в квантовых ямах на основе германия и кремния. Определение эффективной массы и g-фактора*. Физика низких температур, 2009. **35**(2): p. 188-193.
170. Coleridge, P.T., *Correlation lengths for scattering potentials in two-dimensional electron gases*. Semiconductor Science and Technology, 1997. **12**(1): p. 22.
171. Piot, B.A., D.K. Maude, M. Henini, Z.R. Wasilewski, K.J. Friedland, R. Hey, K.H. Ploog, A.I. Todorov, R. Airey, and G. Hill, *Quantum Hall ferromagnet at high filling factors: A magnetic-field-induced Stoner transition*. Physical Review B, 2005. **72**(24).
172. Krishtopenko, S.S., I. Yahniuk, D.B. But, V.I. Gavrilenko, W. Knap, and F. Tepe, *Pressure- and temperature-driven phase transitions in HgTe quantum wells*. Physical Review B, 2016. **94**(24): p. 245402.
173. Платонов, В.В., Ю.Б. Кудасов, И.В. Макаров, Д.А. Маслов, О.М. Сурдин, М.С. Жолудев, А.В. Иконников, В.И. Гавриленко, Н.Н. Михайлов, and С.А. Дворецкий, *Исследование магнитопоглощения при различных температурах в гетероструктурах HgTe/CdHgTe с квантовыми ямами в импульсных магнитных полях*. Физика и техника полупроводников, 2015. **49**(12): p. 1660-1664.
174. Platonov, V.V., Y.B. Kudasov, I.V. Makarov, D.A. Maslov, O.M. Surdin, M.S. Zholudev, A.V. Ikonnikov, V.I. Gavrilenko, N.N. Mikhailov, and S.A. Dvoretzky, *Investigation of magnetoabsorption at different temperatures in HgTe/CdHgTe quantum-well heterostructures in pulsed magnetic fields*. Semiconductors, 2015. **49**(12): p. 1611-1615.
175. Krishtopenko, S.S., V.I. Gavrilenko, and M. Goiran, *Theory of g-factor enhancement in narrow-gap quantum well heterostructures*. J Phys Condens Matter, 2011. **23**(38): p. 385601.
176. Krishtopenko, S.S., V.I. Gavrilenko, and M. Goiran, *The effect of exchange interaction on quasiparticle Landau levels in narrow-gap quantum well heterostructures*. Journal of Physics: Condensed Matter, 2012. **24**(13): p. 135601.
177. Krishtopenko, S.S., K.V. Maremyanin, K.P. Kalinin, K.E. Spirin, V.I. Gavrilenko, N.V. Baidus, and B.N. Zvonkov, *Exchange enhancement of the electron g factor in strained InGaAs/InP heterostructures*. Semiconductors, 2015. **49**(2): p. 191-198.
178. Krishtopenko, S.S., V. Gavrilenko, and M. Goiran, *Exchange Enhancement of g-Factor in Narrow-Gap InAs/AlSb Quantum Well Heterostructures*. Solid State Phenomena, 2012. **190**: p. 554-557.
179. Криштопенко, С.С., К.П. Калинин, В.И. Гавриленко, Ю.Г. Садофьев, and M. Goiran, *Спиновое расщепление Рашибы и обменное усиление g-фактора в гетероструктурах InAs/AlSb двумерным электронным газом*. Физика и техника полупроводников, 2012. **46**(9): p. 1186.
180. Krishtopenko, S.S., K.P. Kalinin, V.I. Gavrilenko, Y.G. Sadofyev, and M. Goiran, *Rashba spin splitting and exchange enhancement of the g factor in InAs/AlSb heterostructures with a two-dimensional electron gas*. Semiconductors, 2012. **46**(9): p. 1163-1170.

181. Drachenko, O., D.V. Kozlov, V.Y. Aleshkin, V.I. Gavrilenko, K.V. Maremyanin, A.V. Ikonnikov, B.N. Zvonkov, M. Goiran, J. Leotin, G. Fasching, S. Winnerl, H. Schneider, J. Wosnitza, and M. Helm, *High-field splitting of the cyclotron resonance absorption in strained p-InGaAs/GaAs quantum wells*. Physical Review B, 2009. **79**(7): p. 073301.
182. Aleshkin, V.Y., D.B. Veksler, V.I. Gavrilenko, I.V. Erofeeva, A.V. Ikonnikov, D.V. Kozlov, and O.A. Kuznetsov, *Shallow-impurity-assisted transitions in the course of submillimeter magnetoabsorption of strained Ge/GeSi(111) quantum-well heterostructures*. Physics of the Solid State, 2004. **46**(1): p. 125-129.
183. Bovkun, L.S., S.S. Krishtopenko, A.V. Ikonnikov, V.Y. Aleshkin, A.M. Kadykov, S. Ruffenach, C. Consejo, F. Teppe, W. Knap, M. Orlita, B. Piot, M. Potemski, N.N. Mikhailov, S.A. Dvoretiskii, and V.I. Gavrilenko, *Magneto spectroscopy of double HgTe/CdHgTe quantum wells*. Semiconductors, 2016. **50**(11): p. 1532-1538.
184. Yakunin, M.V., S.S. Krishtopenko, S.M. Podgornykh, M.R. Popov, V.N. Neverov, N.N. Mikhailov, and S.A. Dvoretiskii, *HgTe/CdHgTe double quantum well with a spectrum of bilayer graphene and peculiarities of its magnetotransport*. JETP Letters, 2016. **104**(6): p. 403-410.
185. Yakunin, M.V., A.V. Suslov, M.R. Popov, E.G. Novik, S.A. Dvoretiskii, and N.N. Mikhailov, *Magnetotransport in double quantum well with inverted energy spectrum: HgTe/CdHgTe*. Physical Review B, 2016. **93**(8).
186. Novoselov, K.S., A.K. Geim, S.V. Morozov, D. Jiang, M.I. Katsnelson, I.V. Grigorieva, S.V. Dubonos, and A.A. Firsov, *Two-dimensional gas of massless Dirac fermions in graphene*. Nature, 2005. **438**: p. 197.
187. Liu, Z.K., J. Jiang, B. Zhou, Z.J. Wang, Y. Zhang, H.M. Weng, D. Prabhakaran, S.K. Mo, H. Peng, P. Dudin, T. Kim, M. Hoesch, Z. Fang, X. Dai, Z.X. Shen, D.L. Feng, Z. Hussain, and Y.L. Chen, *A stable three-dimensional topological Dirac semimetal Cd₃As₂*. Nature Materials, 2014. **13**: p. 677.
188. Orlita, M., D.M. Basko, M.S. Zholudev, F. Teppe, W. Knap, V.I. Gavrilenko, N.N. Mikhailov, S.A. Dvoretiskii, P. Neugebauer, C. Faugeras, A.L. Barra, G. Martinez, and M. Potemski, *Observation of three-dimensional massless Kane fermions in a zinc-blende crystal*. Nat Phys, 2014. **10**(3): p. 233-238.
189. Xu, S.-Y., I. Belopolski, N. Alidoust, M. Neupane, G. Bian, C. Zhang, R. Sankar, G. Chang, Z. Yuan, C.-C. Lee, S.-M. Huang, H. Zheng, J. Ma, D.S. Sanchez, B. Wang, A. Bansil, F. Chou, P.P. Shibayev, H. Lin, S. Jia, and M.Z. Hasan, *Discovery of a Weyl fermion semimetal and topological Fermi arcs*. Science, 2015. **349**(6248): p. 613-617.
190. Teppe, F., M. Marcinkiewicz, S.S. Krishtopenko, S. Ruffenach, C. Consejo, A.M. Kadykov, W. Desrat, D. But, W. Knap, J. Ludwig, S. Moon, D. Smirnov, M. Orlita, Z. Jiang, S.V. Morozov, V.I. Gavrilenko, N.N. Mikhailov, and S.A. Dvoretiskii, *Temperature-driven massless Kane fermions in HgCdTe crystals*. Nature Communications, 2016. **7**: p. 12576.
191. Емельянов, Е.А., Д.Ф. Феклин, А.В. Васев, М.А. Пулято, Б.Р. Семягин, А.П. Василенко, О.П. Пчеляков, and В.В. Преображенский, *Формирование напряженных короткопериодных сверхрешеток InAs/GaSb торого типа для фотоприемников ИК-диапазона методом молекулярно-лучевой эпитаксии*. Автометрия, 2011. **47**(5): p. 43.
192. Емельянов, Е.А., Д.Ф. Феклин, А.В. Васев, М.А. Пулято, Б.Р. Семягин, И.Б. Чистохин, А.К. Гутаковский, А.П. Василенко, О.П. Пчеляков, and В.В. Преображенский, *Молекулярно-лучевая эпитаксия сверхрешеток II типа InAs/GaSb для фотоприемников ИК-диапазона*. Юбилейный сборник избранных

- трудов Института физики полупроводников им. А.В.Ржанова СО РАН (1964-2014). 2014, Новосибирск: Параллель. 843.
193. Sadofyev, Y.G., A. Ramamoorthy, B. Naser, J.P. Bird, S.R. Johnson, and Y.-H. Zhang, *Large g-factor enhancement in high-mobility InAs/AlSb quantum wells*. Applied Physics Letters, 2002. **81**(10): p. 1833-1835.
 194. Vurgaftman, I., J.R. Meyer, and L.R. Ram-Mohan, *Band parameters for III-V compound semiconductors and their alloys*. Journal of Applied Physics, 2001. **89**(11): p. 5815-5875.
 195. Ikonnikov, A.V., A.V. Antonov, A.A. Lastovkin, V.I. Gavrilenko, Y.G. Sadof'ev, and N. Samal, *High-resolution emission spectra of pulsed terahertz quantum-cascade lasers*. Semiconductors, 2010. **44**(11): p. 1467-1471.
 196. Aleshkin, V.Y., V.I. Gavrilenko, D.M. Gaponova, A.V. Ikonnikov, K.V. Marem'yanin, S.V. Morozov, Y.G. Sadofyev, S.R. Johnson, and Y.-H. Zhang, *Spectra of persistent photoconductivity in InAs/AlSb quantum-well heterostructures*. Semiconductors, 2005. **39**(1): p. 22-26.
 197. Zawadzki, W., *Mechanisms of electron scattering in semiconductors*. 1979: Zakład Narodowy imienia Ossolińskich Wydawnictwo Polskiej Akademii Nauk.
 198. Horst, M., U. Merkt, W. Zawadzki, J.C. Maan, and K. Ploog, *Resonant polarons in a GaAs-GaAlAs heterostructure*. Solid State Communications, 1985. **53**(4): p. 403-405.
 199. Yang, M.J., P.J. Lin-Chung, B.V. Shanabrook, J.R. Waterman, R.J. Wagner, and W.J. Moore, *Enhancement of cyclotron mass in semiconductor quantum wells*. Physical Review B, 1993. **47**(3): p. 1691-1694.
 200. Ikonnikov, A., S. Krishtopenko, V. Gavrilenko, Y. Sadofyev, Y. Vasilyev, M. Orlita, and W. Knap, *Splitting of Cyclotron Resonance Line in InAs/AlSb QW Heterostructures in High Magnetic Fields: Effects of Electron-Electron and Electron-Phonon Interaction*. Journal of Low Temperature Physics, 2010. **159**(1): p. 197-202.